Downloaded from orbit.dtu.dk on: Dec 17, 2017

Technical University of Denmark

Characterization of the Resonant Properties of Multi-layer Cantilever Sensors

Sandberg, Rasmus Kousholt; Svendsen, Winnie Edith; Boisen, Anja

Publication date:
2005

Document Version
Publisher's PDF, also known as Version of record

Link back to DTU Orbit

Citation (APA):
Sandberg, R. K., Svendsen, W. E., & Boisen, A. (2005). Characterization of the Resonant Properties of Multi-layer Cantilever Sensors.

DTU Library
Technical Information Center of Denmark

General rights
Copyright and moral rights for the publications made accessible in the public portal are retained by the authors and/or other copyright owners and it is a condition of accessing publications that users recognise and abide by the legal requirements associated with these rights.

- Users may download and print one copy of any publication from the public portal for the purpose of private study or research.
- You may not further distribute the material or use it for any profit-making activity or commercial gain
- You may freely distribute the URL identifying the publication in the public portal

If you believe that this document breaches copyright please contact us providing details, and we will remove access to the work immediately and investigate your claim.

Characterization of the Resonant Properties of Multi-layer Cantilever Sensors

PhD Thesis

Rasmus Sandberg

May 1, 2005

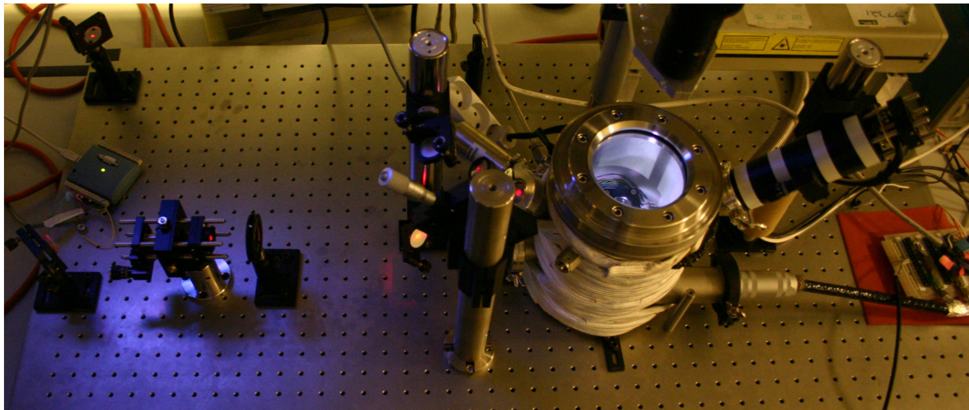

MIC – Department of Micro and Nanotechnology, building 345 east
2800 Kgs. Lyngby, Denmark

Preface

This thesis has been written as a part of the requirements for obtaining the PhD degree at the Technical University of Denmark (DTU). The PhD project has been carried out at Research Center COM and at the Department of Micro and Nanotechnology (MIC) at DTU in the period from September 2001 to April 2005.

This PhD project has been part of the Bioprobe project at MIC and was financed by a DTU PhD grant. The project has been carried out under supervision of

Professor, Dr. Anja Boisen
Main supervisor
Associate Professor, Dr. Winnie Svendsen
Co-supervisor

During this PhD project, I have depended on – and received help and encouragement from quite a number of people. I want to thank:

Winnie Svendsen for being the most outstanding supervisor, organizer and prioritizer I could possibly imagine. I am very grateful for all that you have given me.

Anja Boisen for great support and for being the source of the creative, dynamic and pleasant environment that is characteristic for the Bioprobes group.

Kristian Mølhave for helping me out with cantilever chips, good ideas and insightful considerations.

Reges Cezar de Andrade Costa for doing a great job with the LabVIEW instrumentation control.

The people from the Bioprobes group: Montserrat Calleja, Zachary Davis, Søren Dohn, Esko Forsén, Alexander Grigorov, Daniel Häfliger, Jan Harry Hales, Maria Holmberg, Alicia Johansson, Malene Erup Larsen, Rodolphe Marie, Ramona Matieu, Maria Nordström, Peter Rasmussen — you guys kick a⋆⋆.

Everybody else at MIC – scientific and administrative staff alike – for always being willing to help out, for sharing your knowledge and experience, and for generally making MIC a great place to work and study.

Christian Mikkelsen for a lot of good talks, mental support and kanelgifler.

Det unge talent, Anders Harpøth for making the time as a PhD student more fun and less H⋆ll. Truly amazing.

Karin Andersen for good laughs, good moods and for turning me around at the last minute.

Erik Wenzel of Wenzel Vakuum Teknik ApS, Knud Christensen of Abeto Teknik A/S, Erik Pedersen of Habia Cable and Lars Sander and Glenn Nielsen of Danish Micro Engineering A/S for being particularly helpful with details of the vacuum chamber and optical detection setup.

All my friends for not forgetting about me despite my lack of time to socialize.

My formidable family and incredible in-laws: Lone, Jørgen, Rikke, Christian, Kirsten, Ove, Anja for all your interest in my work and wellbeing, and for reminding me that there's a life after deadline.

Finally, my wonderful Mette for all your love and patience – especially during the final part of my work, when I gave very little in return. Words cannot describe how much you mean to me.

Kgs. Lyngby, May 1, 2005

Rasmus Sandberg
MIC – Department of Micro and Nanotechnology, building 345 east
2800 Kgs. Lyngby
Denmark

Abstract

Resonant cantilever-based mass sensors utilize the fact that a vibrating beam experiences a shift in resonance frequency when the beam's mass is altered, e.g. by adsorption of particles. The mass-sensitivity of a cantilever-sensor is defined by the resolution with which this frequency shift can be measured. A measure of this frequency-resolution is the *quality-factor* (or *Q-factor*), which depends on the energy loss and damping that the vibrating cantilever experiences.

The major part of this PhD project has been to design and construct a vacuum chamber in which the environmental conditions such as temperature, pressure and gas constituents can be controlled with sufficient accuracy to perform characterizations of micro- and nanocantilevers.

The vacuum chamber has been fitted with electrical interconnections for cantilever actuation and signal detection; and with flanges for inlet of vaporized chemicals for adsorption and detection experiments. Special equipment has been designed for piezoelectric actuation of passive cantilevers and for video inspection of the cantilever samples inside the chamber.

A laser-optical detection system has been designed and built in conjunction with the vacuum chamber for characterization of the resonant properties (i.e. resonance frequencies and Q-factors) of micro- and nano-cantilevers as well as alternative resonant devices.

Upon completion of the chamber- and detection setup, an experimental investigation of resonant silicon dioxide microcantilevers was performed. The resonance frequency and Q-factor of the fundamental and higher order flexural modes were characterized at different temperatures and pressures and with different thicknesses of a top-surface gold coating.

An analytical solution for the flexural eigenmodes of a multi-layered vibrating cantilever was derived and its validity was verified by comparison to finite–element analysis as well as the experimentally measured resonance frequencies in vacuum.

Dansk resumé

Dansk titel: Karakterisering af de resonante egenskaber for flerlagscantilever-sensorer

Resonante cantilever-baserede massesensorer udnytter, at der sker en forskydning af resonansfrekvensen når cantileverens masse ændres, f.eks. ved adsorption af partikler. Masse-følsomheden af en cantilever-sensor er bestemt af den opløsning, som denne frekvensforskydning kan måles med. Et mål for denne frekvensopløsning er *kvalitetsfaktoren* (eller *Q-faktoren*), som afhænger af det energitab og den dæmpning, som den vibrerende cantilever udsættes for.

Hovedparten af dette ph.d.-projekt har været at designe og konstruere et vakuumkammer, i hvilket de omgivende forhold såsom temperatur, tryk og gas-sammensætning kan kontrolleres med tilstrækkelig nøjagtighed til at udføre karakteriseringer af mikro- og nanocantilevere.

Vakuumkammeret er blevet udstyret med elektriske forbindelser til cantilever-aktuering og signal-detektion; og med flanger til indførsel af fordampede kemikalier til adsorptions- og detektionseksperimenter. Der er blevet designet specialudstyr til piezoelektrisk aktuering af passive cantilevere og til video-inspektion af cantilever-prøverne inde i kammeret.

Et laser-optisk detektionssystem er blevet designet og opbygget i sammenhæng med vakuumkammeret, til karakterisering af de resonante egenskaber (dvs. resonansfrekvenser og Q-faktorer) af mikro- og nanocantilevere såvel som alternative resonante komponenter.

En eksperimentel undersøgelse af resonante siliciumdioxid-mikrocantilevere blev udført efter færdiggørelsen af kammer- og detektionsopstillingen. Resonansfrekvensen og Q-faktoren for den fundamentale samt højere ordens udbøjningstilstande blev karakteriseret ved forskellige temperaturer og tryk og med forskellige tykkelser af top-overflade-guldbelægninger.

En analytisk løsning til de udbøjende egentilstande for en vibrerende flerlagscantilever blev udledt og dens validitet blev bekræftet ved sammenligning med *finite–element*-analyser samt med de eksperimentelt målte resonansfrekvenser i vakuum.

Contents

Preface i

Abstract iii

Dansk resumé iv

1 Introduction 1
- 1.1 Cantilever sensor operation . . . 1
- 1.2 Resonant cantilever characterization . . . 3
- 1.3 Multi-layer cantilevers . . . 5
- 1.4 Overview of the thesis . . . 5

2 Flexural eigenmodes of a multi-layer cantilever 7
- 2.1 Analytical theory . . . 8

3 Vacuum chamber for cantilever characterization 11
- 3.1 Introduction . . . 11
- 3.2 Vacuum chamber body design . . . 12
- 3.3 Basic equipment . . . 14
  - 3.3.1 Gas Inlet . . . 14
  - 3.3.2 Vacuum Pump . . . 15
  - 3.3.3 Pressure Sensor . . . 15
  - 3.3.4 Temperature Control . . . 16
- 3.4 Special equipment . . . 19
  - 3.4.1 Sample holder & electrical connections . . . 19
  - 3.4.2 Video inspection . . . 22
  - 3.4.3 Vapor Injection . . . 24
- 3.5 Optical detection system . . . 27
  - 3.5.1 Introduction . . . 27
  - 3.5.2 Laser focusing . . . 27
  - 3.5.3 Detection and amplification . . . 31

3.6 Improvements . . . 36
3.6.1 Improvements of current setup . . . 36
3.6.2 Second generation setup . . . 39

4 Resonant properties of monolithic and gold-coated SiO_2 cantilevers 40
4.1 Background . . . 40
4.2 Experiment . . . 41
4.2.1 Initial considerations . . . 41
4.2.2 Design of experiments . . . 42
4.2.3 Cantilever devices . . . 43
4.2.4 Chip mounting . . . 45
4.2.5 Actuation and detection . . . 46
4.2.6 Measurement procedure . . . 48
4.3 Results . . . 51
4.3.1 Resonant modes . . . 51
4.3.2 Q-factor dependence on resonance frequency . . . 53
4.3.3 Q-factor dependence on gold coating in vacuum . . . 55
4.3.4 Q-factor dependence on gold coating at atmospheric pressure . . . 56
4.3.5 Resonance frequency dependence on pressure . . . 58
4.3.6 Q-factor dependence on pressure . . . 61
4.3.7 Resonance frequency dependence on temperature . . . 63
4.3.8 Q-factor dependence on temperature . . . 66
4.4 Discussion . . . 68
4.5 Outlook . . . 69

5 DNA Detection 71
5.1 Introduction . . . 71
5.2 Sensitivity calculation . . . 71
5.3 Laser lithographic de-functionalization . . . 74
5.4 Discussion . . . 75

6 Vacuum chamber applications 77
6.1 Fully CMOS integrated nanoresonator system with attogram/Hz mass resolution . . . 77
6.1.1 Introduction . . . 77
6.1.2 Results . . . 78
6.2 Enhanced functionality of cantilever mass sensors . . . 80
6.2.1 Introduction . . . 80
6.2.2 Results . . . 81

6.3 Alternative structures . . . 81
6.3.1 In-plane vibrating cantilevers . . . 82
6.3.2 Micro-bridge resonators . . . 84

7 Conclusions 86

A List of publications 88

B Transformation of the Gaussian beam 90
B.1 Gaussian beam characteristics . . . 90
B.2 Transformation through a thin lens . . . 92

C Finite-element simulation of gold coated cantilevers 93

D Technical drafts 95
D.1 Vacuum chamber body . . . 95
D.2 Mounting plate . . . 99
D.3 Lens holder . . . 100

E Electronic diagrams 102
E.1 PSD Preamplifier . . . 102
E.2 Difference-amplifier . . . 104

F LabVIEW Interface 106
F.1 Gain–phase analyzer VI . . . 106
F.1.1 Graphical interface . . . 106
F.1.2 Program structure . . . 107
F.2 Temperature and pressure interface VI . . . 109
F.2.1 Graphical interface . . . 109
F.2.2 Program structure . . . 110

G List of abbreviations 112

List of Figures

1.1 Static cantilever principle . . . 2
1.2 Resonant cantilever principle . . . 2
1.3 Amplitude response of vibrating cantilever . . . 4

2.1 Geometry of a two-layer cantilever . . . 8

3.1 Schematic diagram of chamber setup . . . 12
3.2 N_2 inlet valve setup . . . 14
3.3 Pumping speed curve . . . 15
3.4 Chamber pressure as a function of pumping time . . . 16
3.5 Chamber heating delay curves . . . 18
3.6 Temperature curves vs. control method . . . 19
3.7 Aluminum base for sample holder . . . 20
3.8 PGA socket on PCB for sample holder . . . 21
3.9 Ceramic PGA chip mount . . . 21
3.10 PZT-adapter for cantilever actuation . . . 23
3.11 Sample holder and video lens mount . . . 24
3.12 Chemical injection flange . . . 25
3.13 Vapor injection manifold . . . 26
3.14 Optical laser focusing setup . . . 28
3.15 Optical detection setup . . . 31
3.16 Calculated laser beam width and deflection . . . 32
3.17 Active area of PSD . . . 33
3.18 Video imaging lens systems . . . 38
3.19 Lens system spot diagrams . . . 38

4.1 Silicon dioxide cantilever chip . . . 44
4.2 Cantilever clamping (SEM) . . . 44
4.3 Gold coated cantilever chip on PCB . . . 46
4.4 Schematic of actuation and detection setup . . . 46
4.5 Lorentz curve and SHO response . . . 48

4.6 Modal shapes with identical deflection angles 50
4.7 Resonance frequencies of measurable modes 51
4.8 Q-factors vs. resonance frequencies 53
4.9 Q-factors vs. Au coating thickness in vacuum 56
4.10 Q-factors vs. Au coating thickness at 100 kPa 57
4.11 Resonance frequencies vs. pressure 58
4.12 General pressure dependence of Q-factors 61
4.13 Measured and modelled pressure dependence of Q-factors . . . 62
4.14 Uncoated resonance frequencies vs. temperature 63
4.15 Au coated resonance frequencies vs. temperature 65
4.16 Grain size of gold coating (SEM) 65
4.17 Uncoated Q-factors vs. temperature 66
4.18 Au coated Q-factors vs. temperature 67
4.19 Vacuum level vs. temperature 67

5.1 Structure of the four DNA-bases 73
5.2 Polymeric scheme of DNA 73
5.3 Test pattern for laser lithography 75
5.4 Fluorescence scans of the laser-exposed DNA 75
5.5 Cell for micro-fluidic integrated cantilever 76

6.1 Nanomass poly-Si cantilever (SEM) 78
6.2 Nanomass cantilever frequency response 79
6.3 Gold bead on microcantilever (SEM) 80
6.4 Point-mass position dependent resonance 82
6.5 In-plane cantilever with thermal heating actuation 83
6.6 Resonant response of in-plane cantilever 84
6.7 Micro-bridge resonator (SEM) 84
6.8 Resonant response of micro-bridge 85

B.1 Gaussian beam intensity distribution 91
B.2 Dimensions of propagatin Gaussian beam 91
B.3 Refraction of Gaussian beam 92

C.1 Image of the cantilever mesh model 94

D.1 3D visualization of vacuum chamber body 95
D.2 Top and front view of chamber body 96
D.3 Right side view of chamber body 97
D.4 Bottom plate of the chamber body 98
D.5 Mounting plate for vacuum chamber 99
D.6 Video-lens holder 100

E.1 PSD Pre-amplifier, diagram and print layout 103
E.2 PSD Difference-amplifier, diagram and print layout 105

F.1 LabVIEW user-interface for gain–phase analyzer 107
F.2 Program structure for gain–phase analyzer 108
F.3 LabVIEW user-interface for temperature/pressure control 110
F.4 Program structure for temperature/pressure control 111

List of Tables

3.1 Gaussian beam transformation data 29
3.2 Attenuation of laser beam 31

4.1 Measurement parameter space 45
4.2 Cantilever material data 45
4.3 Measured, analytical and simulated resonance frequencies . . . 52
4.4 Q-factors of coated– relative to uncoated cantilevers in vacuum 57

5.1 Masses of the four DNA-bases 72

C.1 Au coated cantilever layer data 93

G.1 List of abbreviations 112

Chapter 1

Introduction

The concept of a stick – held in one end and free to move in the other – may be one of man's oldest and most primitive tools. Through millennia of research and development, this tool has been refined to become one of the most delicate and sensitive instruments in present day micro- and nanotechnology, in the form of cantilevers.

Microcantilever sensors were introduced with the invention of the atomic force microscope (AFM) by Binnig et al.[1] in 1986; and development, characterization and application of micro- and nanocantilevers has since then become a continuously expanding, global field of research, mainly because of their potential as low-cost and high-sensitivity measurement probes.

1.1 Cantilever sensor operation

Cantilever sensors are currently used in two fundamentally different ways, which may be denoted as static mode and dynamic (resonant) mode.

In static mode, the deflection of a bending cantilever is measured as illustrated in figure 1.1. This deflection may be induced by an internal stress gradient – e.g. in bimorph cantilevers, subjected to a temperature change. Such bimorph structures are used in macroscopic as well as microscopic scale as thermostats [2, 3] or calorimeters [4]. The deflection may also be generated by a surface stress – e.g. as a result of molecular adsorption, in which case the cantilever may work as a chemical sensor [5], or simply as a sensor for measuring the surface stress itself [6].

The static mode of operation holds very promising potential for biomedical applications, where an array of nanocantilevers could be used to screen a blood sample for a number of specific constituents. In particular, detection of specific DNA-sequences could prove valuable for e.g. cancer research or

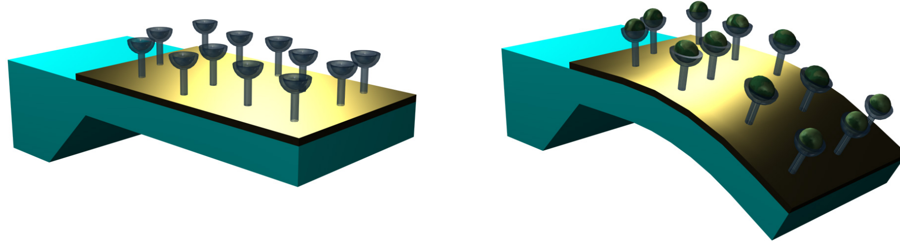

Fig. 1.1: Principle of static mode cantilever operation: A cantilever is functionalized with a receptor coating (left), which will adsorb specific chemical compounds, resulting in a surface stress that causes the cantilever to bend (right).

detection of biological warfare agents, and the area has therefore attracted much attention, both experimentally [7, 8] and theoretically [9].

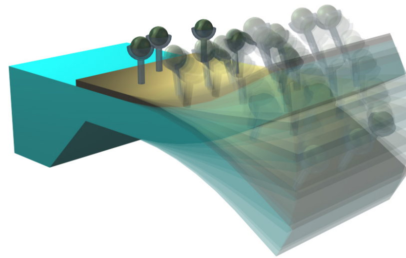

Fig. 1.2: Resonant mode cantilever operation: The functionalized cantilever is actuated into resonant vibration. The change in mass from the adsorbed molecules causes a shift in resonance frequency.

In contrast to static cantilevers, dynamic (or resonant) cantilever sensors (figure 1.2) react to a mass change rather than a stress change. In this mode of operation, the cantilever is actuated into vibration, and the physical vibration amplitude of the cantilever is monitored as a function of vibration frequency. Resonance frequencies are identified as peaks of maximal oscillation amplitude in the frequency spectrum.

As the spectral positions of the resonance frequencies depend on the cantilever geometry, material elasticity and mass, a change in mass will cause a shift in resonance frequency. When used as a mass detector, the cantilever surface can be coated with a functionalization layer for adsorption of specific chemical compounds. Adsorbed molecules will add to the mass of the cantilever and the resulting frequency shift can be detected.

Applications for resonant cantilever sensors include gas- or vapor-detection of e.g. mercury [10], ethanol [11] or relative humidity [12], and recently Ledermann et al.[13] reported on CO_2 detection of concentrations down to 330 ppm. In the biomolecular area, protein masses of specific antigens have been measured using cantilevers in liquid, with a sensitivity of 100 ng/ml [14], and even liquid in a channelled cantilever has been implemented by Burg et al.[15] with a surface density sensitivity of 10 ag/μm^2 on an channel surface of 53000 μm^2.

As the dimensions of the cantilevers decrease, the sensitivity increases, implying that resonant cantilever sensors have the future potential of detecting the mass of individual molecules. Current state–of–the–art includes demonstrated mass detection in the order of a few ag [16] and fabrication of cantilever sensors with sub-ag estimated mass sensitivities [16, 17].

This work is primarily concerned with issues regarding resonant cantilever operation, and unless otherwise specified, it is assumed in the following, that cantilevers are operated in resonant mode.

1.2 Resonant cantilever characterization

Several methods have been developed to actuate cantilevers and detect the resonant motion. The most commonly used are described in the review article by Stemme [18] and include electrostatic actuation and capacitive detection [19], which requires electrodes to be integrated parallel to the cantilever, and holds great promise for cantilevers in the nano-regime; piezoelectric actuation, which may be integrated in the cantilever structure [20] or applied as a separate piezo-ceramic element in physical contact with the cantilever chip; piezoresistive detection [21]; thermal actuation [22, 23], where the cantilever vibration arises from thermal fluctuations (Brownian motion); and optical detection [24], where the cantilever motion or position is probed by a laser beam.

The theoretical oscillation amplitude of a cantilever, as a function of actuation frequency near a resonance peak, is illustrated in figure 1.3. Increasing the mass of the cantilever will shift the resonance towards a lower frequency.

There are two ways of detecting this frequency shift. One is to measure the entire frequency spectrum around the peak and observe whether the peak has moved. This is the common method when characterizing the cantilever experimentally. The other method is to continuously monitor the amplitude of the cantilever at the frequency where the response curve has the steepest slope. A shift in resonance frequency will result in a change in the oscillation amplitude of the monitored frequency. This would be the detection method

used with a cantilever sensor working in continuous operation.

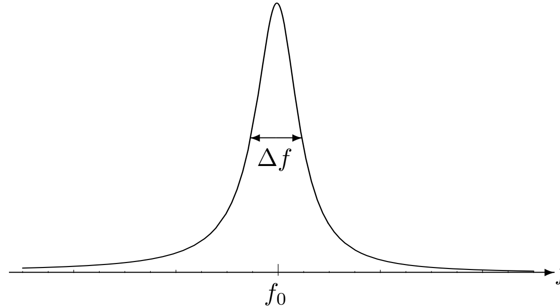

Fig. 1.3: Amplitude response of vibrating cantilever around resonance peak at f_0, as a function of oscillation frequency.

For any cantilever sensor, there are two properties of the frequency response that are of central importance: the position of the resonance frequency and the quality factor or Q-factor, given by $Q = \Delta f / f_0$, where Δf is the full–width half–maximum (FWHM) of the resonance peak.

An observed change in resonance frequency may not just be caused by adsorption of the type of molecule that the cantilever is designed to detect. The elasticity of the cantilever material is an important parameter that governs the resonant properties, and as the elasticity of any material is temperature dependent [25, 26], so is the resonance frequency. When the cantilever is vibrating in a fluidic medium, e.g. atmospheric air, the air that moves with the cantilever will add to its effective mass and lower the resonance frequency. Thus, the resonance frequency is also pressure dependent, as well as dependent on the type of gas or liquid it's surrounded by [27, 28]. Characterizing the temperature and pressure dependencies of the resonance frequency is therefore of great importance in order to be able to distinguish between an actual signal and a frequency drift caused by changes in the ambient conditions.

Regardless of the method of resonance frequency detection, the Q-factor is closely related to the detection sensitivity and resolution as described by Fadel et al. in [29, 30]. A high Q-factor is equivalent to a narrow peak and a steep slope, and a change in resonance frequency will therefore result in a distinct displacement of the resonance peak for high Q-factors, while being undetectable for low Q-factors. Like the resonance frequency, the Q-factor depends on temperature dependent material properties as well as ambient conditions such as pressure. and the characterization of these dependencies is another important issue in the development of micro- or nanocantilever sensors.

1.3 Multi-layer cantilevers

Most cantilever applications require that the cantilever consists of more than one material layer. As a coating layer, gold is widely used, due to the large selection of materials that can be adsorbed via thiol chemistry as described in recent review articles by Lavrik et al.[31] and Ziegler [32]. Besides from a gold layer, electrically conducting layers can be patterned and integrated into the cantilever for local heating [33], magnetomotive actuation [34] or piezoresistive readout of the deflection [35, 36].

The analytical theory describing the motion of a monolithic cantilever is commonly used [37]. For cantilevers with two or more layers, it is customary to use approximations for the effective modulus of elasticity as well as the mass density to estimate the resonance frequency [38], or to neglect the elastic properties of all but the thickest layer [39]. Although good agreement between approximations and experiments have been observed [27, 38], the validity when more than two layers are used has not been verified.

Since high precision measurements are required in many of the mentioned applications, a non-approximative approach would be very useful. Finite–element models are very accurate in predicting the resonance frequencies of cantilever modes, but it is still a time consuming calculation method.

As a step towards an accurate yet easily implemented method for calculating multi-layer resonance frequencies, the analytical theory of monolithic cantilevers has been extended to include any number of layers, as presented in chapter 2, and has shown to be in very good agreement with finite–element simulations.

1.4 Overview of the thesis

The work presented here has primarily been focused on the design and implementation of an experimental setup for characterization of micro- and nanocantilever devices. The central part of this setup is a custom built vacuum chamber with capabilities for temperature and pressure control, and with equipment for introduction of different gases and other chemical compounds.

The vacuum chamber was initially developed as part of an EU project called “Nanomass” [40]. The project took place in 2000–2004 as a collaboration between MIC and three other European research institutes. The main goal of the Nanomass project was to develop a resonant nanocantilever mass sensor integrated with a CMOS circuit for actuation and readout [19]. One of the responsibilities of MIC in this project was to characterize the final

mass sensor devices and present suitable applications. This was the primary purpose for the construction of the vacuum chamber.

In addition to the electrical interface to the chamber, which was required for control and characterization of the Nanomass devices, an optical detection system, based on the principle used in AFM, was implemented with the chamber setup, to enable laser-optical characterization of resonant devices, and make the setup more generally applicable.

As the construction of the vacuum chamber setup came to an end, an experimental project with focus on characterization of the resonant properties of gold coated cantilevers was initiated. Despite the frequent use of gold coatings, the effects of gold on the resonant properties of high–Q cantilevers have not been fully investigated.

By utilizing the capabilities for pressure and temperature control in the vacuum chamber setup, the thermal dependencies and effects of viscous damping on the resonant properties of silicon dioxide cantilevers with varying thicknesses of gold coatings was studied.

In chapter 2 the theory for an analytical model predicting the resonance frequencies of flexural modes of multi-layer cantilevers is deducted. A detailed description of the experimental setup with the vacuum chamber and optical detection system is given in chapter 3. The investigation of temperature-, pressure- and gold coating effects on the resonant properties of SiO_2 cantilevers is presented in chapter 4, with details of the experiment, and discussion of the obtained results. An experiment concerning detection of DNA by means of resonant cantilevers in a fluidic cell is described in chapter 5. The capabilities of the vacuum chamber and detection setup have been utilized by several members of the Bioprobes group at MIC for a number of different experiments, some of which are presented in chapter 6. Finally, some concluding remarks are given in chapter 7.

Chapter 2

Flexural eigenmodes of a multi-layer cantilever

The commonly used theory for the motion of a vibrating cantilever, as presented in [37], is well known, but is limited to the description of homogeneous cantilevers that consist of only one material (monolithic cantilevers). In many applications, the cantilevers used are structured in more layers, and the theory is not directly applicable. Previous theoretical work on non-monolithic resonant cantilevers has mainly been limited to bi-material cantilevers [41, 27, 38, 26], and even then, approximations have been used.

The most commonly used approximation is to estimate the Young's modulus as a weighted average [38]:

$$E \approx \frac{E_1 h_1 + E_2 h_2}{h_1 + h_2} \tag{2.1}$$

This is accurate when the neutral axis is not significantly altered compared to a homogeneous cantilever of the same thickness, which implies that $E_1 \approx E_2$ or that one layer must be much thinner than the other, e.g. a very thin coating layer.

The theory presented here is explicitly accounting for the mass and elasticity of all layers and is therefore relevant for calculations on more complex layered cantilever structures, such as for instance coated cantilevers with integrated piezoelectric or piezoresistive layers [20]. It is meant as an accurate and time-saving alternative to finite–element modelling (FEM). Its accuracy is confirmed in chapter 4 by comparison to FEM as well as experimentally obtained results.

2.1 Analytical theory

Consider a cantilever with rectangular cross-section, consisting in the z-direction of N layers with different heights (h_i), densities (ρ_i) and Young's moduli of elasticity (E_i). The different layers are uniform along the width (w) and length (ℓ) of the cantilever. The cantilever is clamped in one end ($y = 0$), and is otherwise free to move in the z-direction, as sketched in figure 2.1. A deflection of the cantilever will result in a bending, which creates an internal moment (torque), M, given at any point along the cantilever length by [37]

$$M = \mathrm{w}\int_h \sigma_{zz} \cdot (z - z_0)\mathrm{d}z = -C\mathrm{w}\int_h E \cdot (z - z_0)^2\mathrm{d}z \tag{2.2}$$

where $\sigma_{zz} = -C\,E \cdot (z - z_0)$ is the tensile stress due to the curvature (C), E is Young's modulus of elasticity, and the integration is taken over the height (h) of the entire cantilever. z_0 is the position of the neutral axis (i.e. the part of the cantilever which retains its original length during bending). For a layered cantilever, E is a discontinuous, piecewise constant function of z.

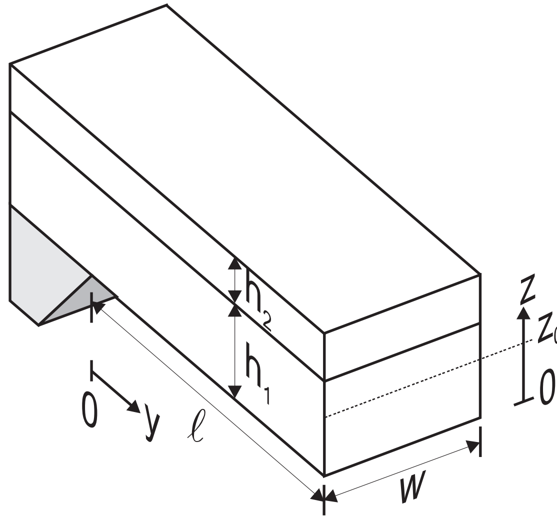

Fig. 2.1: Illustration of the geometry of a two-layer, clamped cantilever.

The neutral axis can easily be determined as the solution to

$$\begin{aligned} &\mathrm{w}\int_h \sigma_{zz}\,\mathrm{d}z = 0 \\ \Leftrightarrow &\int_h E\cdot(z-z_0)\,\mathrm{d}z = 0 \end{aligned} \tag{2.3}$$

which states that the integrated tensile stress over the cross-section of the cantilever must be zero. This equation must hold, as there would otherwise be a net longitudinal force, straining the cantilever.

The equation of motion, governing the flexural modes of the cantilever, can be derived from Newton's 2nd law:

$$\begin{aligned} \mathrm{w}\sum_{i=1}^{N}(h_i\rho_i)\frac{\partial^2\zeta(y)}{\partial t^2} &= \frac{\partial^2 M}{\partial y^2} \\ &= -\mathrm{w}\frac{\partial^4\zeta(y,t)}{\partial y^4}\int_h E\cdot(z-z_0)^2\mathrm{d}z \end{aligned} \tag{2.4}$$

where $\zeta(y,t)$ is the time dependent z-deflection at any point along the cantilever length. In the derivation of equation (2.4), the expression in equation (2.2) for M has been used in conjunction with the small deflection approximation of the curvature [37]

$$C \approx \frac{\partial^2\zeta}{\partial y^2} \tag{2.5}$$

The equation of motion can be solved by assuming harmonic, modal solutions of the form

$$\zeta(y,t) = \zeta(y)\cos(\omega_n t + \theta) \tag{2.6}$$

where ω_n is the angular resonance frequency of the nth mode, and θ is an arbitrary phase. Equation (2.4) then simplifies to

$$\frac{\mathrm{d}^4\zeta(y)}{\mathrm{d}y^4} = \kappa_n^4\zeta(y) \tag{2.7}$$

where the modal parameter κ_n is defined as

$$\kappa_n{}^4 \equiv \frac{\omega_n^2\sum_{i=1}^{N}(h_i\rho_i)}{\int_h E\cdot(z-z_0)^2\mathrm{d}z} \tag{2.8}$$

The boundary conditions for a clamped cantilever are

$$\zeta(0) = 0\ ,\quad \zeta'(0) = 0\ ,\quad \zeta''(\ell) = 0\ ,\quad \zeta'''(\ell) = 0 \tag{2.9}$$

stating that at the clamped end, the deflection and slope must be zero, and that there is no moment or shear force acting at the free end. Applying these boundary conditions, the solutions to equation (2.7) take the form of the flexural eigenmodes

$$\zeta(y) = A(\cos\kappa_n y - \cosh\kappa_n y) + B(\sin\kappa_n y - \sinh\kappa_n y) \tag{2.10}$$

with the modal restrictions

$$\frac{A}{B} = \frac{\cos\kappa_n\ell + \cosh\kappa_n\ell}{\sin\kappa_n\ell - \sinh\kappa_n\ell} = -\frac{\sin\kappa_n\ell + \sinh\kappa_n\ell}{\cos\kappa_n\ell + \cosh\kappa_n\ell} \tag{2.11}$$

where the second equality implies that

$$\cos\kappa_n\ell\cosh\kappa_n\ell + 1 = 0 \tag{2.12}$$

The first five solutions of this equation are obtained numerically as

$$\kappa_n\ell \simeq 1.8751,\quad 4.6941,\quad 7.8548,\quad 10.9955,\quad 14.1372 \tag{2.13}$$

For higher order modes, the very accurate approximation

$$\kappa_n\ell \simeq \pi(n - \tfrac{1}{2}) \tag{2.14}$$

may be used. The resonance frequencies f_n can be obtained from equation (2.8) as

$$f_n = \frac{\omega_n}{2\pi} = \frac{(\kappa_n\ell)^2}{2\pi\ell^2}\left(\frac{\int_h E\cdot(z-z_0)^2\mathrm{d}z}{\sum_{i=1}^N(h_i\rho_i)}\right)^{1/2} \tag{2.15}$$

For a homogeneous, single–material, rectangular cantilever, this expression reduces to the well-known

$$f_n = \frac{(\kappa_n\ell)^2}{4\pi}\frac{h}{\ell^2}\left(\frac{E}{3\rho}\right)^{1/2} \tag{2.16}$$

Chapter 3

Vacuum chamber for cantilever characterization

A vacuum chamber and laser-optical detection system was designed and constructed for the purpose of characterizing cantilever sensors in a controlled environment. This chapter describes the details of the design and functionality of the setup.

The structure of the vacuum chamber body is described in section 3.2. Section 3.3 is concerned with the basic equipment of the vacuum chamber, such as gas inlet, pump, temperature- and pressure-control. The more specialized equipment for cantilever characterization, that has been designed for the chamber is described in section 3.4. Section 3.5 is dedicated to the laser-optical detection system, and section 3.6 gives a discussion of the steps that may be taken to improve the functionality of the experimental setup.

3.1 Introduction

In relation to the EU project "Nanomass" [40], where MIC had the responsibility to characterize the fabricated cantilever devices, a vacuum chamber and detection system was constructed. The main focus in the construction process was to make the chamber versatile and easily configured for new experiments.

For characterization of the Nanomass devices, only electrical interconnections to the chamber were required, as the cantilevers were integrated with CMOS circuitry for actuation and signal detection. The laser-optical detection system was implemented as an additional method of detection, to enable characterization of a wide range of the resonant structures that are designed and fabricated at MIC.

The primary purpose for the chamber was

- to be able to measure the resonant properties (i.e. resonance frequency and Q-factor) of nano- and micro-cantilevers at different temperatures and pressures,
- to functionalize the cantilevers by introducing chemicals such as e.g. silanes that will bind to the cantilever surface,
- to do mass detection measurements by introducing chemicals that will adsorb onto the functionalization layer.

The vacuum chamber setup is illustrated schematically in figure 3.1, and technical drafts of the chamber and custom designed equipment are collected in appendix D.

3.2 Vacuum chamber body design

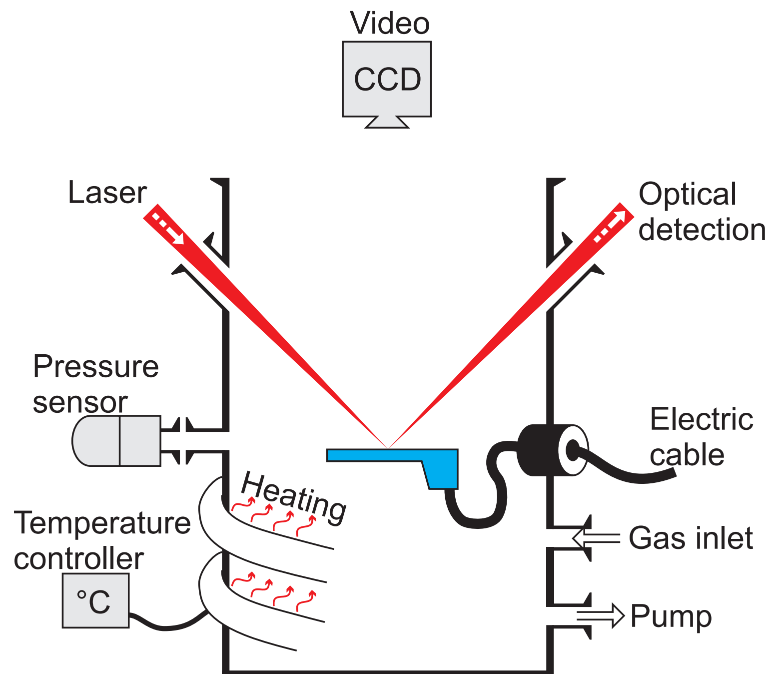

Fig. 3.1: Schematic diagram of the vacuum chamber setup.

The chamber was decided to be constructed in stainless steel rather than aluminum, mainly because of the outgassing rate of aluminum, which is 2–3 times higher than that of stainless steel [42] and due to the small chemical reactivity of stainless steel.

The size of the chamber should be minimized, as a smaller volume requires less time to pump down. The limiting factor for the size was the number of flanges required, as the cantilever chips that would be placed in the chamber are at most a few centimeters across. A tubular shaped chamber body with an inner diameter of 150 mm proved to be sufficient.

Connection of external equipment to the chamber was decided to be done through KF flanges as these are easy to use and highly standardized. When using Viton O-rings, these flanges will sustain temperatures up to 150 °C.

Gas inlets were designed as Swagelok VCR 1/4" face seal fittings with silver plated metal gaskets.

Figure D.2 in appendix D (p.96) shows a technical draft of the vacuum chamber. The three VCR flanges in the bottom are meant as inlets for different gasses (see section 3.3.1). In addition to the gas inlets,a KF DN-16 flange for the pump (section 3.3.2) and one KF DN-25 flange for a pressure sensor (section 3.3.3) have been placed in the back of the chamber body. The VCR flange at the top (chamber front) is for mounting a vapor injection manifold (section 3.4.3). The large KF DN-40 flange has been fitted with an electrical feed-through using a vacuum tight LEMO model SWH series 5S coupler mounted with a 48-pin hermaphroditic multicontact. A couple of LEMO model FFA.5S straight plugs may then be plugged into this coupler providing electrical connections from the sample inside the chamber to any measurement equipment. The horizontally mounted KF25 flange is for any auxiliary equipment that needs to be connected to the chamber, e.g. a mass spectrometer for analyzing the gas composition in the chamber. The two 45° mounted KF DN-40 flanges are fitted with glass blanks for optical characterization (section 3.5). Loading of samples or equipment into the chamber is done through the top, which is fitted with an ISO-K DN-160 blank flange, also with an encased glass plate for visual or video inspection of the sample (section 3.4.2).

The entire chamber body has been helium leak tested to a pressure of 4 bar. The inner volume of the chamber and flanges when no equipment has been inserted is approximately 3640 cm^3. Measurements show a pressure increase rate of 6.5 mPa/s when the chamber is pumped down to a vacuum level and the pump valve is closed. This corresponds to a leak rate of about 24 mPa l/s.

3.3 Basic equipment

The basic features of the chamber are described in the following sections. This includes the system for gas inlet (section 3.3.1), the properties of the pump (section 3.3.2), the pressure sensors (section 3.3.3) and the implementation of temperature control (section 3.3.4).

3.3.1 Gas Inlet

The three VCR gas inlets are placed in the back of the chamber, so the pipes are not in the way when the chamber is in use, and at the bottom of the chamber – below the sample, in order to have the gas molecules scattered off the sample mount, thus avoiding a direct jet of gas onto the sample.

One inlet is permanently connected to a N_2 supply line through a Swagelok bellows valve (model SS-4BKT V51) and an Air Liquide pressure reducer as sketched in figure 3.2. The bellows valve has only two settings: open and closed, while the pressure reducer allows the flow to be varied continuously. The pressure reducer is not capable of shutting off the flow entirely.

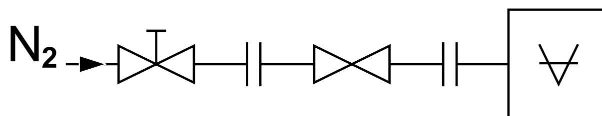

Fig. 3.2: N_2 inlet valve setup (from left to right): The flow of N_2 is limited by a pressure reducing valve, followed by a bellows valve (only *on/off*), immediately before the chamber body.

The order of the two valves allows for instantaneous shutoff of the N_2 flow into the chamber, but has the disadvantage that the pressure in the pipe section between the two valves will build up when the bellows valve is closed. An initial burst of gas will therefore be let into the chamber when reopening the bellows valve. This burst could be avoided by switching the order of the two valves, which, however, would introduce a different disadvantage, as the N_2 pressure between the two valves will be high (supply line pressure) when the bellows valve is open. The high pressure N_2 between the valves will therefore continue to flow into the chamber after closing the bellows valve and thus prevent instantaneous shutoff. The ideal solution would naturally be a mass flow controlled valve with shutoff ability. For financial reasons this has not been implemented though.

3.3.2 Vacuum Pump

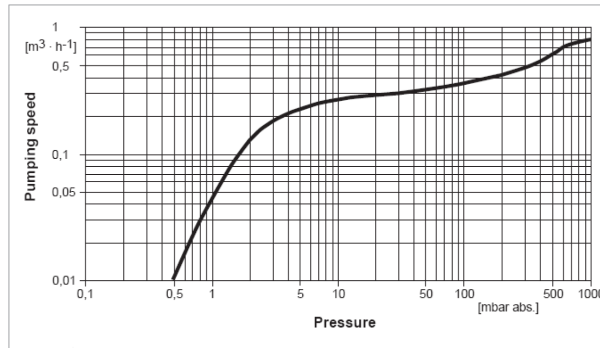

Fig. 3.3: Pumping speed curve of the DIVAC 0.8 LT. (Source: Leybold product catalog)

The vacuum chamber was required to pump down to a pressure of less than 50 Pa, in order to have negligible air damping of the Nanomass cantilevers. This is a relatively high vacuum level, which can be obtained without installation of a turbo pump. To avoid oil and hydrocarbon contamination of the chamber, a Leybold diaphragm pump model DIVAC 0.8 LT was installed. All parts of this pump that are in contact with the gas are coated with PTFE (Teflon), FFPM (Kalrez) or PVDF (Solef), making it highly resistant against chemically reactive gasses. The 4 pump heads enable it to reach a final pressure of less than 50 Pa in 10 to 20 minutes, as illustrated in figures 3.3 and 3.4.

For attaining a lower vacuum level, the diaphragm pump may be used as a backing pump for a turbo pump, which can therefore easily be installed.

3.3.3 Pressure Sensor

The pressure sensor is a HPS Series A900 vacuum sensor system with a DualTrans+ transducer, consisting of a Piezo transducer and a MicroPirani transducer. The Piezo transducer is a solid state sensor, which measures the mechanical stress, due to pressure, in a silicon membrane. It has an absolute accuracy of 200 Pa in the range from 10 Pa to 400 kPa, and outputs a voltage directly proportional to the pressure. The MicroPirani transducer is based on the measurement of thermal conductivity. It has a relative accuracy of 5 % of the measured value over the range from 1 mPa to 100 kPa. To obtain the most accurate pressure reading at any pressure, the Piezo transducer should therefore be used for pressures at and above 4 kPa, and the MicroPirani

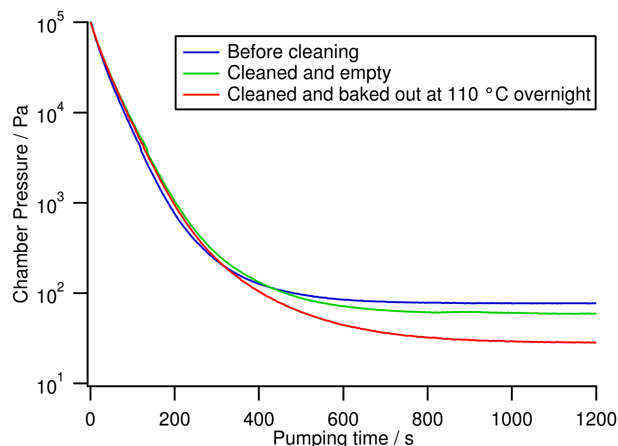

Fig. 3.4: Measurement of the chamber pressure as a function of pumping time. Terminal pressures are 77 Pa before cleaning the chamber, 59 Pa after cleaning but before baking, and 28 Pa after the chamber has been baked.

transducer for pressures below 4 kPa. The MicroPirani transducer provides an output voltage in the range $0 - 10$ V, which depends on the pressure as well as the type of gas. A 5-parameter analytic conversion formula as well as a parameter table has been provided by the manufacturer.

3.3.4 Temperature Control

Description

To control the temperature of the chamber, the exterior surface of the chamber body has been covered with an electrical heating ribbon. Direct heat transmission is not easily implemented on cantilever chip samples, and at low pressures, heat transfer by convection is almost negligible. The only way of heating the interior of the chamber is therefore by radiation, and for this, the heating ribbon is quite efficient, as illustrated in figure 3.5.

The ribbon is connected to a solid state relay which is driven by a CAL 9400 autotune temperature controller by CAL Controls. It is equipped with Proportional–Integral–Derivative (PID) functionality, which is a necessity due to the very slow and nonlinear response of the chamber temperature to heat pulses from the ribbon. The controller is also equipped with a RS-232 serial interface, enabling it to be connected to a computer for programmatic control and readout of temperature data.

The temperature sensor connected to the controller may be any con-

ventional thermocouple or resistance thermometer. A thermocouple in the vacuum chamber would require a special feed-through flange with electrodes consisting of the same metals or alloys as the thermocouple. Otherwise, the temperature gradient across the chamber wall would give rise to a nonlinear and temperature-dependent error in the temperature reading. The simpler solution, to use a resistance thermometer detector (RTD), was therefore used. The detector was chosen to be a U.S. Sensor thin film platinum RTD (Pt100 type) with an accuracy of 0.06 % at 0 °C, corresponding to 1/2 DIN of the DIN 43760 standard.

Adjusting the controller

The CAL9400 operates on the PID control principle. In general, the PID controller has a three parameter transfer function, with a proportional gain, an integral gain and a derivative gain, which determines the heating level at any time based on the target temperature and the temperature-history. The heating level is represented in the controller as a percentage of full power, and as the solid state relay only allows the heating ribbon to be *on* or *off*, a heating level below 100 % is accomplished by turning on the heat in the corresponding fraction of the *cycle-time*, which can be set manually between 0.1 s and 81 s. The reason for choosing a longer cycle time is to reduce the wear of a mechanical switch or relay. As the solid-state relay has no moving parts, the cycle-time has been set to a medium low value of 5 s.

A measurement of the temperature response of the chamber is displayed in figure 3.5. The heating ribbon was set to full power at time $t = 0$ s, where the chamber was at room temperature, and turned off after exactly 240 s. This was done three times: at atmospheric pressure with a RTD placed up against the chamber wall; at atmospheric pressure with the RTD in the centre of the chamber; and finally in vacuum with the RTD in the centre.

The results show a significant difference in temperature response, which is best seen by observing the position of the maximum peak temperature relative to the time when power is turned off. At the wall, the temperature peaks after a 2 min delay. In the centre at atmospheric pressure, a delay of about 7.5 min is observed, while the lack of heat conduction in vacuum results in a delay of almost 10 min.

It was found that a steady-state wall temperature of 140 °C requires a constant heating power of 23 %, which results in a stable temperature of approximately 97 °C in the centre of the chamber.

The very long delays present difficulties in controlling the temperature in the centre of the chamber precisely. And because of the large temperature difference between the chamber wall and the centre, it serves no practical

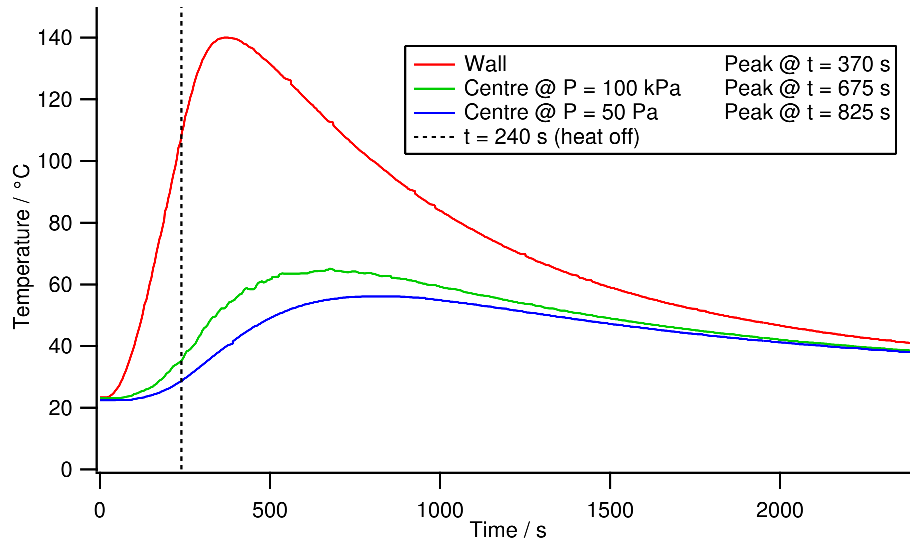

Fig. 3.5: Measurement of the temperature in the chamber as a function of time, when the heat is turned on at t=0 s and off at t=240 s. The temperature curve has been measured at atmospheric pressure: with a RTD close to the chamber wall, and with a RTD in the centre of the chamber; and at vacuum level with the RTD in the centre.

purpose to use the wall temperature as input for the controller.

Figure 3.6 illustrates the temperature response of the chamber centre in vacuum when heating and cooling between 30 °C and 70 °C. Changing the temperature can be done by adjusting the setpoint of the controller or by making the controller do a temperature ramp. The setpoint method results in a large temperature difference between the setpoint and the actual temperature. When heating, the proportional and integral gains therefore cause the controller to overshoot to 78 °C. When cooling on the other hand, the differential gain overcompensates for the initially steep cooling rate, resulting in an overall cooling rate that is unnecessarily slow.

The temperature control is slightly improved by using the ramp method. Because the temperature is adjusted at all points of both the heating and the cooling curves, the temperature controller is closer to an *equilibrium* condition, and the gain parameters are not *out of hand*.

In these temperature control tests the controller has been limited to 23 % output, (the power required to maintain a stable wall-temperature of 140 °C), in order to avoid the overheating of the chamber wall that would otherwise have occurred.

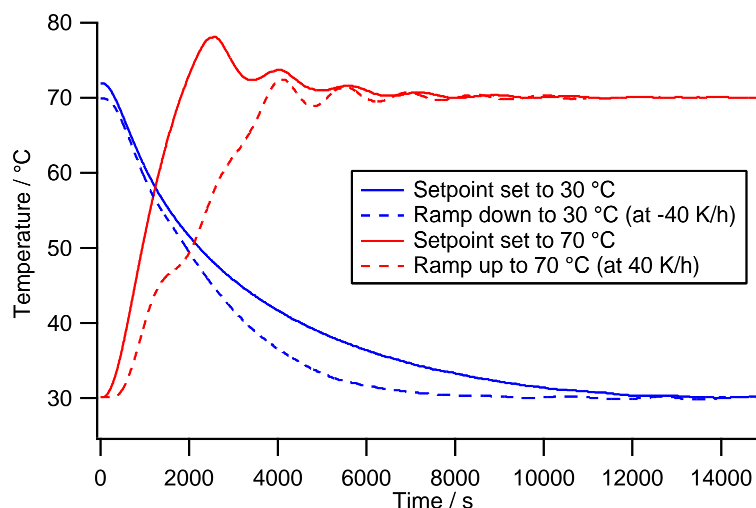

Fig. 3.6: Temperature change in the centre of the chamber at vacuum level for two different temperature control methods: Instant change in setpoint (target) temperature, and controlled temperature ramps (with slopes set to 40 K/h).

3.4 Special equipment

In order to do characterization of cantilevers in the chamber, a set of specialized equipment has been designed and implemented for the chamber setup. The design of a sample holder, that provides electrical connections to the cantilever chips, and acts as a stable platform for the sample relative to the laser focus, is described in section 3.4.1. Section 3.4.2 provides the details of an optical system that enables video inspection of the sample in the chamber. Characterization of the sensitivity of chemical cantilever sensors by inlet of chemical vapor has been implemented as a vapor injection manifold, described in section 3.4.3.

3.4.1 Sample holder & electrical connections

A sample holder has been designed to facilitate both optical and electrical characterization. The sample holder consists of an aluminum base, designed to have a height that ensures that the cantilever sample will be positioned in the centre of the chamber, 65 mm above the chamber floor. This coincides with the intersection of the center axes of the two 45°-angled optical flanges, and is therefore the intended optimum position for the laser focus. Figure 3.7 shows a sketch of the aluminum base, mounted at the bottom of the chamber.

Together with the printed circuit board (PCB) and pin grid array (PGA) socket, sketched in figure 3.8, the sample holder enables easy positioning and stable electrical connections for a cantilever chip mounted on a corresponding PGA-chip.

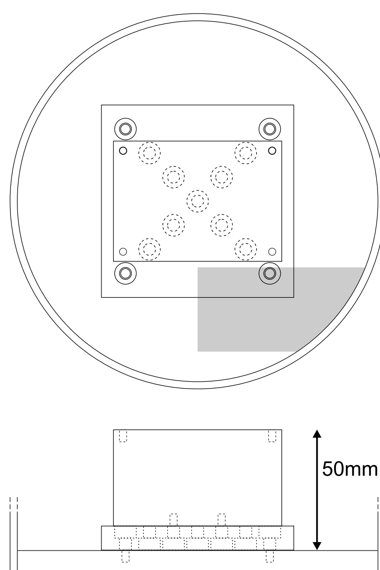

Fig. 3.7: Technical draft of the aluminum base for the sample holder. The grey area indicates the position of the LEMO plug.

The PCB part of the sample holder, shown in figure 3.8, is wired to the 48-pin hermaphroditic LEMO plug using 36 of the conductors in a 56-conductor Habia Cable (type: ZN 2419 SSTZ 28x2) capable of sustaining temperatures up to 150 °C. The PCB is fitted with a 121-pin PGA socket from Advanced Interconnections; the terminals are gold plated and the insulator is made of molded polyphenylene sulfide with a melting point above 300 °C. The 121-pin PGA footprint matches that of a chip mount constructed for a scanning electron microscope (SEM) in the Danchip cleanroom facility, so that chip-mounted samples may be characterized in both the SEM and the vacuum chamber. Of the 121 available terminals in the PGA, the 28 that are connected to the PCB have been selected **a:** from the outer rim of the footprint, to simplify the PCB circuit-layout, and **b:** in a way that ensures adequate spacing between the bonding pads on the ceramic PGA chip mount as much as possible, as seen in figure 3.9. The number of connected bonding pads, 28, was chosen because the Nanomass chip circuits each require 7 connections for actuation and readout. With 28 connections, 4 chips may be bonded onto one chip mount and characterized at a time.

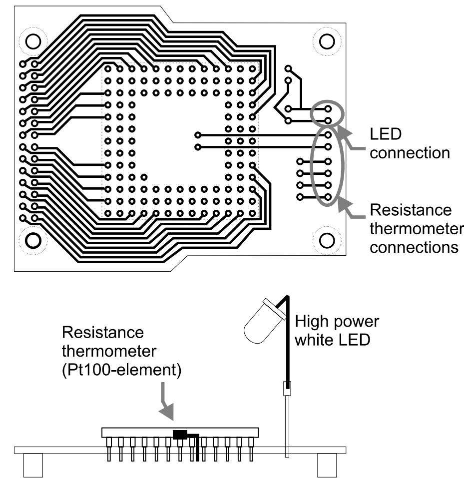

Fig. 3.8: Layout of the printed circuit board (PCB) and pin grid array (PGA) socket of the sample holder.

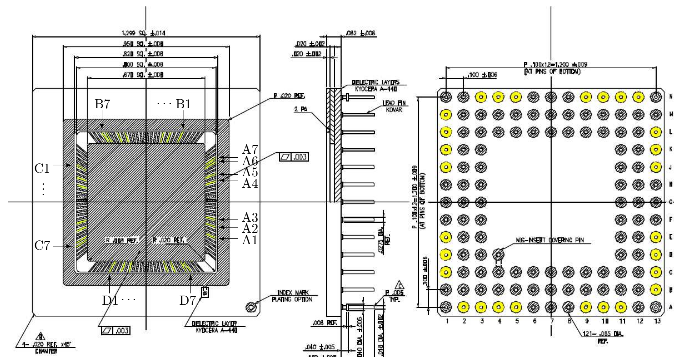

Fig. 3.9: Technical draft of ceramic PGA chip mount: Spectrum Semiconductor Materials Inc. P/N CPG12006. The bonding pads and corresponding terminal leads that have been wired to the PCB socket (fig. 3.8) are highlighted.

In addition to the PGA socket, the PCB contains two white high power LED's for illumination of the sample. This is useful for optical characterization when positioning the laser spot. Without illumination, only the laser spot is visible on the video monitor.

Three RTD's can be fitted onto the PCB. One is mounted in a permanent position in the centre of the PGA socket, directly underneath the chip mount. This will provide the best possible indication of the sample temperature.

Another RTD has been connected using a 20 cm long cable, enabling it to be placed anywhere in the chamber. The active RTD is selected by a switch on the mounting box of the CAL 9400. Changing the active RTD when the CAL 9400 is controlling the temperature, introduces a problem, however, in that the controller will attempt to compensate for the instant change in temperature because of the strong derivative gain factor that is induced.

On the outside of the chamber, the 36 used conductors from the LEMO plug are wired to a connection board where external equipment may be connected.

The conductors in the main cable are not shielded individually; neither do the LEMO plugs and feed-through provide individual shielding, which means that noise may occur because of cross-talk between individual conductors. The CAL 9400 temperature controller has been identified as a strong noise source, and for the sensitive electrical measurements of the Nanomass chips, the controller has been turned off.

In order to be able to actuate *passive* cantilevers (i.e. cantilevers that are not fabricated with an on-chip actuation mechanism, a chip holder with capabilities of piezoelectric actuation has been constructed (shown in figure 3.10). It fits into the PGA socket and acts as an adapter between the PGA and a flat–flexible–cable (FFC) connector which can be used for 0.4 mm thick PCB's as the one shown in figure 4.3 on page 46. These PCB's can then be used as a base onto which a chip containing free hanging cantilevers for out-of-plane oscillation may be fixed by e.g. epoxy glue. The six electrical connections may be utilized for e.g. piezo-resistant readout. When the PCB is fastened to the FFC connector, it will be in close contact with a Noliac A/S piezo-electric ceramic linear transducer element (PZT), which may be driven by the output of a lock-in amplifier or gain-phase analyzer, as described in detail in section 4.2.5.

3.4.2 Video inspection

Visual inspection of a sample in the chamber is a necessity in optical detection for focusing and positioning the laser spot onto the cantilever to be characterized.

For this purpose a Panasonic (model GP-KR222) color CCD camera is being used. A mounting post has been constructed to hold the camera centered above the chamber, pointing down through the inspection window of the top flange. The mounting post allows for the camera to be moved in the horizontal plane and adjusted up and down for focusing.

The camera has an objective with an object plane that is fixed in a distance of 80 mm. This introduces a problem in that the sample is positioned

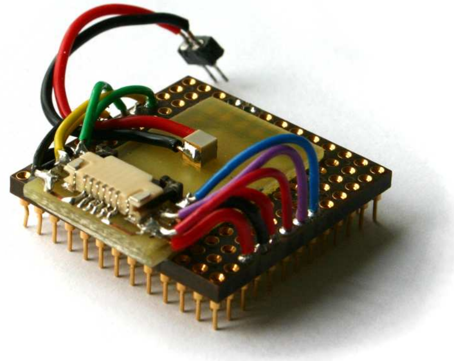

Fig. 3.10: PZT-adapter, mounted with a ceramic piezoelectric transducer for actuation of *passive* cantilever chips.

about 15 cm below the top flange. To solve this, a lens mount has been constructed as shown in figure 3.11. The mount is fitted with a $f = 50$ mm biconvex lens located 80 mm above the sample, thus creating an image of the sample 133 mm above the lens. This image is floating 45 mm above the glass surface of the top flange, enabling the camera to focus on it. A schematic of the imaging lens is shown in figure 3.18 a).

The object size that is captured by the camera ranges from 6 mm×4.8 mm down to 1 mm×0.8 mm depending on zoom level. This gets displayed on a 600×480 pixel monitor, giving a resolution of 10 to 1.7 μm per pixel. The magnification by 133 mm/80 mm = 1.66 of the lens further enhances this resolution to 6 to 1 μm per pixel.

The single biconvex lens is the simplest choice for projecting an image of the sample onto the camera object plane. It has proven functional despite the problem of optical aberrations in a single spherical lens. Theoretically, the lens only makes a perfect projection of rays that travel on the optical axis. Any off-axis rays or object points are subject to aberrations, which implies that in praxis the image gets blurred. To minimize this image distortion, the lens mount has been constructed to enable horizontal displacement of the lens, so that it may be centered directly above any point of the sample prior to closing the chamber. This has proven necessary in order to get a useful video image, as all off-axis points are heavily distorted – primarily by chromatic aberrations. The experiments on cantilever chips, described in chapter 4, showed that 10 μm wide cantilevers are barely visible on the minimum zoom level.

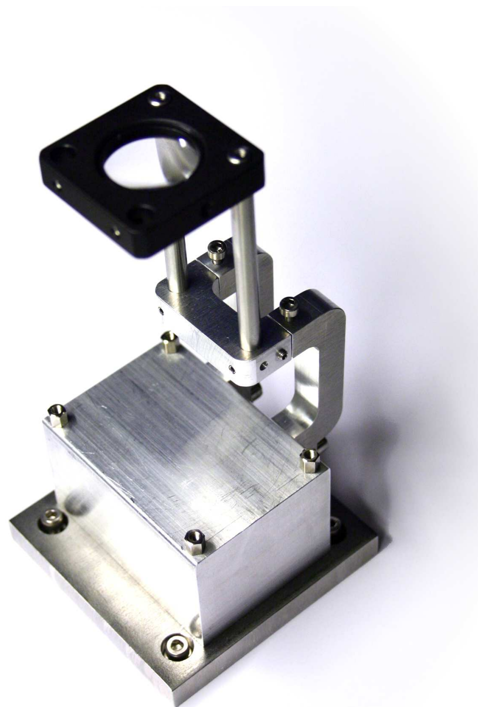

Fig. 3.11: Picture of the sample holder aluminum base and the lens mount for displacing the object plane of the video camera objective to the position of the sample.

3.4.3 Vapor Injection

For characterization of functionalized cantilever sensors, the cantilever must be exposed to the chemicals to be adsorbed and detected. This requires an injection system connected to the chamber, so that chemicals can be introduced into the chamber while it is pumped down to vacuum level.

A simple method for chemical injection is to inject the chemical as a liquid into the chamber, where it will evaporate in the low pressure. A blank DN-25 flange was constructed by Erik Wenzel of Wenzel Vakuum Teknik ApS, with a 3 mm hole and a replaceable viton membrane, as shown in figure 3.12. A chemical can be injected through the membrane by use of a syringe and needle, and if the syringe is left in the perforated membrane, no significant leak was observed. In fact, two such injections could be done in the same membrane.

This very simple approach has a few fundamental limitations though:

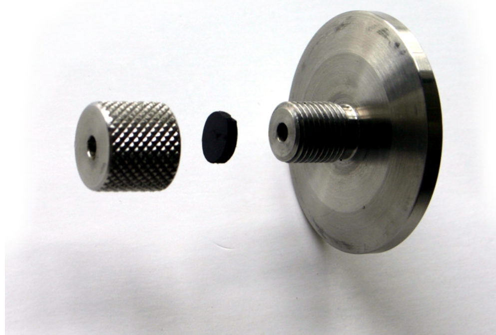

Fig. 3.12: Picture of the KF DN-25 flange with a 3 mm Ø bore for chemical injection by syringe and needle, sealed with a replaceable viton membrane and finger screw cap.

1. The penetrated membrane does not hold pressure once the syringe is removed. After a maximum of two injections, the membrane therefore needs replacement which involves opening the hole in the flange and exposing the chamber to atmospheric pressure.

2. After injection, the chemical will be in liquid phase in the bottom of the chamber, and the chamber will be filled with the chemical at its vapor pressure at the current temperature. This will only be altered by pumping out the chamber, until the injected amount of liquid has evaporated entirely and is being pumped out.

3. Precise control of the pressure by injection of only the amount of liquid needed to obtain a specific pressure below the vapor pressure is practically impossible with a standard syringe and needle. An example concerning acetone (C_3H_6O) demonstrates this: The vapor pressure of acetone is 24.6 kPa at 20 °C [43]. Assuming that acetone follows the ideal gas law, $PV = nRT$, where $R = 8.3145$ J/(mol K) is the gas constant, and $V = 3640$ cm^3 is the inner volume of the chamber, the amount of acetone needed to obtain $P = 24.6$ kPa at $T = 20$ °C is $n = 0.0367$ mol. With a molar mass, $M = 58.08$ g/mol, and a density $\rho = 790$ kg/m^3 [44], the injected volume of liquid is $V_{\text{liq}} = 2.7$ ml.

   This volume can easily be injected with a standard syringe, and smaller volumes too – e.g. 0.1 ml, enabling proof–of–principle experiments to verify a cantilever sensor's ability to detect acetone. However, the detection limit of concentration of a state–of–the–art detector will not be characterized by this method of injection.

For experiments with a greater demand on vapor concentration control and multiple injections – perhaps even of different chemicals, the limitations of the membrane-flange necessitate a more advanced method for chemical introduction. The vapor injection manifold shown in figure 3.13 was therefore constructed.

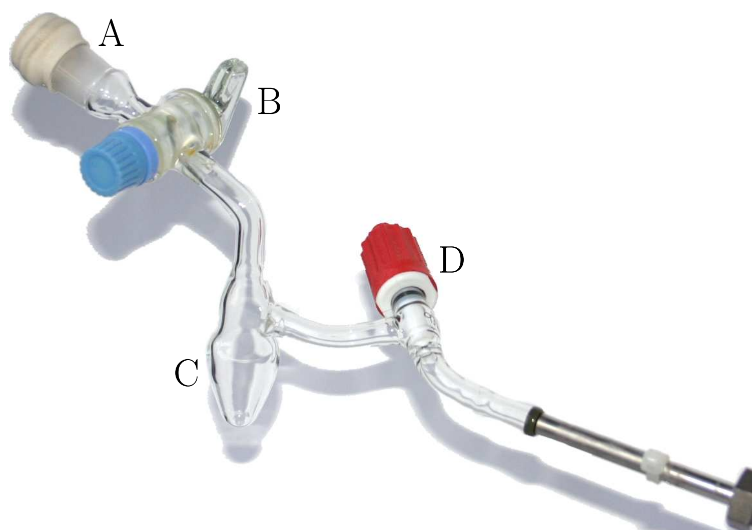

Fig. 3.13: Manifold for injection of chemical vapor in small concentrations. A: Latex membrane, B: Outer valve, C: Chemical manifold, D: Vacuum proof teflon valve.

In this device, liquid chemicals may be injected through the membrane (A) and outer valve (B) into the manifold (C), where it will evaporate until the vapor pressure is reached. The high vacuum proof teflon valve (D) may then be opened to let in the amount of vapor needed. A small opening of the valve will expectedly allow for very precise control of the chamber pressure up to the chemical vapor pressure. A greater vapor pressure may be obtained by heating up the chamber and manifold. In this case, all parts of the chamber must be at an equal or higher temperature than the manifold to avoid condensation of the chemical on the walls or flanges. The orientation of the teflon valve ensures tight sealing of the chamber. The sealing of the manifold to the outside atmosphere is not specified, but a significant pressure difference between the manifold and the room atmosphere may cause a leak. Hazardous chemicals should therefore be avoided or only used with the entire chamber and manifold placed in a fume hood. The vacuum grease in the outer valve will melt at temperatures over 60 °C, so heating of the manifold must be local. The teflon valve will sustain temperatures up to 150 °C.

3.5 Optical detection system

3.5.1 Introduction

A laser-optical system was designed and implemented for characterizing the frequency response of resonant cantilevers. The principle is to focus the laser beam onto the cantilever which will reflect the laser at an angle that depends on the deflection (bending) of the cantilever. A position sensitive photo-detector (PSD) is then used to measure the deflection of the laser beam and thus the deflection of the cantilever. When the cantilever is vibrating, the PSD will generate an AC current with an amplitude proportional to the cantilever's physical deflection amplitude. The principle is similar to that used in atomic force microscopy, developed by Meyer et al.[24].

By driving the actuator mechanism of the cantilever with the frequency output of a gain-phase analyzer (GPA), and connecting the PSD output to the GPA input, a frequency sweep can be performed, where the cantilever is put in motion at a range of frequencies and the amplitude and phase-response of the cantilever vibration can be measured. If a resonant mode of the cantilever is excited within this frequency range, it will show up on the detected signal as a positive amplitude peak accompanied by a 2π phase shift.

The optical setup consists of two parts: The focusing part which guides the laser and focuses in onto the cantilever, and the detection part which collects the reflected light from the cantilever, detects it and amplifies the detector signal. The following two sections will discuss these parts individually.

3.5.2 Laser focusing

The laser focusing setup is sketched in figure 3.14. The laser beam is redirected on the optical table by the mirrors M1 and M2, expanded and collimated by the lenses L1 and L2 and filtered for noise through the pinhole PH and the iris I1. The collimated beam is raised vertically and pointed down into the chamber by the mirrors M3 and M4 and focused onto the sample by the lens L3. Details of the individual components are described in the following:

HeNe Laser The laser is a Spectra-Physics Stabilite model 120 S helium–neon laser, with an output effect of 7.8 mW at the wavelength $\lambda = 632.8$ nm. The waist width, w_0, has been measured by pointing the laser to a wall at the distance $d = (41.15 \pm 0.05)$ m, and measuring the spot radius on the wall, $w(d) = (33.5 \pm 1)$ mm. This gives a divergence

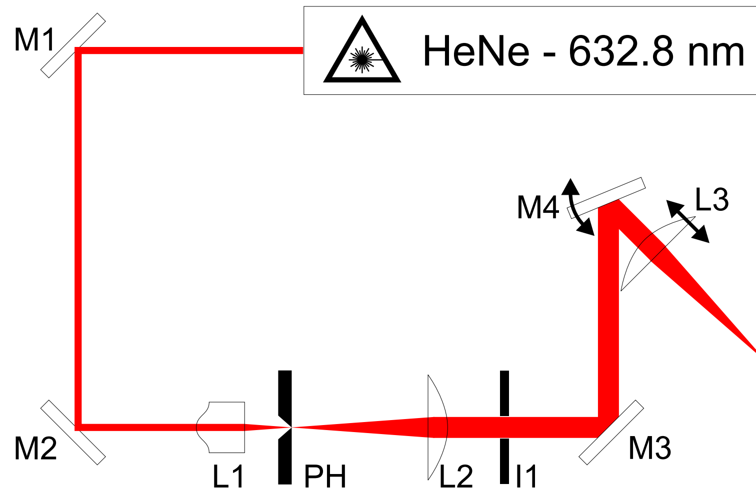

Fig. 3.14: Schematic diagram of the optical laser focusing setup.

angle $\theta_0 = (8.14 \pm 0.25) \cdot 10^{-4}$, which corresponds to a waist width of $w_0 = 0.247 \pm 0.08$ mm. (see appendix B for details of the Gaussian beam). Based on this measurement, it is plausible to assume that the laser has been designed to have a waist width of $w_0 = 0.25$ mm. The waist is assumed to be located at the front mirror of the laser cavity[1]

Mirrors M1-M2 The 25.4 mm diameter aluminum mirrors M1 and M2 are mounted in kinematic mounts with two adjuster screws used for fine adjustment of the direction and height of the laser beam.

Beam expander: L1, PH, L2, I1 Because of diffraction, a wider Gaussian beam can be focused to a smaller spot size than a narrower beam. Inside the chamber, a small spot is preferred, meaning that the laser beam should be as wide as possible before the focusing lens (L3).

This is achieved by the aspheric lens, L1 and the collimating lens, L2. This lens pair acts as a beam expander. L1 has a focal length of $f_1 = 7.5$ mm and focuses the beam to a waist radius of 1.6 µm. The position of L1 is finely adjusted so that this waist coincides with the 10 µm diameter pinhole (PH), which filters off most of the non-Gaussian spa-

[1]It may also be located in the centre of the laser, but since verification of the waist position requires a disassembly of the laser, it has not been done. Instead, the calculations of the beam propagation have been done for both waist positions, and the variation between the results are insignificant.

tial noise. The distance from the pinhole to the lens, L2, corresponds to its focal length, $f_2 = 50$ mm. The expanding beam is thereby collimated by L2 and will maintain its width (radius) of 6.26 µm with less than 1 % deviation over 27.5 m. The details of the Gaussian beam parameters are listed in table 3.1. The spatial filtering is not perfect and after collimation, the central Gaussian mode is surrounded by a number of fringes. These are removed by the adjustable iris, I1.

Besides from the iris, the limiting aperture between the collimating lens, L2, and the focusing lens, L3, is mirror M3, which is positioned in an angle of 45° to the beam. It will therefore cut off parts of the beam wider than $25.4\ \text{mm}/\sqrt{2} \approx 18$ mm. With a beam waist of 6.26 µm, more than 98 % of the power will pass unhindered through the mirror, and the Gaussian profile will not be significantly altered. This has been the criteria for selecting the focal lengths of L1 and L2.

Mirrors M3-M4 The purpose of M3 and M4 is to raise the beam vertically and reflect it down in a 45° angle onto the sample in the chamber. M3 and M4 are identical to M1 and M2 and are also mounted in kinematic mounts. They are furthermore mounted on a vibration damped pillar where they can be moved vertically. The adjuster screws for M4 are used to position and adjust the beam spot on the sample inside the chamber.

Focusing Lens L3 This plano-convex lens has a focal length $f_3 = 200$ mm and focuses the collimated Gaussian beam onto the sample. The lens is mounted on a micrometer precision translation stage with 30 mm movement parallel to the beam direction. With this translation stage and the two adjuster screws of M4, the focus point of the beam can be adjusted in all three dimensions with micrometer accuracy.

Lens	w_0/mm	z_w/mm	w'_0/mm	z'_w/mm
L1	0.25	-1130	0.0016	7.55
L2	0.0016	-50.0	6.26	0
L3	6.26	-490	0.00644	200

Table 3.1: Theoretical data for the Gaussian beam as it is transformed through the lenses L1–L3. w_0 and z_w are the waist radius and position before the lens, located at $z = 0$. w'_0 and z'_w are the values after transformation through the lens.

Practical limitations

The theoretical calculations on beam characteristics and spot size assume that the laser beam is perfectly Gaussian. Most of the output from the laser is in fact confined in the fundamental Gaussian mode, but some light also exists in higher order modes.

The purpose of the pinhole is to filter off this *spatial noise*, but doing so satisfactorily requires a very good match between the beam waist after the lens (L1) and the pinhole diameter. It also requires the pinhole to be almost perfectly circular. The primary requirement of the beam expander and spatial filter was to expand the beam from 0.25 mm to about 6 mm. To achieve this expansion, a strong focusing lens is needed, and with the strong focus follows a small beam waist. According to the theoretical calculations on the beam waist at the pinhole (see table 3.1), a pinhole diameter of 5 μm would be ideal, as about 99 % of the power in the fundamental Gaussian mode would be able to pass through it. A 5 μm pinhole was initially installed, but the resulting beam contained very strong noise components and was attenuated significantly. Replacing it with the 10 μm pinhole was a considerable improvement, but the beam is still not perfect, with the result that the focused beam spot in the chamber is slightly larger than expected from theory.

An estimation of the actual laser spot size was done by inserting a mirror in the position of the beam focus and directing the reflected, diverging beam onto the ceiling. The distance to the projected beam spot was measured as $d = (204 \pm 3)$ cm, and the radius of the spot was $w(d) = (6.0 \pm 0.5)$ cm. This corresponds to a divergence half-angle $\theta_0 = 0.029 \pm 0.003$, which again corresponds to a beam waist radius $w_0 = 6.8 \pm 0.7$ μm, under the assumption that the beam has a perfectly Gaussian profile. This measurement shows that the beam waist radius is close to the diffraction limited theoretical calculation of $w_0 = 6.44$ μm, as listed in table 3.1. It should be noted though, that the non-Gaussian beam components do not follow the transformation rules that govern the Gaussian beam, and the actual spot size may therefore be larger than predicted by this measurement.

Power attenuation

The laser power has been measured at different points through the system. This is important in order to optimize the position of the pinhole and is useful for estimating the power that can be reflected onto the photodetector and thus the sensitivity of the detector system. The measured powers are listed in table 3.2.

Position	Optical power/mW	Attenuation/dB
Laser output	7.8	0.0
After M2	6.2	1.0
After PH	4.0	2.9
Focus in chamber	1.9	6.1

Table 3.2: Measured optical power and total attenuation of the laser beam, at different points through the focusing part of the optical setup.

3.5.3 Detection and amplification

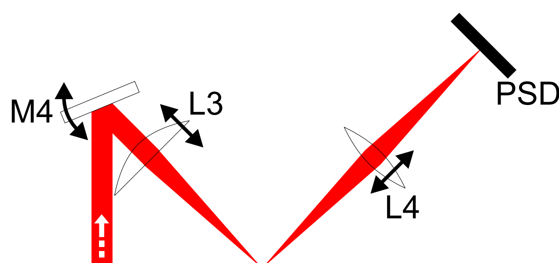

Fig. 3.15: Schematic diagram of the detection part of the optical setup.

The detection part of the optical setup is sketched in figure 3.15. The laser beam, after being focused onto the sample, is reflected up and out through the second angled flange in the chamber wall. Here it is collected by the lens L4, which focuses the light onto the PSD. The photo-current generated by the detector is then converted to a voltage, amplified and measured by e.g. a gain–phase analyzer.

Focusing the deflected beam

Under the assumption that the laser spot hitting the sample has a Gaussian profile, and that the sample has a perfectly plane, reflective surface, which is at least as large as the dimension of the laser spot, then the reflected beam can be treated analytically, and thereby giving an idea of the functionality and an estimation of the sensitivity of the detection.

Figure 3.16 illustrates the theoretical focusing of the beam from the sample through the collecting lens (L4) to the detector. The detector is seen to be displaced relative to the exact focus of L4. The reason for this is found by

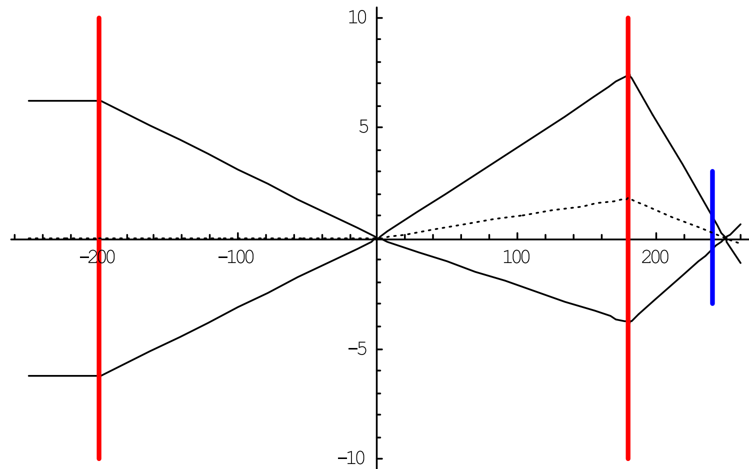

Fig. 3.16: This graph visualizes a calculation of the beam width and deflection along the optical path: through the focusing lens (red), sample, collecting lens (red) and detector (blue). The center of the beam is displayed as a dotted curve, while the full curves indicate the $1/e^2$ radii. Both axes are in units of millimetres; and for simplicity of calculation, the optical path has been straightened out at the point of reflection off the sample.

considering the function of a lens: All the rays of light that originate from a single point (object) in space before the lens will – by refraction through the lens – be deflected towards a single point after the lens (image). As the laser spot will practically be stationarily positioned on the cantilever, the focus of the laser spot will also be stationary. If the detector were placed exactly in this focus, there would be no change in signal when the beam is deflected by the cantilever. By adjusting the lens position, the focus can be displaced away from the detector plane to optimize the signal.

Position sensitive photo-detector (PSD)

The detector in the setup is a one-dimensional analogue PSD from SiTek, model 1L20_CP3, with an active area of 3×20 mm, and a responsivity of 0.63 mA/mW. It has two current outputs, and the generated photo-current from absorbed light is distributed between the outputs with almost linear dependence on the position of the light. Because of the large active area, the theoretically optimal position of the detector is at the position where the deflection of the centre of the beam is maximal (within the limit of the 20 mm height of the detector). The lens, L4, therefore serves no purpose in the ideal case. In praxis, the light reflected from a cantilever is much

more diffuse than a Gaussian beam, and the lens is necessary for collecting the diffuse reflections that would otherwise not reach the detector. A PSD position of a few centimetres after the lens has been observed to give optimal results, but the exact position is not critical.

A theoretical calculation of the signal-currents from the PSD when exposed to a Gaussian laser spot can be done by integrating the Gaussian intensity profile, $I(x, y)$, folded with the position-dependent current-responses, over the active area of the PSD. The position dependent current responses can be approximated as

$$R_1(y) = 0.63 \text{ mA/mW} \times (\frac{y}{h} + \frac{1}{2}) \tag{3.1a}$$

$$R_2(y) = 0.63 \text{ mA/mW} \times (\frac{1}{2} - \frac{y}{h}) \tag{3.1b}$$

where $h = 20$ mm is the height of the active PSD area as seen in figure 3.17. The signal-currents will then be:

$$i_j = \iint_A I(x, y) R_j(y) \mathrm{d}x \mathrm{d}y \tag{3.2}$$

where $j = 1, 2$ indicates the output, and A is the active area.

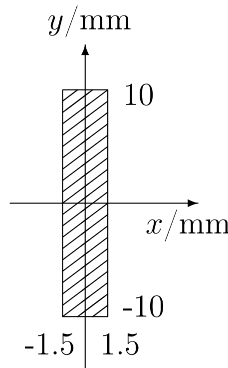

Fig. 3.17: Active area of PSD. h=20 mm, w=3 mm.

The beam position and intensity profile on the PSD can be calculated as a function of cantilever deflection-angle (as shown in figure 3.16). Inserting this into equation (3.2) will then provide information about the current-signal-amplitude as a function of cantilever deflection-amplitude for a vibrating cantilever:

Setting the theoretical PSD position to immediately after the lens and assuming that 1 mW of laser power is reflected onto the PSD, the signal amplitude calculates to

$$i_1 - i_2 = 9.15\ \mu\text{A/mrad} \tag{3.3}$$

The noise current of the PSD is specified to 0.5 pA/$\sqrt{\text{Hz}}$ for each output channel, which gives a RMS noise for the current-difference of 0.71 pA/$\sqrt{\text{Hz}}$. The theoretical detection limit (signal–to–noise ratio of 1) is therefore

$$\Delta\theta_{min} = 78\ \text{prad mW}/\sqrt{\text{Hz}} \tag{3.4}$$

This number should be multiplied by the detection bandwidth and divided by the actual reflected laser power, which is typically much less than 1 mW, depending on the material and size of the cantilever sample that is being measured on. With a typical bandwidth of 100 Hz and a reflected laser power of 0.1 mW, the minimum detectable deflection amplitude is (by this theoretical calculation) $\Delta\theta_{min} = 5.5$ nrad.

Quadrant photo-diode

In AFM systems a quadrant photo-diode is used for detection of the reflected laser beam, and this approach was also considered for the vacuum chamber. A quadrant or dual photo-diode is ideal when the reflected light has an intensity profile that is approximately Gaussian. In this case the diode position should be adjusted so the junction between the different diode-parts is located at the steepest intensity slope of the Gaussian profile. This ensures maximum sensitivity towards deflections of the beam.

Some of the major differences between such a detection method and the one implemented here will be discussed in the following. The advantages of the PSD can be summarized as:

An analogue response, which enables measurements on non-Gaussian reflected light. The active area is not sensitive to the intensity profile of the absorbed light. Since most samples in the chamber are smaller than the focused laser spot, the reflected light will be a diffracted pattern of light rather than a *nice* Gaussian beam.

A large active area, which makes the PSD insensitive to the exact position of the reflected light. In the characterization of the gold coated cantilevers (described in chapter 4), the temperature changes created a stress-induced bending of the cantilevers due to their bimorph structure. This resulted in a large offset (several millimetres) of the reflected

beam, which was not a problem for the PSD, but would have been for a quadrant diode.

For a system where the reflected beam is Gaussian, the quadrant photo-diode detector on the other hand holds some advantages:

Quasi-digital response, in the sense that the laser spot is cut over a sharp edge, giving a much higher sensitivity towards small deflections of the beam.

Faster response time due to the much smaller active area of the quadrant diode. The rise time of the PSD is 500 ns which sets the upper limit of about 2 MHz to the detectable frequencies. In comparison, a $5{\times}5\ \mathrm{mm}^2$ commercially available quadrant diode will have response times down to 5 ns enabling detection of signals up to 200 MHz.

Lateral sensitivity. The quadrant diode is structured as a 2×2 diode array, which enables it to detect lateral deflection of the laser spot. This can be used for characterization of twisting modes of cantilevers, whereas the PSD is mainly sensitive to flexural bending modes.

Electrical amplification

Two signal conditioning circuits were constructed in order to analyze the signal from the PSD: a pre-amplifier circuit for converting the output currents from the PSD to voltages, and a difference-amplifier in which the two voltages are subtracted and further amplified.

The pre-amplifier circuit is shown in appendix section E.1. The pre-amplifier is based on the a low–distortion, low–noise operational amplifier, type Burr-Brown OPA2604. The amplification in the circuit is 100 V/mA, and the noise is specified to be $10\ \mathrm{nV}/\sqrt{\mathrm{Hz}}$. According to equation (3.3), this gives a signal amplitude of

$$U_1 - U_2 = 915\ \mathrm{mV/mrad} \tag{3.5}$$

per mW of reflected laser power and a RMS voltage noise of $51\ \mathrm{nV}/\sqrt{\mathrm{Hz}}$ per channel, which is dominated by the contribution from the PSD current noise.

The difference-amplifier is shown in appendix section E.2. This is based on a high-speed, low-noise operational amplifer, type Analog Devices AD829. The output of the difference-amplifier is $U_{out} = 100(U_1 - U_2)$. The input voltage noise of the AD829 is $1.7\ \mathrm{nV}/\sqrt{\mathrm{Hz}}$, which is negligible compared to the output noise of the pre-amplifier. With the $100\times$ difference-amplification, the noise figures on the two input channels result in an RMS output noise

of 7.2 $\mu V/\sqrt{Hz}$. The signal amplitude from an oscillating cantilever is 100 times that of the pre-amplifier, equation (3.5), and since the bottleneck noise source is the PSD, the theoretical detection limit after pre- and difference-amplification is still given by equation (3.4).

3.6 Improvements

From the experimental work done in the chamber, a number of possible improvements have been revealed. Some of these could be implemented with the current setup as it is (section 3.6.1), while others would be suitable for a "*second generation vacuum chamber and detection system*" (section 3.6.2).

3.6.1 Improvements of current setup

Electrical noise shielding

The noise originating from the temperature controller may be minimized by connecting a 10 nF capacitor between the "+" and "−" terminals of the RTD connection on the controller, and another capacitor between the "−" terminal and the chamber wall to dampen the high frequency noise.

Ideally, the cables carrying high precision signals should be individually shielded and connected to coaxial connectors in a different LEMO plug. Such connectors take up considerable space in a plug, implying that just two coaxial connectors would come at the expense of at least half of the current numbers of commonly shielded conductors in the plug.

Mechanical stability

For the optical detection, the greatest noise source is the physical vibrations of the chamber. Most of these originate from the diaphragm pump and travel through the hose connecting the chamber and the pump.

These mechanical vibrations may be minimized by two initiatives. Firstly, the chamber can be fitted with mounting brackets at the outer bottom edge, so that it may be fastened rigidly to the optical table. Secondly, the vibrations of the pump hose may be dampened by leading it through a box of sand or by fastening it to the optical table. The first approach alone would probably be effective and sufficient, but also require more effort than the second – and probably less effective – approach.

Temperature and pressure control

As mentioned in section 3.3.4, the temperature control reacts relatively slowly – especially in vacuum – and for this reason, the temperature is not controlled very accurately, since the controller is not capable of fast compensation for temperature fluctuations.

A sample holder with an integrated Peltier-element in direct contact with the sample would enable a fast and accurate temperature control, although integration with a piezo-electric element for actuation might be a challenge. If the Peltier-element is not in direct contact with the sample, there might be a temperature variation between sensor and sample, and the improved speed and accuracy may thence come at the cost of a reduced precision.

The pressure sensor provides very accurate readings of the actual pressure, but the valve system does not allow very accurate control. The ideal method for controlling the pressure would be to keep the pump connected to the chamber and control the gas flow into the chamber using a mass flow controller at the gas inlet. This would maintain a stable equilibrium pressure.

Video inspection system

To improve on the relatively large distortion of the video inspection system described in section 3.4.2, a slightly more advanced imaging system composed of two lenses could be implemented. In the following, some calculations on two such systems are presented. Both systems are composed of two commercially available, identical lenses. In the first system two plano-convex lenses are placed with the convex surfaces facing each other as shown in figure 3.18 b). This approach decreases the total spherical aberration to about one third of the value for the single bi-convex system. The chromatic aberrations are not improved by this approach, since that requires the use of different glass types with different dispersion coefficients [45]. As the chromatic aberrations are dominant, a more efficient solution is to use two achromatic doublets as shown in figure 3.18 c). These are lenses consisting of two types of glass that are cemented together. The curvature of the three spherical surfaces in the doublet are designed to minimize both spherical aberration and chromatic aberration.

To get an intuitive idea of the improvements in image quality and resolution that can be obtained by the three different imaging systems mentioned, the spot diagrams for on-axis and 3 mm off-axis object points have been calculated using optical characterization software WinLens from LINOS Photonics. The diagrams are shown in figure 3.19.

The best optical imaging system for minimized on- as well as off-axis

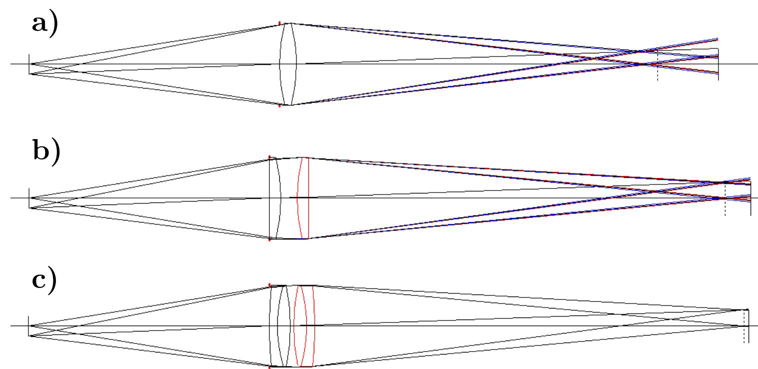

Fig. 3.18: Schematics of three different imaging systems for video-monitoring of the sample: **a)** Single bi-convex lens, **b)** Double plano-convex and **c)** Double achromatic doublet.

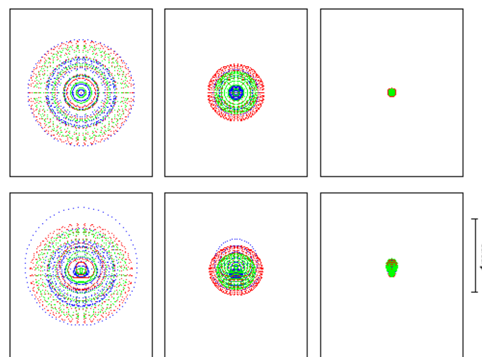

Fig. 3.19: Spot diagrams for on-axis object points (top) and 3 mm off-axis object points (bottom) of the bi-convex lens (left), the double plano-convex system (middle) and the double achromatic doublet (right).

aberrations would probably be a cooke triplet, which is the simplest imaging system with sufficient design parameters to minimize all first and third order aberrations [46]. The drawback is, that it would take up considerably more space inside the chamber than the two-lens alternatives, and it would also require custom made lenses rather than standard commercially available ones.

It is important to note that the spot diagrams represent the image just above the top flange, as it would appear on a photographic film or CCD-array located there. In reality, the lens in the chamber and the camera objective constitute a single optical system, and the spot-sizes of the intermediate

image cannot be used to calculate the actual resolution of the entire imaging system. They only serve the purpose of indicating the relative quality of the different proposed lens systems.

3.6.2 Second generation setup

Elaborate details on the possible improvements of a second generation setup do not exist, as such a setup may not become a reality. An outline of the considered improvements is given here.

- Different distribution of space in the chamber. Handing of samples in the current setup is slightly awkward, as the top opening is narrow compared to the depth of the chamber. Currently, removal of the inner electrical plug is close to impossible without dismantling the sample holder – also due to the narrow lateral dimensions of the chamber body.

- Automatic rotation and translation stage for sample in chamber. In the current setup, the sample is mounted horizontally and cannot be moved easily. A heat-induced bending of a cantilever sample may result in a deflection angle of the laser beam that cannot be detected. The dimensions of the chamber are too small to implement motorized stages.

- Improved electrical shielding, by implementing separate electrical connections for "noisy" and "sensitive" cables. Lose cables inside the chamber should also be avoided, to reduce outgassing from the cables and to avoid contamination of the cables when chemicals are introduced into the chamber.

- Improved optical detection system – preferably a laser focusing lens (microscope objective) inside the chamber to obtain a smaller beam spot, similar to the implementation in atomic force microscopes. In the design of this, the sample should be positioned close to an inspection window, to allow visual inspection by a regular optical microscope. This would also allow for a laser doppler vibrometer to be integrated into the microscope optics, such as the Polytec MSV-400 [47], capable of mapping the out–of–plane motion with picometer displacement resolution.

Chapter 4

Resonant properties of monolithic and gold-coated SiO_2 cantilevers

4.1 Background

The common way of functionalizing cantilever sensors is by applying an adsorptive coating to the cantilever top surface. A gold coating is frequently utilized for both static and resonant detection functionalization. The use of gold is due to the large selection of materials that can be adsorbed via thiol chemistry, as described in chapter 1.

In the case where the sensor is based on static deflection, this presents the problem of a strong temperature dependence due to the bimorph effect [48, 49]. This effect, however, may be compensated for by simultaneous temperature monitoring or a non-functionalized reference cantilever.

In the case of resonant mode cantilever sensors, the bimorph stress and bending causes a shift in the resonance frequency [26, 50, 51]. This may be a problem in some applications, but may again be compensated for by reference cantilevers or temperature monitoring. However, a gold film presents an entirely different problem for resonant cantilevers, namely that of damping due to internal friction in the gold [52], resulting in significantly lower Q-factors of the cantilever modes.

The sensitivity of the resonant cantilever when used as a mass sensor depends on the spectral resolution, which is directly related to the Q-factor of the resonant mode, defined in [52] as

$$Q = 2\pi \frac{\text{Stored vibrational energy}}{\text{Energy lost per cycle of vibration}} = \frac{f_0}{\Delta f} \tag{4.1}$$

where f_0 is the resonance frequency of the mode and Δf is the FWHM of the resonance peak in the frequency domain.

The total energy loss per cycle may be expressed as a sum of different loss sources with corresponding Q-factors: internal material loss (Q_i), loss to the chip substrate through the cantilever support (Q_s), and viscous (and acoustic) loss [53] to the surrounding medium (Q_a). The total Q-factor is then given by

$$\frac{1}{Q} = \frac{1}{Q_i} + \frac{1}{Q_s} + \frac{1}{Q_a} \tag{4.2}$$

where the viscous damping term is usually dominant at atmospheric pressure.

In the characterizations of silicon dioxide cantilevers, it was found that higher order resonant modes exhibit considerably higher Q-factors than the fundamental modes, implying that the higher order modes potentially will yield higher sensitivities in resonant cantilever sensor applications.

As most cantilever sensor applications require operation at atmospheric pressure, great effort has been put into describing the effect of pressure on the resonant properties of cantilevers – both experimentally [41, 27, 54, 55] and theoretically [56, 57, 58, 59]. The different approaches have yielded good results for different aspects of the research area, but as the constellation of temperature-, pressure- and gold coating effects is highly complex, many aspects are still to be discovered – especially that of internal cantilever losses, which the theoretical models do not account for with sufficient detail to be directly applicable.

The material properties such as elasticity and internal viscosity of silicon dioxide as well as gold vary with temperature. As these are central properties for the resonance frequency and Q-factor of the cantilevers, the effect of temperature should not be neglected.

These issues have therefore been addressed here, and experimental results are presented from the characterization of a series of monolithic silicon dioxide cantilevers with high intrinsic Q-factors (in the order of 10^3–10^4), onto which gold coatings of varying thicknesses are applied. The resonant properties of the cantilevers are measured at different pressures and different temperatures.

4.2 Experiment

4.2.1 Initial considerations

The experiment described here was of an *initial* nature, where even the qualitative outcome was not known a priori. The purpose was to discover areas of interest for further investigations, where focus could be directed to specific issues. It was therefore necessary to include as many parameters into

the experiment as possible in order to draw the correct conclusions on the causality of the experimental observations. Some of the considerations prior to designing the experiment are discussed here.

There are several factors that determine and influence the Q-factor of an oscillating cantilever. At atmospheric pressure, the major limiting factor is the viscous damping due to the surrounding medium (usually air) [56]. The viscous damping itself depends on the geometry of the cantilever i.e. its general shape, and for rectangular cantilevers its width and length, and to a certain degree its height. It is plausible to assume that viscous damping is also dependent on the specific flexural mode of the oscillating cantilever, as the air flow pattern will be different from e.g. the fundamental mode, where the air must flow around the cantilever edges, and some higher order mode with several nodal points, where the air may just relocate across a nodal point.

In vacuum, the damping mechanisms determining the Q-factor are the internal losses and support losses. The internal friction in gold is much higher than in silicon dioxide [60], which has been used as substrate material for the cantilevers. Furthermore, the mass density of gold is almost an order of magnitude greater than that of silicon dioxide. It is therefore reasonable to presume that the gold coating thickness will have a great influence on the Q-factor in vacuum.

Bimorph effects, such as bending due to the difference in the thermal expansion coefficients of the substrate material and the metal film, was also presumed to affect both the Q-factor and the resonance frequencies.

4.2.2 Design of experiments

Ideally, all the above mentioned effects should be investigated through careful design of experiments. This would, however, require a set of measurements with a parameter space too extensive to be carried out within a reasonable period of time. The parameters that would have to be varied include cantilever height, width and length, metal film coating thickness, temperature, pressure and vibrational mode number.

To reduce the number of experiments, an experiment design program such as MODDE could be used, if it wasn't because some parameters are not easily varied. These include *cantilever shape and dimensions*, as specific component design and fabrication for these experiments was not an option; *metal film thickness* (can only be increased by depositing additional layers) and *temperature* due to the long temperature response time of the vacuum chamber.

Another major hindrance to using MODDE is that the Q-factor measurements have a relatively low accuracy and reproducibility, as discussed in section 4.3. To obtain qualitatively correct conclusions through MODDE, a redundancy of measurements would therefore be required, implying that the benefits of MODDE are rather outweighed by the drawbacks.

For that reason, the experimental procedure was designed *by hand*, and it was decided to neglect the cantilever width and height as variable parameters, by using a chip containing six cantilevers of varying lengths but identical widths and thickness. The chip could be coated with different thicknesses of gold layers through subsequent depositions, and for each layer thickness, all measurable modes of the cantilevers could be characterized at two temperatures, 30 °C and 45 °C, in vacuum (approximately 50 Pa) as well as atmospheric pressure (100 kPa). The parameter space covered by these measurements is summarized in table 4.1.

Upon completion of this series of measurements it was evident that two temperatures and two pressures did not give a sufficiently detailed picture of the thermal and pressure-dependent effects, and one of the cantilevers was therefore characterized for a range of pressures and a range of temperatures. This was also done for a new, uncoated cantilever on a chip from the same wafer. This cantilever held the same properties as the gold coated ones, but with a slightly different length.

4.2.3 Cantilever devices

The chip containing six monolithic silicon dioxide cantilevers with different lengths[1] is shown in figure 4.1. The silicon dioxide is 0.85 µm thick and was grown thermally on a Si (100) wafer. Using UV-lithography and reactive ion etch, the oxide was patterned to form the cantilevers [61].

The cantilevers are all 10 µm wide with lengths of 89, 113, 137, 161, 185 and 209 µm. The lateral dimensions are measured with an accuracy of about 1 µm using an optical microscope. The effective length of the cantilevers may differ slightly from the measured value because of cantilever–substrate boundary effects in the clamped end (see Rinaldi et al.[62] for a detailed study on boundary effects). The precision error from the clamping effect on the effective length is expected to be less than 2 µm, evaluated by inspection of the SEM image shown in figure 4.2.

In order to observe the effect of different coating thicknesses, the SiO_2 cantilevers were characterized without any metal coating, and with three

[1]The cantilever chips used in these experiments are designed and fabricated at MIC by Kristian Mølhave.

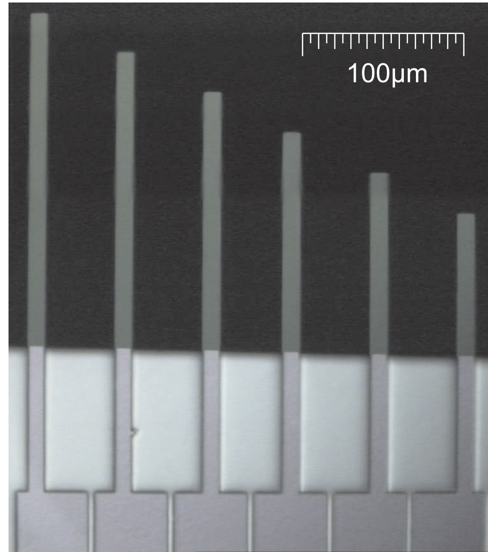

Fig. 4.1: Optical microscope image of the silicon dioxide cantilever chip before metal deposition.

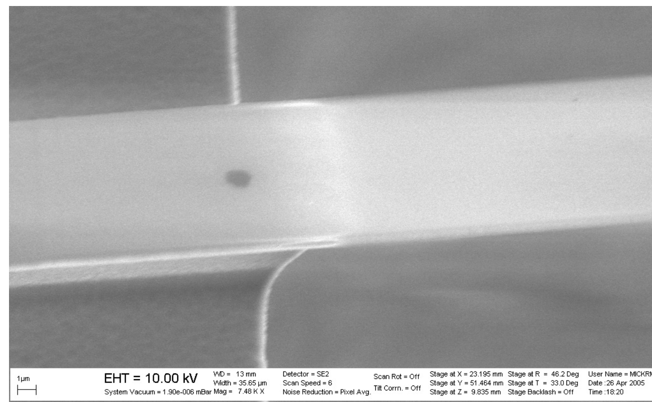

Fig. 4.2: SEM image showing the clamping end of one of the uncoated cantilevers.

different thicknesses of gold, deposited on the top surface. In the first deposition a 10 nm titanium layer was formed to ensure good adhesion between the SiO_2 and the gold, and a subsequent layer of 100 nm Au was deposited. In the second deposition another 100 nm Au, and in the third deposition an additional 200 nm Au was formed. The cantilever characterizations were therefore done for 0 nm, 100 nm, 200 nm and 400 nm Au coating layers.

The depositions were done in an Alcatel E-beam evaporator with a chamber pressure of 0.1 mPa and a deposition rate of 10 Å/s for Ti and 5 Å/s for Au. Deposition of the Ti-layer and first Au-layer was done successively to avoid oxidation of the titanium.

Parameter	Values used for measurements
Cantilever length	$89, 113, 137, 161, 185, 209$ µm
Au thickness	$0, 100, 200, 400$ nm, Adhesion: 10 nm Ti
Temperature	30 °C, 45 °C
Pressure	50 Pa, 100 kPa
Mode	1 - 7, limited by: $f_i \lessapprox 2$ MHz

Table 4.1: Overview of the parameter space covered by measurements of resonance frequency and Q-factor.

For the detailed temperature- and pressure-related measurements, the 185 µm long gold coated cantilever, and an uncoated cantilever, 195 µm long, on a different chip from the same wafer were characterized.

The material data used for modelling the cantilever properties analytically and by finite–element simulation is listed in table 4.2.

Layer	$height$/nm	$\rho/(\mathrm{g/cm^3})$	E/GPa
SiO_2	850	2.15	70
Ti	10	4.5	116
Au	100, 200, 400	19.3	78

Table 4.2: Summary of layer structure and material data for the cantilevers used. Values are obtained from [63, 64].

4.2.4 Chip mounting

The chip containing the six cantilevers is shown in figure 4.3. Its dimension is approximately 1.6 mm × 4 mm and it is glued onto a printed circuit board (PCB) for mounting and actuation in the PZT-adapter (see figure 3.10, page 23). The chip and PCB is fastened to the piezo-ceramic actuator using double sided tape to ensure a better transfer of the actuator movement to the chip. For high frequencies, the tape will assumably absorb an increasing amount of vibration energy due to its elastic properties, resulting in a smaller actuation of the chip. However, experiments without the tape showed significantly lower signals (more than 30 dB lower signal–to–noise–ratio) and

no more than 3 detectable modes for the long cantilever, meaning that the actuation is improved considerably when using the tape.

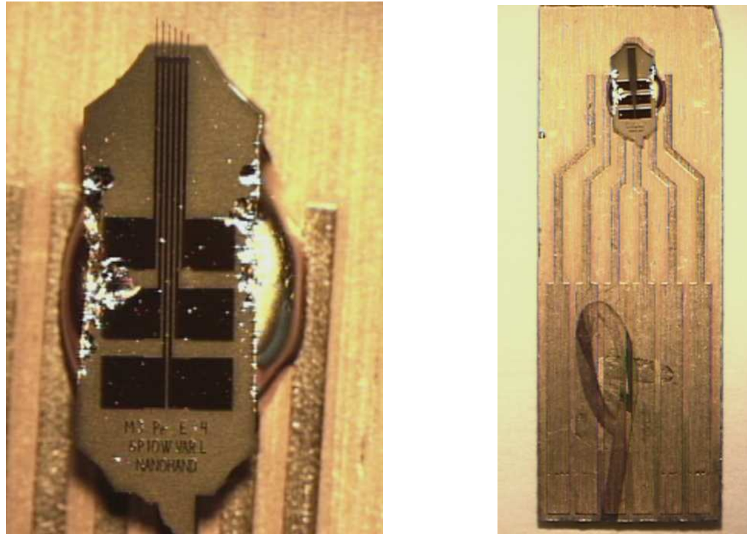

Fig. 4.3: Closeup image of the gold coated cantilever chip (left). The chip mounted on the PCB (right); note that the conducting circuits of the PCB serve no functional purpose for this particular chip.

4.2.5 Actuation and detection

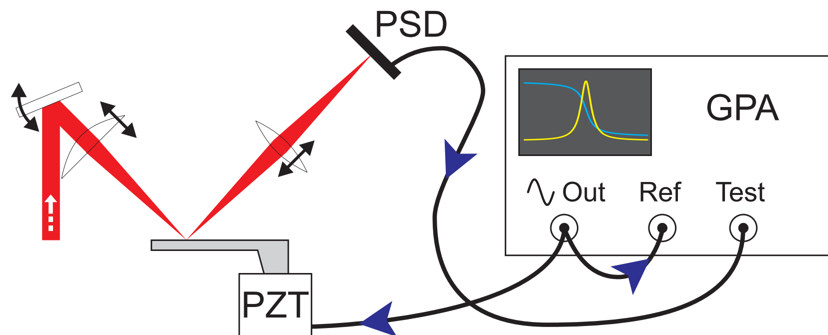

Fig. 4.4: Schematic diagram of the actuation and detection setup.

The output signal of a gain-phase analyzer (GPA) (Hewlett Packard, model 4194A) is used for driving the piezo-ceramic actuator (PZT), and

is also directed to the GPA reference channel input, as illustrated in figure 4.4. The amplified difference-signal from the position-sensitive photodetector (PSD) is connected to the GPA test channel input. The laser is focused with minimum spot size (beam waist) on the cantilever and the spot is positioned so as to get maximum deflection amplitude of the reflected laser beam onto the PSD. The GPA is then used to perform a frequency sweep, measuring the amplitude and phase of the input signal relative to the output signal at a number of linearly spaced discrete frequencies over a specified frequency range. The measured values of amplitude and phase are transferred via a GPIB interface to a LabVIEW program on the computer and stored in a file for further analysis (see appendix F).

When doing a frequency sweep around the resonance frequency of an isolated flexural mode of a cantilever, the measured amplitude vs. frequency may be fitted with a Lorentz curve[2],

$$A(f) = A_0 + \frac{\alpha}{(f - f_0)^2 + \beta} \tag{4.3}$$

In this fit, the resonance frequency of the cantilever mode is taken as the Lorentz peak's center with a full–width–half–maximum (FWHM) which is given by $2\sqrt{\beta}$ and a Q-factor (defined as the resonance frequency divided by the FWHM) of

$$Q = \frac{f_0}{2\sqrt{\beta}} \tag{4.4}$$

The Lorentz function (equation (4.3)) is a built-in fitting function in the data analysis program Igor Pro, and has been used for fitting the measured data, although the expression for the frequency response of a simple harmonic oscillator (SHO) [66] describes the behaviour of the cantilever resonance peaks more accurately:

$$A(f) = A_0 + \frac{4\alpha f_0^2}{(f^2 - f_0^2)^2 + 4f^2\beta} \tag{4.5}$$

Using the ordinary Lorentz-function instead of this – more correct – expression will only result in serious errors for very low Q-factors ($Q < 10$). For $Q > 10$, the resonance frequency (determined as the position of the Lorentz

[2]The fit is done using the data analysis software Igor Pro by WaveMetrics. Igor uses the Levenberg-Marquardt algorithm to search for the coefficient values that minimize chi-square, defined as $\sum_i \left(\frac{y-y_i}{\sigma_i}\right)^2$, where y is a fitted value for a given point, y_i is the measured data value for the point and σ_i is an estimate of the standard deviation for y_i. This is a form of non-linear, least-squares fitting [65].

peak) will deviate from the SHO expression with less than 0.3 %, and this deviation scales with $1/Q^2$. Figure 4.5 shows a comparison between the two expressions for different values of Q. As all the measured Q-factors are in the order of 10^1–10^4, the values obtained by fitting the experimental data to equation (4.3) are considered to be sufficiently accurate for a re-evaluation to be unnecessary.

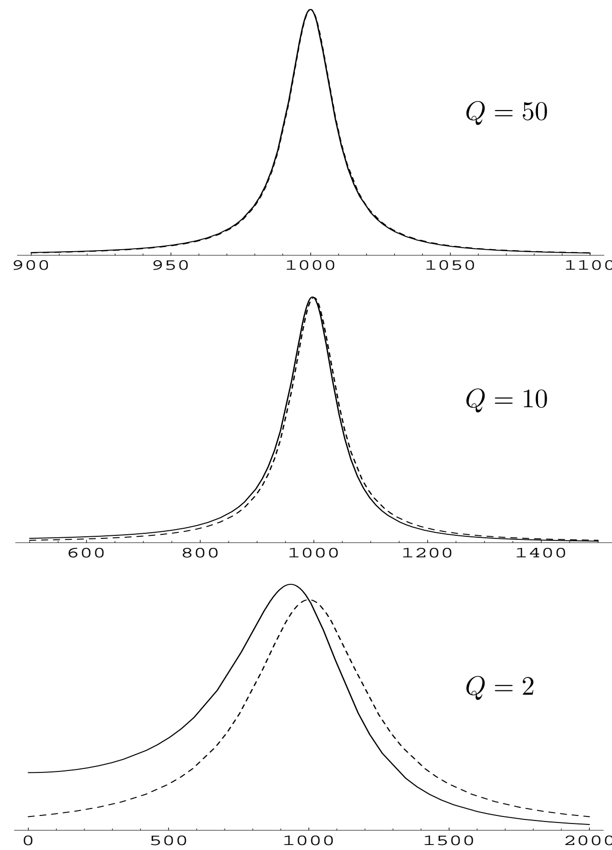

Fig. 4.5: Illustration of the deviation between the ordinary Lorentz function (equation (4.3) – dashed curves), and the expression for the frequency response of a simple harmonic oscillator (equation (4.5) – solid curves), for Q-factors 2, 10 and 50.

4.2.6 Measurement procedure

In order to ensure maximum reproducibility and reliability in the frequency scans and Q-factor measurements, a general measurement procedure regarding equipment settings and adjustment steps has been established as follows:

- All pieces of optical equipment in the setup have been tightly secured prior to all the measurements and have been left untouched, with the adjustment screws of the upper mirror and the primary focusing lens as the only exceptions (see figure 3.14, page 28).

- All equipment, including the He-Ne laser, the temperature controller and the GPA, is turned on well in advance of the measurements, to avoid drift and instability during warm-up.

- The settings of the GPA have been optimized and are kept the same for all similar measurements. These settings include

  - Input and output impedance and attenuation.
  - Number of sampling points. This number influences the frequency sweep speed and thus the cantilever oscillation amplitude because of its finite response time to a change in actuation frequency.
  - Frequency span (sweep range). Should be as small as possible without cutting off a significant part of the tails of the resonance peak. The span was chosen as 20 kHz for measurements at 100 kPa and 5 kHz for measurements in vacuum.
  - Integration time. This can be set to *short*, *medium* and *long*, and has been set to *medium*, as a tradeoff between speed and SNR, for nearly[3] all measurements.

- After inserting the chip into the vacuum chamber and sealing it, the laser beam is focused onto the chip surface close to the cantilevers, and the minimum spot size is obtained by adjusting the position of the focusing lens along the optical path while inspecting the beam spot on the video monitor.

- The optimal laser spot position, yielding the highest Q-factor and/or the best SNR, varies slightly between the different modes of a cantilever, and any attempt to optimize the Q-factor for each mode would result in a very low measurement reproducibility. Since reproducibility is a more important issue here than high Q-factor readings, all detectable modes of a cantilever are measured successively with the same laser spot position. This position is found for cantilevers in vacuum by maximizing the detected oscillation amplitude at the peak of the

[3] A few exceptions were done; when the SNR was so low that a *long* integration time had to be used; and in a few cases, when signal fluctuations occurred so frequently that a *short* integration time (and thus a fast sweep) was necessary to get a *clean* curve.

first mode. For cantilevers at 100 kPa the peak of the first mode is often very poorly defined, and therefore, the laser spot position is set to maximize the peak of the second flexural mode.

One setting of the GPA that could not be kept constant for all measurements was the oscillation amplitude, i.e. the amplitude of the AC voltage driving the PZT actuator. Too low an amplitude resulted in a poor SNR and too high an amplitude resulted in distortion and frequency-displacement of the measured Lorentz-peaks. As described in the following, a common amplitude for all modes could not be found. The oscillation amplitude was therefore optimized for each mode as the highest amplitude without any measurable distortion of the Lorentz-peak. One set of amplitudes was defined for the cantilever modes in vacuum measurements, and another set for atmospheric pressure. These sets of amplitudes were then used to the extend possible for the same modes in subsequent measurements e.g. after the metal depositions.

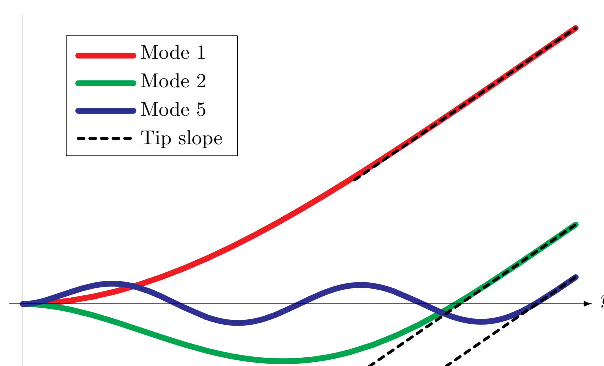

Fig. 4.6: Modal shapes of flexural modes 1, 2 and 5. The amplitude of each mode is scaled to attain identical deflection angles at the tip. This requires a much larger tip-deflection for mode 1 than for the higher order modes.

For the 1st order modes, a high amplitude was required to get a good SNR, while for the middle modes of each cantilever, a lower amplitude was necessary to avoid signal distortion. For the highest order modes, a high amplitude was again required in order to get a decent SNR – most likely because of a smaller response of the PZT at high frequencies. In vacuum, the oscillation amplitude was in general much lower than the one required for atmospheric pressure. Typical values of the amplitudes are −10 dBV for fundamental and high order modes in vacuum, −45 dBV for middle modes

in vacuum, 0 dBV for fundamental and high order modes at atmospheric pressure and −10 dBV for middle modes at atmospheric pressure.

The low oscillation amplitude for higher order modes and high amplitude for low order modes may be caused by the fact that the optical detection system measures deflection angle rather than deflection distance. To obtain a measurable deflection angle on the cantilever surface, the tip-deflection must be much larger for the fundamental mode than for higher order modes, because of the distance between a point of maximum deflection and the closest nodal point. This is illustrated in figure 4.6.

4.3 Results

4.3.1 Resonant modes

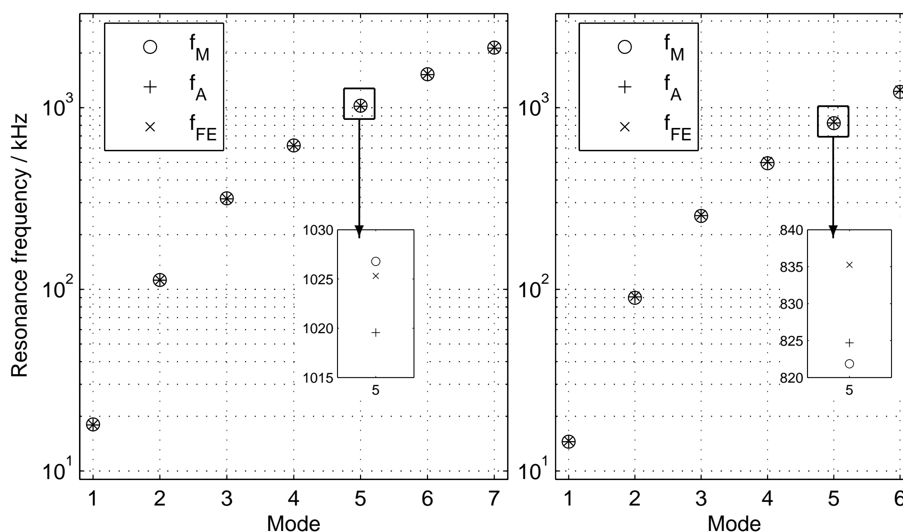

Fig. 4.7: Measured and calculated resonance frequencies of the flexural modes of the cantilever with $\ell = 209$ µm, uncoated (left) and coated with 400 nm gold (right). The subscripts M, A and FE refer to measured, analytical and finite-element values respectively. The insets magnify the deviation between the different methods.

The resonance frequencies of monolithic as well as multi-layer (coated) cantilevers can be calculated by equation (2.15). A comparison between the measured resonance frequencies in vacuum and the values obtained from this theoretical expression has been done to evaluate the quality of the theoretical deduction as well as the dimensions and material properties of the fabricated

cantilevers. As a cross-validation of the device properties and the theoretical model, some of the resonance frequencies have also been computed in a finite-element simulation of the cantilevers' eigenmodes, using the modelling software CoventorWare.

The results for the 209 µm long cantilever without gold coating and with 400 nm gold is shown in table 4.3 and figure 4.7.

The deviation between the calculated results and the measured can be explained by the inaccuracy in determination of the layer thicknesses and material properties. It appears that the analytical model in general results in lower values than the finite element simulation. This could be due to the small deflection approximation, which causes the analytical model to neglect the fact that the effective length of the cantilever is reduced because of the flexural bending.

There is very good agreement between the experimental results, the finite-element model and the analytical model, which confirms the validity of the theory as well as the quality of the fabricated cantilevers – in terms of the material properties and the geometry being close to the expected or measured values.

Cantilever	n	$f_{n\mathrm{M}}$/ kHz	$f_{n\mathrm{A}}$/ kHz	$\frac{f_{n\mathrm{A}}-f_{n\mathrm{M}}}{f_{n\mathrm{M}}}$	$f_{n\mathrm{FE}}$/ kHz	$\frac{f_{n\mathrm{FE}}-f_{n\mathrm{M}}}{f_{n\mathrm{M}}}$
ℓ=209 µm	1	18.079	17.936	-0.79 %	17.963	-0.64 %
No coating	2	112.712	112.406	-0.27 %	112.621	-0.08 %
	3	316.922	314.739	-0.69 %	315.596	-0.42 %
	4	619.447	616.764	-0.43 %	619.216	-0.04 %
	5	1026.781	1019.555	-0.70 %	1025.310	-0.14 %
	6	1529.501	1523.038	-0.42 %	1534.801	0.35 %
	7	2142.038	2127.219	-0.69 %	2148.919	0.32 %
ℓ=209 µm	1	14.502	14.508	0.04 %	14.652	1.03 %
Au-coating:	2	89.941	90.921	1.09 %	91.831	2.10 %
400 nm	3	253.449	254.582	0.45 %	257.262	1.50 %
	4	494.620	498.878	0.86 %	504.600	2.02 %
	5	821.842	824.681	0.35 %	835.254	1.63 %
	6	1223.309	1231.931	0.70 %	1249.838	2.17 %

Table 4.3: Resonance frequencies of the measurable flexural modes (n) of the 209 µm long cantilever; obtained by measurements ($f_{n\mathrm{M}}$), analytical expression ($f_{n\mathrm{A}}$) and finite-element model ($f_{n\mathrm{FE}}$). Also shown is the deviation of the calculated results from the measured.

For the other cantilevers there is an equally good correspondence between simulated, theoretical and experimentally obtained resonance frequency val-

ues. The deviation between theoretical resonance frequencies and actual resonance frequencies measured in vacuum is 2.4 %. This is the RMS value when averaging over all modes of the six cantilevers on the chip.

4.3.2 Q-factor dependence on resonance frequency

In the characterization of each cantilever, a clear tendency towards higher Q-factors for the higher order modes was observed. The Q-factors of the shorter cantilevers were also higher than those of the longer cantilevers. This is illustrated in figure 4.8, which shows the Q-factors in vacuum of all the measured modes of the uncoated cantilevers as a function of resonance frequency. The observed Q-factor variation can be described by a frequency dependence, where a higher resonance frequency of a mode implies a higher Q-factor of that mode.

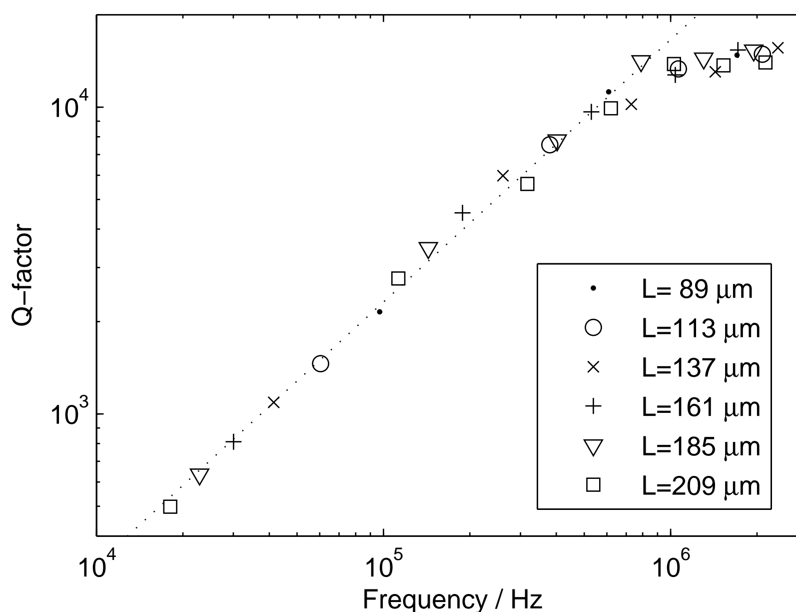

Fig. 4.8: Q-factors in vacuum at 30°C of all measured flexural modes for each of the six uncoated cantilevers, graphed as a function of the resonance frequencies of the modes. The dotted line ($Q \approx 0.123(f/\mathrm{Hz})^{0.855}$) is a power-law fit to the points below 1 MHz.

The Q-factors for resonance frequencies below 1 MHz appear to be linearly dependent on frequency, but are best fitted by a power-law as $Q \approx 0.123(f/\mathrm{Hz})^{0.855}$ (dotted line). The apparent falloff for frequencies above

1 MHz could be caused by the frequency response of the measurement equipment, as the cut-off frequency of the photo-detector is close to 2 MHz. The most interesting thing to note though, is that the Q-factors do not explicitly exhibit a dependence on cantilever length or mode, but only on the resonance frequency.

The almost linear dependence between the Q-factors and the resonance frequencies is supported by the theory presented by Blom et al. in [56]. Blom derives an expression for the Q-factor caused by dissipative damping, as well as the expression for the Q-factor caused by air damping in the molecular Knudsen region, and both show a distinct proportionality to the frequency of vibration for cantilevers with identical cross-sections. The measured deviation from this linearity, as described in the power-law fit, may be caused by different loss mechanisms that are not linearly frequency dependent, such as support-loss.

The expression for dissipative damping in [56] is very general and does not specify how to actually calculate exact values of Q. Several other theoretical models for Q-factors and cantilever damping have therefore been taken into consideration to evaluate the measured values.

The expression given by Blom for the Q-factor of a rectangular cantilever, due to damping caused by collisions with gas molecules is more specific:

$$Q = \frac{\kappa_n^2}{k_m P} \frac{\mathrm{w}^2}{\ell^2} \sqrt{\frac{\rho E}{12}} = \frac{2\pi}{k_m P} \mathrm{w} \rho f_n \tag{4.6}$$

where κ_n is the modal parameter defined in equation (2.12), P is the gas pressure w and ℓ are the cantilever width and length, ρ and E are the mass density and Young's modulus, f_n is the resonance frequency and k_m is defined as

$$k_m = \sqrt{\frac{32M}{9\pi RT}} \tag{4.7}$$

where M, R and T are the molar mass of the gas, the gas constant and the temperature, respectively.

For air molecules, $k_m = 3.6 \times 10^{-3}$s/m. Inserting the data for the cantilevers in equation (4.6) results in $Q = 0.768 f_n/\mathrm{Hz}$, which is more than 40 times higher than the observed Q-factors. The expression in equation (4.6) is valid in the molecular flow regime[4], which for 10 µm wide cantilevers corresponds to pressures below 25 Pa. As this is very close to the pressure of

[4] The molecular flow regime is defined as Knudsen numbers $Kn \gtrsim 10$. The definition of Kn is given in equation (4.11) in section 4.3.5.

50 Pa that was used for characterization, the expression is assumed to be applicable here.

Another specific damping mechanism that has been considered is thermoelastic damping, i.e. irreversible heat conduction between areas of compression and areas of expansion in the vibrating cantilever. Higher frequencies imply less heat transportation and therefore a lower loss, which would result in a higher Q-factor. This, however, only applies for frequencies above a characteristic frequency, given by the expression [67]:

$$f_{\text{therm}} = \frac{\chi}{\pi} \left(\frac{2.225}{h} \right)^2 \tag{4.8}$$

where h is the cantilever height and χ is the thermal diffusivity, which is $\chi = 0.0075\,\text{cm}^2/\text{s}$ for fused silica [68]. Inserting $h = 0.85\,\mu\text{m}$ yields $f_{\text{therm}} = 1.64\,\text{MHz}$. This is the centre frequency of maximal thermoelastic damping. At higher frequencies the vibration becomes adiabatic and the damping will decrease as described, and at lower frequencies the damping will decrease because the cantilever can be considered in thermal equilibrium at all times (isothermal vibration). Calculating the maximal thermoelastic damping for SiO_2 using the formula presented in [67] reveals that it only limits the Q-factor to 127000, meaning that it can not be the cause for any of the observed Q-factors, although the calculated f_{therm} fits well with the fall-off seen at frequencies above 1 MHz.

Photiadis and Judge [69] have derived expressions for the damping of rectangular cantilevers due to the substrate attachment loss. This damping results in Q-factors in the order of 10^6 or more and are therefore clearly not relevant for describing the primary loss mechanisms of the cantilevers characterized here.

No specific dominating damping mechanism has therefore been identified for describing the observed frequency dependence of the Q-factors.

4.3.3 Q-factor dependence on gold coating in vacuum

By characterizing the cantilevers in a vacuum environment, the loss due to viscous damping can be eliminated, and the relative effect of a gold coating on the intrinsic properties of the cantilever can be explored. Figure 4.9 shows the measured Q-factors of the first 6 flexural modes of the cantilever with length $\ell = 209\ \mu\text{m}$ as a function of gold coating thickness.

The internal friction in gold is much higher than in SiO_2, and the gold coating therefore gives rise to a higher internal loss and thus a reduced Q-factor. The most significant reduction in Q-factor appears already for the

100 nm coating, and further increase of the coating thickness leads only to a small additional reduction. This suggests that the Q-factor of resonant cantilever sensors are impaired significantly even by very thin film metal coatings.

The same tendency in Q-factor reduction that is illustrated in figure 4.9 is observed for all of the characterized cantilevers (as quantified in table 4.4). As seen in the figure, the higher order modes are much more severely affected by the gold coating than the low order modes. The Q-factor of mode 1 drops to approximately half the value on average by the 100 nm coating, while the Q-factor of mode 3 and above decreases by at least an order of magnitude.

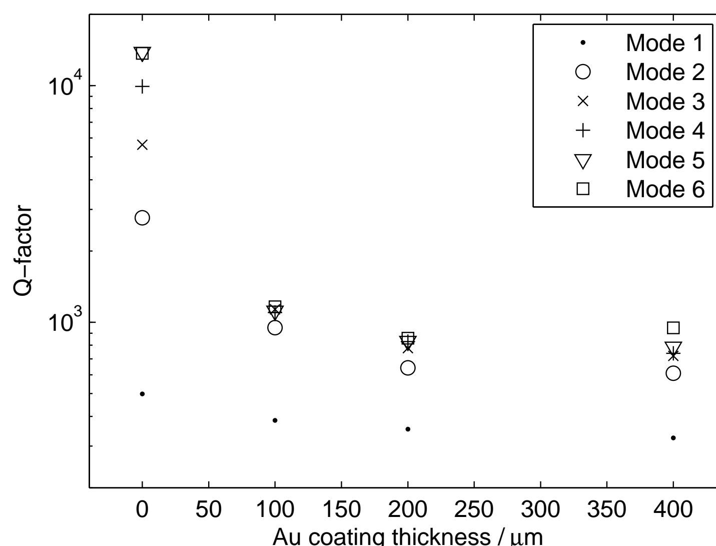

Fig. 4.9: Q-factors in vacuum and at 30 °C of the first 6 flexural modes of the cantilever with length $\ell = 209$ µm as a function of gold coating thickness.

4.3.4 Q-factor dependence on gold coating at atmospheric pressure

The Q-factors at atmospheric pressure (100 kPa nitrogen) are significantly lower than in vacuum. In contrast to the observations in vacuum, the Q-factors at atmospheric pressure increase slightly with increasing gold coating thickness, as seen in figure 4.10. As the energy loss per cycle of vibration is assumed to be increased by the coating, as seen in figure 4.9, it follows from equation (4.1) that the increasing Q-factor can be explained as an increase

Mode	Q/Q_0 (100 nm Au)	Q/Q_0 (200 nm Au)	Q/Q_0 (400 nm Au)
1	0.593 ± 0.189	0.521 ± 0.135	0.454 ± 0.140
2	0.193 ± 0.077	0.145 ± 0.048	0.126 ± 0.049
3	0.107 ± 0.039	0.080 ± 0.023	0.072 ± 0.022
4	0.084 ± 0.014	0.065 ± 0.009	0.059 ± 0.010
5	0.072 ± 0.011	0.062 ± 0.009	0.055 ± 0.007
6	0.080 ± 0.004	0.051 ± 0.009	0.059 ± 0.012
7	0.058 ± 0.021	0.051 ± 0.014	

Table 4.4: Average values and standard deviation of the relative Q-factors of the coated cantilevers with respect to the Q-factors of the uncoated cantilevers, measured in vacuum.

in total vibrational energy. This makes good sense considering the increased mass density of the gold coated cantilever. The mass of the 830 nm thick SiO_2 cantilever is almost doubled by the addition of 100 nm Au, implying that the vibrational energy for a constant oscillation amplitude is almost doubled as well.

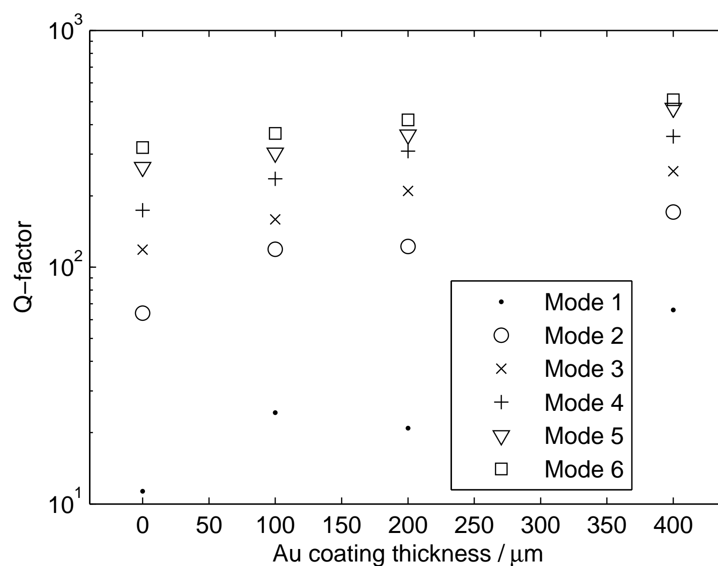

Fig. 4.10: Q-factors in 100 kPa N_2 and at 30 °C of the first 6 flexural modes of the cantilever with length $\ell = 209$ µm as a function of gold coating thickness.

4.3.5 Resonance frequency dependence on pressure

The resonance frequency of a cantilever vibrating in a gaseous environment is dependent on the pressure of the gas. When the pressure is increased, the resonance frequency will decrease. This effect is caused by the increased amount of gas that moves with the cantilever when it is vibrated, resulting in an increase in the effective mass of the cantilever. A rigorous and satisfactory model of the fluidic damping of resonant cantilevers has yet to be developed [59], and experimental observations are therefore necessary in order to describe the pressure dependent frequency response of specific structures.

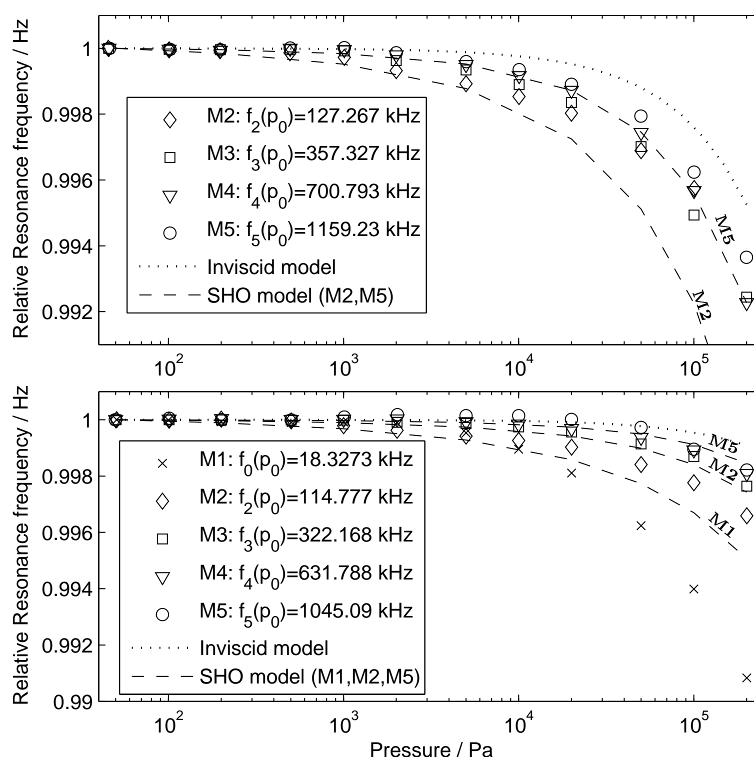

Fig. 4.11: Normalized resonance frequencies of the first five flexural modes (M1-M5) of the uncoated (top) and coated (bottom) cantilevers as a function of pressure. Mode 1 of the uncoated cantilever has been left out due to unreliable data points. The large deviation of mode 1 of the coated cantilever may be caused by the same problem. Also shown is the analytical values of the inviscid model, equation (4.9), and values of the SHO model for selected modes.

The resonance frequencies of the first five flexural modes of the uncoated and 400 nm gold coated cantilevers were measured for 12 quasi-logarithmi-

cally spaced pressures between 50 Pa and 200 kPa. The gas used was dry N_2 at a temperature of 303 K. The results are shown in figure 4.11, and are in accordance with those obtained by Mertens et al.[27]. For both the coated and the uncoated cantilever, the resonance frequencies of all modes are almost constant (less than 0.1 % variation) for pressures below ≈ 5 kPa, whereafter they start to decrease.

An analytical expression for the change in resonance frequency of flexural modes of rectangular cantilever plates submerged into water has been derived by Lindholm et al.[70], and elaborated by Liang et al.[71]. It can easily be rewritten to a form that describes cantilever vibration in a gas:

$$f_{n,\text{gas}} = f_{n,\text{vac}} \left(1 + \frac{\pi M P\, w}{4 R T \rho\, h}\right)^{-1/2} \tag{4.9}$$

where M is the molar mass of the gas, P is the pressure, $R = 8.314$ J/(mol K) is the gas constant and T is the absolute temperature. For a multi-layer cantilever $\rho\, h$ should be replaced by $\sum_i \rho_i h_i$.

This model does not take the viscosity of the fluidic medium into account, and is therefore only valid for high Reynolds numbers. The Reynolds number of a cantilever, oscillating with frequency f in a fluid with viscosity and density η and ρ_{fluid} is given by [59]

$$Re = \frac{\pi \rho_{\text{fluid}} f\, w^2}{2\eta} \tag{4.10}$$

where w is the cantilever width. For nitrogen, the viscosity is $\eta = 16.58$ μPa s and the density is $\rho_{\text{fluid}} = 1.16$ kg/m^3 at room temperature and atmospheric pressure. Nitrogen can be considered an inviscid fluid for the cantilever oscillation when $Re \gg 1$. This requirement is fulfilled for $w = 10$ μm when the pressure–frequency product is $P \cdot f \gg 10^{10}$ Pa Hz; this corresponding to high order modes with $f_n \approx 1$ MHz at atmospheric pressure.

The validity of the *inviscid* model also requires the gas flow to be in the continuum regime. The Knudsen number which characterizes different regimes of flow can be defined as [27]

$$Kn = \frac{1}{D \sigma w} \tag{4.11}$$

where D is the molecular density of the gas and σ is the collision cross section, which is 1.72 nm^2 for nitrogen. For $Kn \lesssim 0.01$, the gas may be considered a continuum, while $Kn \gtrsim 10$ defines the free molecular regime. For 10 μm wide cantilevers in nitrogen, these numbers correspond to pressures above 25 kPa and 25 Pa respectively.

At pressures above 25 kPa, equation (4.9) therefore applies, and the change in resonance frequency for the cantilevers is obtained by inserting $M = 28.0134$ g/mol for nitrogen together with the data for the cantilevers. The resulting curve is shown together with the experimental values in figure 4.11.

The small but notable tendency for the higher order modes to be less affected by pressure than the lower order modes is not accounted for by the inviscid model, which generally predicts resonance frequencies that are too high. Nevertheless, the agreement with the experimental data is quite good, considering the simplicity of this model.

A more rigorous model, describing the frequency response of cantilevers in terms of both resonance frequencies and Q-factors, is presented by Sader et al. in [59]. This model takes the viscosity of the medium into account and the experimental verification presented in [55] shows very good agreement with measurements. The expression of this model for the change in cantilever resonance frequency is:

$$f_{n,\mathrm{gas}} = f_{n,\mathrm{vac}} \left(1 + \frac{\pi M P \, \mathrm{w}}{4 R T \rho \, h} \Gamma_r(Re) \right)^{-1/2} \tag{4.12}$$

This is similar to that of equation (4.9), but includes the effect of viscosity through the real part, Γ_r, of the correction function $\Gamma(Re)$, which – for a rectangular cantilever – solely depends on the Reynolds number, Re. For inviscid media ($Re \to \infty$), $\Gamma_r(Re) \to 1$, and the two models become identical. A full expression of $\Gamma_r(Re)$ is presented in [59]. The model is valid when dissipative forces are small, in which case the cantilever can be considered a simple harmonic oscillator (SHO). The model is therefore referred to as the SHO model. Further prerequisites for the validity of the model are presented in [59]; these are reasonably well satisfied by the cantilevers characterized here, with the exception of the presence of high internal friction in the gold-coatings. This primarily affects the Q-factors, and not so much the resonance frequencies, as can be seen in figure 4.11, where the analytical values correspond equally well for the coated as for the uncoated cantilever.

There is a tendency for the SHO model to overestimate the effect of the viscosity on the effective mass of the uncoated cantilever, i.e. the predicted resonance frequencies are too low; whereas the effect of viscosity is underestimated for the coated cantilevers. While the SHO model is shown to be in excellent agreement with experimental data obtained by Sader et al.[72], other comparisons [39] estimate the model to be less superior[5].

---

[5] Gibson et al.[39] find that the SHO model has a ±15 % uncertainty in determining the spring constant of gold coated AFM cantilevers.

The measurements are in relatively good agreement with both the inviscid and the SHO models, although neither of these models can be used to give exact predictions of the pressure dependency of the cantilever resonance frequencies.

4.3.6 Q-factor dependence on pressure

The detailed pressure dependence of the Q-factors of the uncoated and the 400 nm gold coated cantilever is illustrated in figure 4.12 (a).

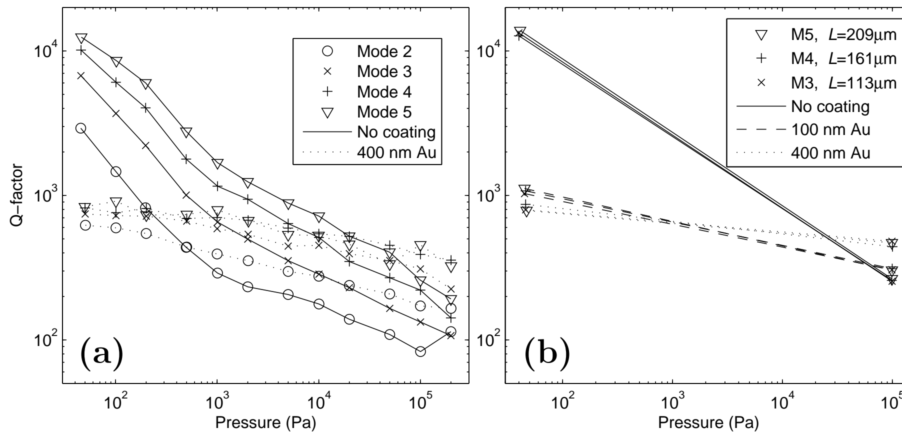

Fig. 4.12: **(a)** The Q-factor of mode 2–5 of the uncoated cantilever and the cantilever with 400 nm Au coating, illustrating the general pressure dependence.
(b) The Q-factor of three modes of different cantilevers, having almost identical resonance frequencies.
The drawn lines should not be interpreted as an interpolation between the measured values but rather as a visual aid in distinguishing the different data points.

The Q–P-plot shows a general pressure dependence that resembles a straight line (i.e. $Q \approx \beta P^{\alpha}$). Though this description is not entirely accurate, it is useful for a qualitative treatment of the modes that have only been characterized at vacuum and atmospheric pressure, as seen in figure 4.12 (b).

The almost parallel curves in figure 4.12 (a) suggest that the relative Q-factor decrease is identical for all modes and only varies with the coating thickness. To verify this, three different order modes on different cantilevers with almost identical resonance frequencies have been identified:

mode 5 for $\ell = 209$ µm with $f_5 = 1027$ kHz
mode 4 for $\ell = 161$ µm with $f_4 = 1038$ kHz
mode 3 for $\ell = 113$ µm with $f_3 = 1065$ kHz

The Q-factors of these three modes have been plotted in figure 4.12 (b) for vacuum and atmospheric pressure and for different coating thicknesses.

As noted in section 4.3.2, the Q-factor of a mode is mainly determined by its resonance frequency. This is further confirmed by figure 4.12 (b), which shows that the mode number and cantilever length has no implicit effect on the measured Q-factors. The graph verifies that the Q-factors of the cantilevers at any specific pressure are determined primarily by the resonance frequency, and that the relative pressure dependence of the Q-factors is defined primarily by the gold coating thickness.

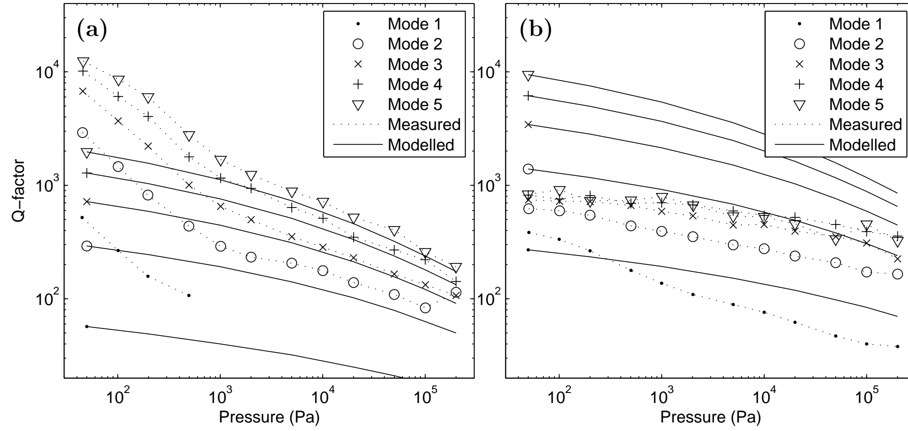

Fig. 4.13: **(a)** Measured and calculated Q-factors of mode 1–5 of the uncoated cantilever. Some points of Mode 1 have been left out due to unreliable measurement points.
(b) Measured and calculated Q-factors of mode 1–5 of the 400 nm Au coated cantilever.

The SHO model described in the previous section also provides an expression for the cantilever Q-factors due to viscous damping [59]:

$$Q = \frac{\frac{4RT\rho h}{\pi MP w} + \Gamma_r(Re)}{\Gamma_i(Re)} \tag{4.13}$$

where Γ_r and Γ_i are the real and imaginary parts of the correction function $\Gamma(Re)$.

The modelled values of the Q-factors for the two cantilevers are compared to the experimentally obtained values in figure 4.13. As concluded for the resonance frequencies, the SHO model overestimates the viscous damping for the uncoated cantilevers, where it predicts Q-factors that are an order of magnitude too low in vacuum, although they seem to coincide with the

measured values of the higher order modes at higher pressures. For the gold coated cantilevers, the SHO model apparently underestimates the viscous damping in predicting too high Q-factors – especially for the higher order modes. Another explanation for the lower measured Q-factors is that the internal friction of the gold layer is the dominating loss factor, and that it is this loss that sets an upper limit to the Q-factors of the gold coated cantilevers.

4.3.7 Resonance frequency dependence on temperature

The material properties of the cantilevers, such as density and elasticity, are temperature dependent. For the density of mass (ρ), the dependence is very small and is the result of thermal expansion with constant mass. Young's modulus of elasticity (E) also shows a temperature dependence. Both these effects influence the resonance frequency, which has been measured for the uncoated and the 400 nm gold coated cantilever at six different temperatures in the range from 30 °C to 80 °C.

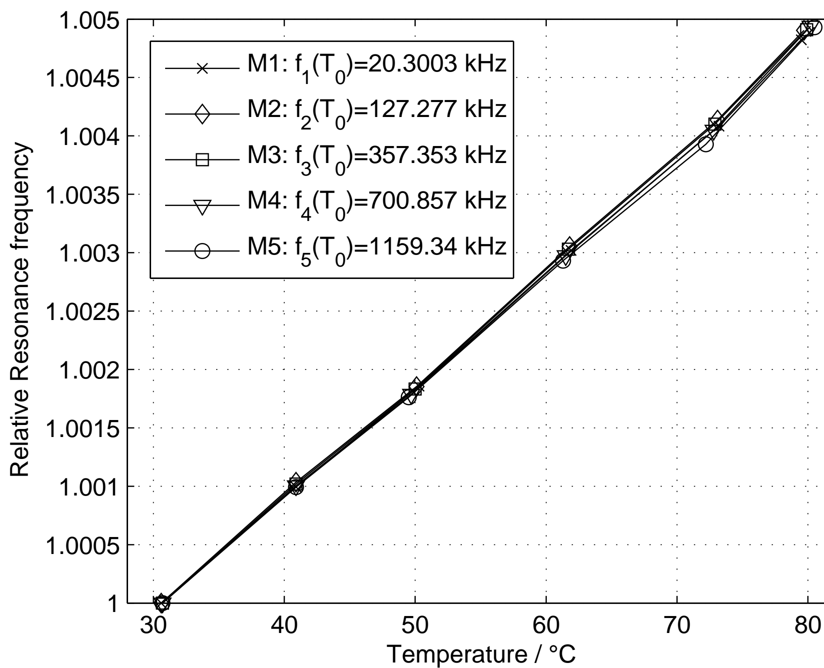

Fig. 4.14: Normalized resonance frequencies of the first five flexural modes (M1-M5) of the uncoated cantilever as a function of temperature.

The results for the uncoated cantilever are displayed in figure 4.14. There

is clearly a linear dependence between the change in temperature, ΔT, and the change in relative resonance frequency. Fitting all the data points with a straight line yields the relation

$$\frac{\Delta f_n}{f_n(T_0)}\Delta T^{-1} = (9.79 \pm 0.06) \times 10^{-5}\mathrm{K}^{-1} \tag{4.14}$$

The effect due to thermal expansion alone can be determined by inspecting equation (2.16). Both h and ℓ are subject to thermal expansion, (i.e. proportional to $1 + \alpha\Delta T$), and ρ changes as $\rho \propto (1 + \alpha\Delta T)^{-3}$. The resonance frequency, f_n is therefore proportional to $\sqrt{1 + \alpha\Delta T}$. A first order approximation to this can be expressed as

$$\frac{\Delta f_n}{f_n(T_0)}\Delta T^{-1} \approx \frac{\alpha}{2} = 2.5 \times 10^{-7}\mathrm{K}^{-1} \tag{4.15}$$

where the value $\alpha = 0.5 \times 10^{-6}\mathrm{K}^{-1}$ has been used for thermal silicon dioxide. Clearly the thermal expansion is negligibly small compared to the effect seen in the measurements, and the dominating effect governing the observed change in resonance frequency is therefore presumed to be the thermal dependence of the elasticity, E. Young's modulus can be expressed as a linear approximation:

$$E = E_0\,(1 + \beta \cdot \Delta T) + \mathrm{O}(\Delta T^2) \tag{4.16}$$

By combining equation (2.16) and equation (4.16) and inserting the experimental value of equation (4.14), the thermal coefficient of Young's modulus is obtained as:

$$\frac{\Delta f_n}{f_n(T_0)}\Delta T^{-1} \approx \frac{\beta}{2} \Leftrightarrow \beta \approx 19.58 \times 10^{-5}\mathrm{K}^{-1} \tag{4.17}$$

This corresponds well to the values for fused silica, as measured and depicted by McSkimin in [25]. Here $E_0 \approx 73$ GPa and $\beta \approx 18.5{\times}10^{-5}\mathrm{K}^{-1}$ at $T = 30$ °C. It is worth noticing that Young's moduli for fused silica and silicon dioxide have positive temperature coefficients (i.e. the material gets more rigid with increasing temperature), contrary to e.g. silicon. This effect may be utilized to form multi-layer cantilevers with zero effective temperature coefficient of elasticity [26].

The measurements carried out on the gold coated cantilever for varying temperature are displayed in figure 4.15. The behaviour of the different modes is non-trivial and highly irregular. The relative change in the resonance frequencies of the different modes should theoretically be identical,

since the absolute frequencies are scaled by the factor $(\kappa_n \ell)^2$, given by the expression in equation (2.12). Inspection of the gold coated cantilever in a scanning electron microscope revealed a grain size of approximately 50 nm, as seen in figure 4.16. The inhomogeneous structure of the gold could have an influence on the internal friction, affecting the individual modes differently, and may be the reason for the observed behaviour. Further studies of this must be carried out in order to draw any final conclusions.

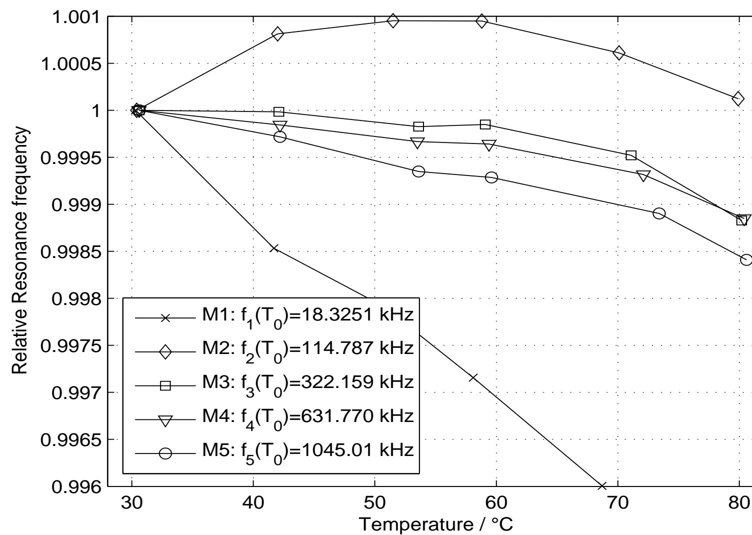

Fig. 4.15: Normalized resonance frequencies of the first five flexural modes (M1-M5) of the 400 nm gold coated cantilever as a function of temperature.

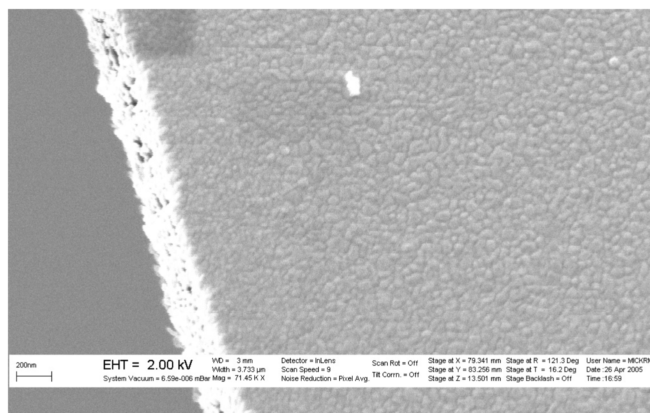

Fig. 4.16: SEM image of the surface and edge of the 400 nm gold coated cantilever, revealing a grain size of approximately 50 nm.

4.3.8 Q-factor dependence on temperature

The Q-factors of the coated and uncoated cantilevers can also be expected to change with temperature because of the changes in hardness or elasticity.

The normalized Q-factors of the uncoated cantilever are shown in figure 4.17. A small increase in Q may be observed, which could also be expected because of the increasing modulus of elasticity that raises the resonance frequency. However, the uncertainty in the Q-factor measurements is greater than any such tendency, implying that the apparent increase in Q could also be purely coincidental. Any attempt to quantify the temperature dependence of the Q-factor would be pointless with the large deviations in the measurements.

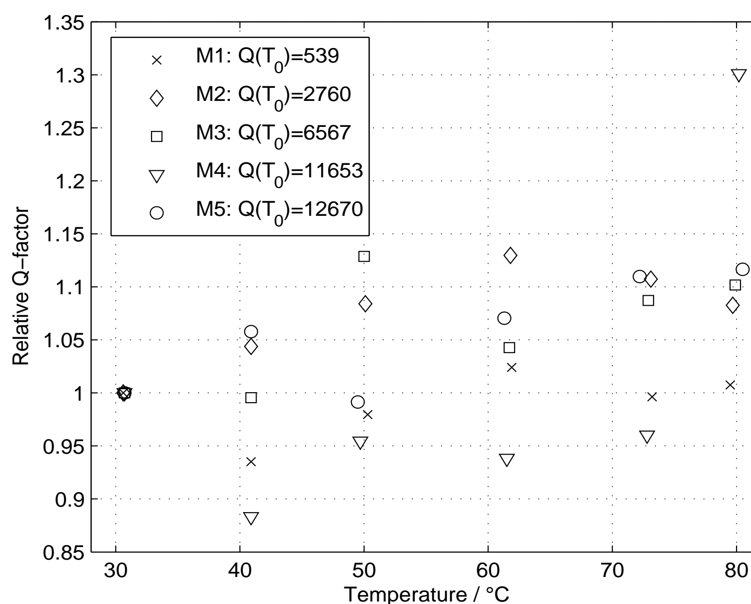

Fig. 4.17: Relative Q-factor, $Q(T)/Q(T_0)$ vs. temperature, for modes 1–5 of the uncoated silicon dioxide cantilever in vacuum.

In figure 4.18, the normalized Q-factors of the 400 nm gold coated cantilever are shown. Whereas no significant temperature dependence could be seen for the uncoated cantilever, a clear decrease in Q is seen for the gold coated. This decrease is almost identical for all 5 modes – the differences between modes being comparable to the uncertainty in the Q-factor measurements.

The minimum obtainable *vacuum* pressure in the chamber rises from 48 Pa to 62 Pa with temperature as seen in figure 4.19, and in figure 4.12 it was seen how the Q-factor decreased with increasing pressure. This pres-

sure dependence of the Q-factor, however, is much too small to explain the decrease in Q observed, implying that the major effect causing the Q-factor of the gold coated cantilever to decrease with increasing temperature presumably is an increased energy dissipation in the cantilever due to increasing internal friction (i.e. *softening*) of the gold layer when being heated.

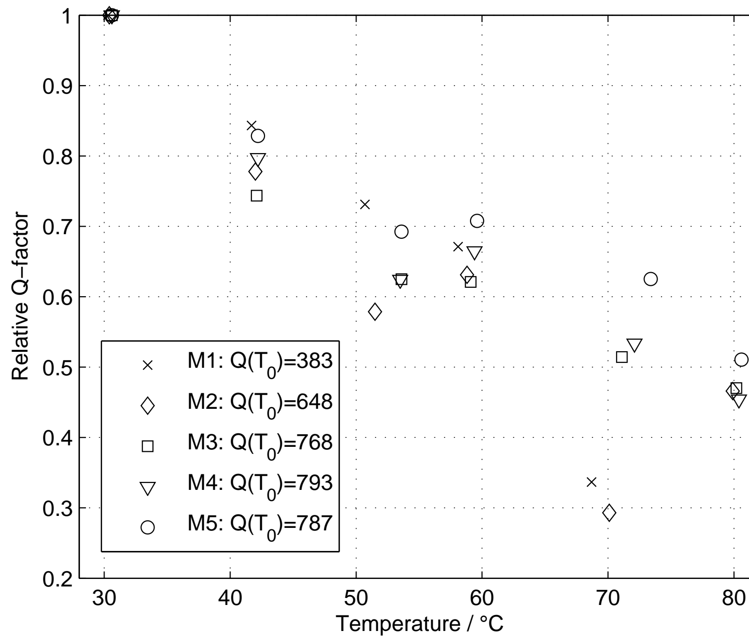

Fig. 4.18: Relative Q-factor, $Q(T)/Q(T_0)$ vs. temperature, for modes 1–5 of the 400 nm Au coated cantilever in vacuum.

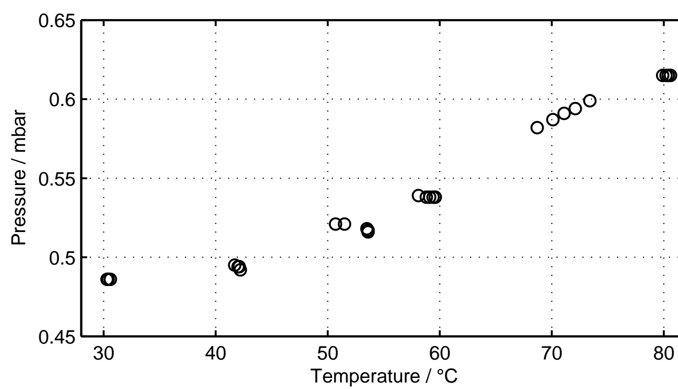

Fig. 4.19: Obtained *vacuum* pressure at measurement time for different temperatures.

4.4 Discussion

It was seen that the analytical expression of the resonance frequency of multilayer cantilevers is in good agreement with experimentally obtained as well as simulated values, and may be used as a less time-consuming alternative to finite–element modelling when evaluating cantilever performance.

In the characterization of gold coated cantilevers a clear dependence between resonance frequency and Q-factor was observed. A high resonance frequency implies a high Q-factor, and for cantilever-sensor applications, an obvious conclusion would therefore be, that using a higher order mode for detection will yield a higher sensitivity. A higher resonance frequency and Q-factor may also be achieved by fabricating a shorter cantilever, but at the same time this would reduce the functionalized surface area, and would therefore not provide the same improvement in sensitivity.

In vacuum, the Q-factor is severely reduced by the deposition of even a thin metal film; especially for higher order modes. This sets a limit on the high sensitivity of metal coated nanocantilever sensors, and calls for alternative functionalization methods, such as partial gold coating of the cantilever tip, or even functionalization of separate objects attached to uncoated cantilevers [73].

At atmospheric pressure, an improvement of the Q-factor was observed for metal coated cantilevers, suggesting that a high mass density is more important than a high intrinsic Q-factor for cantilever sensors operating in a non-vacuum environment. A consequence of this is to maximize the thickness of such cantilever sensors and use denser materials for fabrication. The two major drawbacks of using denser materials would of course be a reduced mass sensitivity and a decreased resonance frequency, so some sort of optimization must be done. A new approach to cantilever fabrication would be to generate an optimized material matrix consisting of dense materials mixed with high-stiffness materials, such as nano-fibres – maybe carbon nano-tubes.

The pressure dependence of the resonance frequencies is described well by the model given by Lindholm et al.[70] for large resonating plates, although this model predicts higher resonance frequencies than those measured. Lindholm describes some empirical correction factors to better take the geometry of the rectangular plate into account, but since these factors all have the effect of increasing the predicted frequencies, they are apparently not applicable to micro- or nanocantilevers. The model by Sader et al.[59] provides a correction function which predicts lower resonance frequencies. The predicted resonance frequencies are dependent on the resonant mode order in a manner similar to the observed results, which leads to the conclusion that Sader's model is a considerable improvement over Lindholm's.

The thermal dependence of the resonance frequency of the uncoated silicon dioxide cantilevers could not be explained in terms of thermal expansion, which is negligibly small, and so the temperature dependence of the elastic properties (i.e. Young's modulus) is presumed to cause the observed change in resonance frequency. In the deduction of the temperature coefficient of E, it was found that E increases with T; an unusual property that may be utilized to fabricate multi-layer cantilevers with zero effective temperature coefficient of elasticity.

4.5 Outlook

The experiments on the resonant properties of gold coated SiO_2 cantilevers, presented here, have given rise to a number of ideas and considerations about improvements and detailed investigations. Some of these are mentioned here.

- The cantilevers that were characterized here only differ in length and have the same width and thickness. Furthermore, they are all much longer than they are wide, and much wider than they are thick. The observed resonance frequency and Q-factor dependencies on pressure and coating thickness may be specific to this $\ell \gg w \gg h$ geometry, and different conclusions may be drawn for significantly different geometries, which should therefore be investigated further.

- The derivation of the thermal coefficient of Young's modulus for thermally grown silicon dioxide should be measured more accurately by characterization of SiO_2 cantilevers with different widths and thicknesses. The precision in the measurements presented here is excellent (within 1 %), but the presence of systematic errors cannot be ruled out.

- The dramatic decrease in Q-factors by the deposition of 100 nm gold clearly indicates that much thinner depositions will have significant effects. Even the 10 nm titanium layer that was used for adhesion may make a considerable difference. A number of experiments could be carried out to investigate this further:

  - Vary the thickness and/or material of the adhesion layer.
  - Use different metals for coating, in order to identify relationships between damping and metal properties.
  - Characterize cantilevers with varying thickness of thin-film gold coatings below 100 nm.

- Vary the grain size in the metal coating layer by annealing and/or different deposition methods. The grain size and other material defects may be a significant parameter for the damping due to internal friction.
- Fabricate cantilevers with different surface roughness, as this too may influence the damping in the oxide–metal border region significantly.

The result of these experiments would be a step towards a solid platform of knowledge for fabrication of high-Q cantilevers.

- The observed damping of the coated cantilevers may be unnecessarily high, because of the multiple deposition steps. The characterization of the cantilevers between depositions must almost unavoidably have resulted in small amounts of particles between the oxide and the different gold layers, and thus caused a higher internal friction from these impurities.
- A method to fabricate cantilevers with high Q-factors and with the adsorption and functionalization properties of a full gold coating would be to do a deposition of gold nano-particles on the surface of SiO_2 cantilevers[6]. If the particles are not in contact then very little stress or internal friction may be expected, while the total surface area of the particles may be as high as (or even higher than) that of the monolithic cantilever.
- The current method of measuring the Q-factor by fitting a Lorentz-curve to the amplitude response of a frequency sweep is not very accurate. A different technique that may yield more accurate measurements would be to actuate the cantilever by a short pulse and measure the exponential decay of the resonant oscillation amplitude as suggested by Höök et al.[74].

[6] This idea was suggested to me by Kristian Mølhave, MIC.

Chapter 5

DNA Detection

5.1 Introduction

Cantilever sensors can be used for DNA detection by means of thiol–gold chemistry [75]. Single-stranded DNA may be attached to a gold surface and used as a functionalization layer that complementary single-stranded DNA will bind to by hybridization.

DNA-detection using cantilever sensors is conventionally done by static operation, where the surface stress of hybridized DNA causes the cantilever to bend. An investigation was done to see if the DNA could be detected using a resonant cantilever based on the mass change by the hybridized DNA strands.

This investigation further spun off the idea of patterning the functionalized part of the cantilever in order to get hybridization on specific areas of the cantilever surface e.g. at the tip only. Being able to pattern a cantilever with different DNA sequences in different areas would possibly also enable detection of these sequences individually by using different modes [73].

The possibility of patterning a single-stranded–DNA–coated gold surface by means of *burning* away the DNA layer in a laser lithographic process was investigated. The laser used is an argon laser with adjustable output power and adjustable writing speed. Part of the laser power is absorbed in the gold surface, and if sufficient heat is generated in the absorption, the exposed area will be de-functionalized.

5.2 Sensitivity calculation

In order to detect the hybridization of DNA with a resonant cantilever, the mass change of the cantilever from the attached single stranded DNA must

induce a sufficiently high change in resonance frequency.

The mass change per surface area can be evaluated from the hybridization surface density and the mass of the single-stranded DNA molecule.

The hybridization density on poly-crystalline gold is expected to be slightly more than $5 \cdot 10^{12}$ cm^{-2} [76].

The target DNA sequence used was the single-stranded 25'mer sequence: 5'-TGC CAC GCT CAT CGA CAA GCT TGT C-3'. The mass of this molecule can be calculated by summing up the atomic masses of the atoms that it consists of. The chemical structure of the four different bases are shown in figure 5.1. In the DNA-strand, each base is bonded to the structure shown in figure 5.2. The mass of the individual DNA-bases are listed in table 5.1, and the mass of the 25'mer sequence is seen to be 12.644 zg, and the mass change per surface area is thus expected to be

$$\sigma_{\text{mass}} = 12.644 \text{ zg} \times 5 \cdot 10^{12} \text{ cm}^{-2} = 632.2 \text{ pg/mm}^2 \tag{5.1}$$

DNA-base	mass / atu	mass / zg
Thymine	303.19	0.50346
Adenine	312.20	0.51842
Cytosine	288.17	0.47852
Guanine	328.20	0.54499

Table 5.1: Masses of the four DNA-bases in single-stranded DNA.

For a cantilever that is functionalized on the entire top surface, the mass-induced resonance frequency shift due to hybridization can be derived from equation (2.16) in chapter 2, and is given by

$$\frac{\Delta f_0}{f_0} = -\frac{\sigma_{\text{mass}}}{2h\rho} = -0.0000831295 \tag{5.2}$$

where $h = 960$ nm is the height of the cantilever (850 nm SiO_2 coated with 10 nm Ti and 100 nm Au); $\rho = 3961$ kg/m^3 is the density of the cantilever, taken as a weighed average of the three layers. We have assumed in the derivation of the sensitivity that the elasticity of the cantilever remains unaltered by the hybridization. As the hybridization induces a high surface stress which results in a bending of the cantilever, this assumption is not well satisfied.

The calculated frequency change is fully resolvable by a cantilever with a Q-factor of approximately 12000, which is not unrealistic when using higher

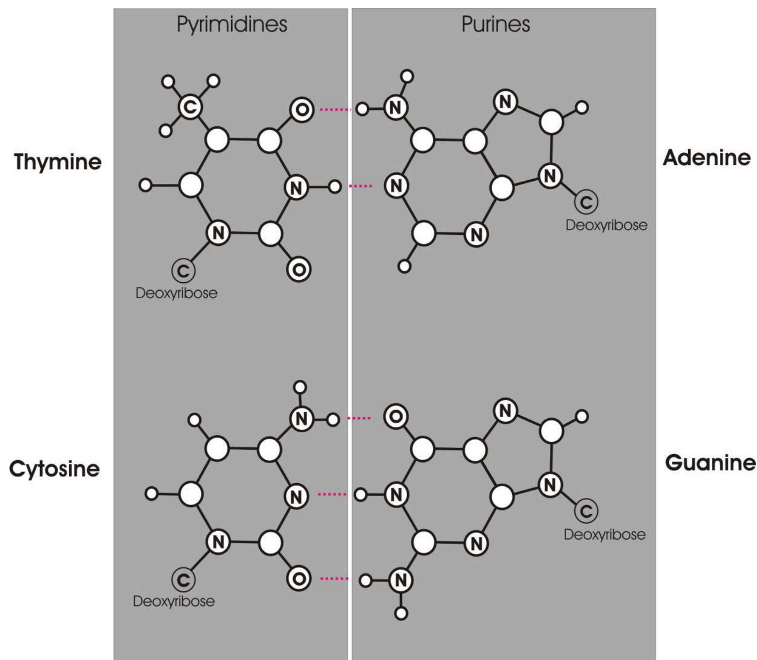

Fig. 5.1: Structure of the four DNA-bases. The illustration is borrowed from [75] with permission.

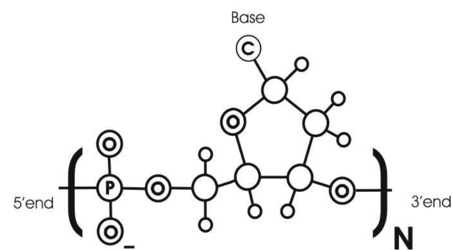

Fig. 5.2: The polymeric scheme of Deoxyribose Nucleic Acid (DNA). The illustration is borrowed from [75] with permission.

order modes. If necessary, new cantilevers could be fabricated with thinner gold coatings. This would yield higher sensitivities because of the decrease in both h and ρ, and it would furthermore result in higher Q-factors, as discussed in section 4.3.3.

5.3 Laser lithographic de-functionalization

To explore the possibility of de-functionalizing immobilized DNA by laser lithography, a gold coated glass slide was coated with single-stranded DNA and exposed by an argon laser using the 488 nm laser-line.

In the laser-lithographic setup, the focused laser beam has a diameter of approximately 0.5 μm. The laser power is adjustable from zero to approximately 50 mW, and the beam spot is scanned over the sample by means of an X–Y translation stage with adjustable speed.

An exposure test pattern (illustrated in figure 5.3) was designed to investigate the effective linewidth and degree of de-functionalization of the DNA. The translation stage was programmed to follow this test pattern to write it in the DNA. The test pattern includes some structures that are intended to reveal the optimal writing speed and laser power in terms of a small linewidth and a high degree of de-functionalization. The angled lines in the lower left part will show up as a semi-disc in the centre and as distinct lines at a certain distance from the centre. With a 30° angle between them, the radius where the lines become visibly separated is expected to be twice the effective linewidth. The dotted lines in the lower right part is designed to reveal the resolution when writing single points or small spots. The parallel lines with varying separation (lower right as well as upper left) is a different approach to measuring linewidth. As the scanner used to detect hybridization has a resolution of 5 μm, a 0.5 μm line is not expected to show up on the scan, but a series of closely spaced lines may show up as a darker area. By identifying the greatest line-spacing where no DNA has hybridized, as well as the degree of hybridization in the areas with greater line-spacing, the linewidth may be evaluated. The cone is supposed to reveal if all DNA gets de-functionalized when an area (rather than just a line) is being exposed. The MIC-logo is just propaganda.

The test pattern was written on the coated slide in a 3×3 array using the writing speeds [50 μm, 200 μm, 1000 μm] and the laser powers [2 mW, 10 mW, 50 mW]. After exposure, the slide was hybridized with complementary DNA labelled with a Cy5' fluorescence marker and scanned in a fluorescence scanner.

The results are shown in figure 5.4. Unfortunately, and for reasons not known, the background fluorescence turned out much lower than expected. The result of this is a very low contrast between hybridized and non-hybridized areas. None of the test patterns written with 2 mW or 10 mW were visible at all. This probably means that the temperature under the focused laser spot is not high enough to damage the immobilized DNA molecules. With 50 mW laser power, the pattern is visible for all

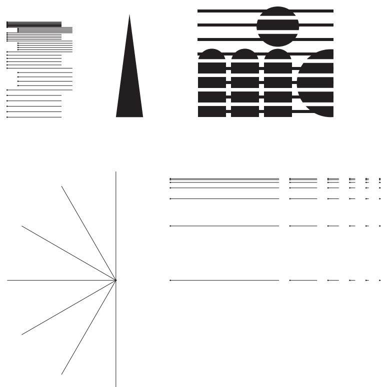

Fig. 5.3: The test pattern for laser lithographic writing. The MIC logo will be written as a raster scan with horizontal lines, 0.5 µm spaced.

writing speeds. Because of the poor contrast, the linewidth is can not be estimated very precisely. Inspection of the structures leads to linewidth estimates of $\delta < 3$ µm at writing speed v = 1000 µm/s; $\delta \approx 6 - 8$ µm at v = 200 µm/s and $\delta \approx 10 - 12$ µm at v = 50 µm/s. An estimate of the degree of de-functionalization in the fully exposed areas is not possible with the low contrast.

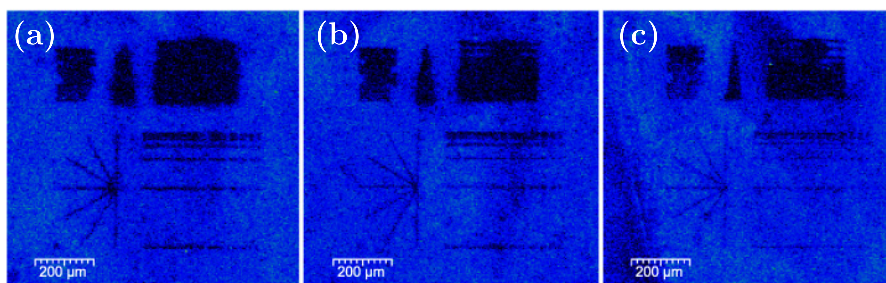

Fig. 5.4: Fluorescence scans of the laser-exposed DNA-coated slide after hybridization. The laser power was 50 mW. The laser writing speed was **(a)** 50 µm/s, **(b)** 200 µm/s and **(c)** 1000 µm/s.

5.4 Discussion

The experiment is a proof of principle that immobilized single-stranded DNA can be de-functionalized effectively and precisely by direct laser exposure.

This may be useful for partial functionalization of cantilever sensors, or for dividing a larger functionalized area into an array of cells for applications where different analytes are sputtered onto an array of identical receptor molecules. The exact reaction that takes place under the exposure has not been identified. Neither has the temperature of the exposed area, and further investigations will be done.

An attempt to expose a glass slide where DNA had been attached by silanization [75] without the use of a gold coating, yielded no result, meaning that the absorption of the laser power must take place in the gold. Using a UV laser for the lithographic patterning is therefore expected to be more reliable, as the UV light is absorbed by the DNA molecule itself. The DNA will be mutated by the UV and thus rendered unable to hybridize.

The biochemistry involved in this work was carried out at MIC by Rodolphe Marie, who also fabricated the micro-fluidic detection cell shown in figure 5.5. A cantilever chip is mounted in the cell, which is sealed to enable a flow of liquid or gas to pass the cantilevers on the chip. For actuation, the entire cell has been glued to a PCB and set in motion by the piezoelectric actuator on the adapter shown in figure 3.10, page 23, and optical laser detection has been done through the top glass layer of the cell. No more than three modes could be detected in vacuum, and the Q-factors were in the range of 100–200. This indicates that a different approach is necessary. A cell designed for integration of both the piezoelectric actuator and the cantilever chip, and with a very thin top glass layer may give a significant improvement in the detection of the higher order cantilever resonances.

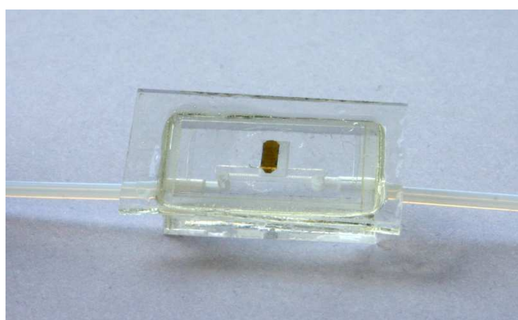

Fig. 5.5: PMMA cell for integrating a cantilever chip with a micro-fluidic channel. External valves and pumps allows for the cantilever to be exposed to different liquid solutions or gasses.

Chapter 6

Vacuum chamber applications

The vacuum chamber described in chapter 3 was designed as part of the Nanomass project [40], in order to characterize the Nanomass cantilever chips electrically and possibly optically. After completion of the chamber setup, a number of other experimental projects were realized, where the measurement capabilities of the setup could be used with great advantage. In this chapter some of these projects are described, with focus on the utilization of the chamber setup.

Section 6.1 describes the characterization of the Nanomass cantilever chip. It is a summary of the work described by Esko Forsén et al. in [77, 78]. In section 6.2 the work done by Søren Dohn [73] on higher order mode actuation and point-mass position-dependent cantilever sensitivity is presented. Section 6.3 is intended to demonstrate as a proof–of–principle that the vacuum chamber and optical detection setup is capable of characterizing alternative resonant structures – other than vertically vibrating cantilevers. The alternative structures described are: in-plane vibrating cantilevers, designed and fabricated by Alexander Grigorov [79] (section 6.3.1); and balanced bridge-structures, designed and fabricated by Zachary Davis (section 6.3.2).

6.1 Fully CMOS integrated nanoresonator system with attogram/Hz mass resolution

Summary of work done by Esko Forsén et al. in [77] and [78].

6.1.1 Introduction

One of the strongly anticipated applications within nanotechnology is ultra-sensitive mass detectors for use in portable, low cost biosensor systems with

low energy consumption and low analyte usage. Resonant nanocantilevers, where mass adsorption induces a measurable change in resonance frequency, constitute a promising approach for such sensors.

Detection of the resonance frequency is primarily done optically. The reason for this is the simplicity and flexibility in the implementation and use of an optical detection system. For fully integrated devices, optical detection is not easily accomplished, and different methods of frequency detection must be used. One highly applicable method is capacitive readout, where the capacitance variation between the cantilever and a parallel electrode gives a measure of the cantilever deflection.

By applying an AC voltage with a DC bias over the cantilever and the electrode, the cantilever is electrostatically actuated into vibration, and the induced displacement current can be amplified and measured. To reduce the effect of parasitic capacitance related to an external amplification and measurement system, the electric detection must be done on chip using e.g. CMOS technology.

Such a system has been implemented and fabricated. The resulting cantilever chips have been characterized under different pressure conditions in the vacuum chamber.

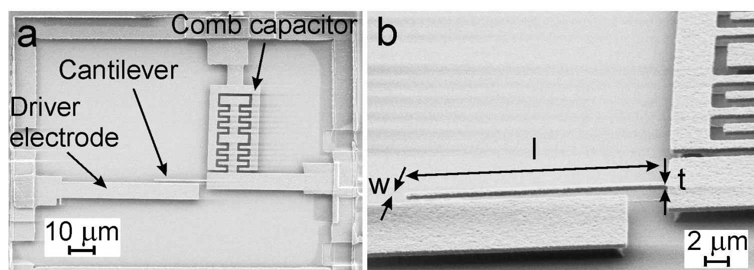

Fig. 6.1: SEM images of the integrated poly-silicon cantilever. (a) Top view of the cantilever structure. The cantilever is excited into lateral resonance by applying an AC and DC voltage between the driver electrode and the cantilever. The comb capacitor is used to polarize the CMOS circuit. (b) Tilted view of the 20 µm long, 425 nm wide and 600 nm thick cantilever.

6.1.2 Results

A poly-silicon cantilever with dimensions $\ell \times w \times h = 20 \times 0.425 \times 0.6\ \mu\text{m}^3$, displayed in figure 6.1, was characterized. The resonance frequency is measured as 1.487 MHz at a pressure of 40 Pa, as shown in figure 6.2 a. The

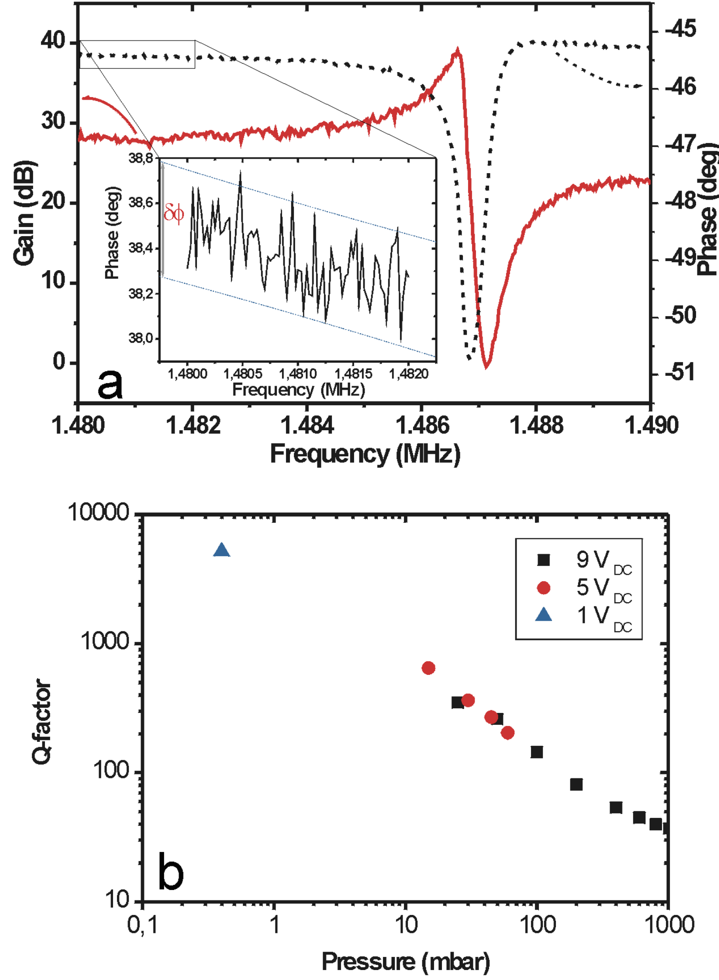

Fig. 6.2: a: Cantilever readout using a gain-phase analyzer, at a pressure of 40 Pa. The inset shows the phase noise of $\delta\phi \approx 0.5$deg. **b:** Q-factor dependence on pressure and applied DC bias voltage.

measured Q-factor is in the order of 5000 at this pressure and drops to 30 at atmospheric pressure, as shown in figure 6.2 b.

The minimal detectable resonance frequency shift in vacuum can be calculated from the measured phase noise, which is $\delta\phi \approx 0.5°$, and the phase slope, $\mathrm{d}\phi/\mathrm{d}f = -0.108°/\mathrm{Hz}$. The result is $\delta f_{0,\mathrm{min}} \approx 4.6$ Hz. From this, the minimal detectable mass can be deduced, using [80]

$$\delta M = \frac{2 \cdot 0.2427m}{f_0} \delta f_0 \tag{6.1}$$

Insertion of the cantilever mass $m = 11.9$ pg into this equation, yields the value $\delta m_{\text{noise}} = 18$ ag for the noise-limited mass resolution. To the author's knowledge, this is the highest reported mass sensitivity of a fully integrated resonator system.

Measurements of the minimal detectable frequency shift at atmospheric pressure yields values in the order of $\delta f_{\text{min}} \approx 1$ kHz, which corresponds to a mass resolution of a few femtograms. This reduction in resolution is caused by a reduced Q-factor, but also an increase in phase noise.

6.2 Enhanced functionality of cantilever mass sensors

Summary of work done by Søren Dohn et al. in [73].

6.2.1 Introduction

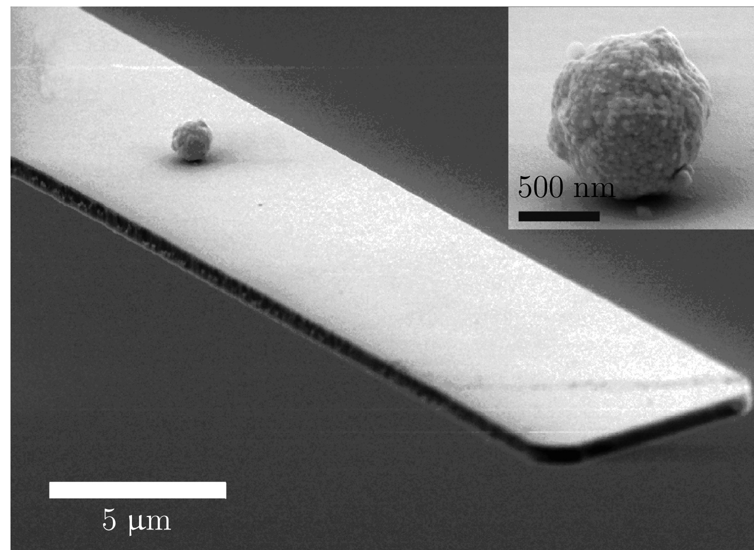

Fig. 6.3: SEM image showing part of the microcantilever and a single gold bead.

In the utilization of cantilevers as sensitive mass detectors, the step from *micro* to *nano* imposes challenges in terms of readout and functionalization, which become increasingly difficult when the cantilevers are down-scaled. The commonly used method of functionalizing the cantilever, by applying

a gold coating on the entire surface, reduces the Q-factor of the resonant modes, thus lowering the mass resolution.

The implications of functionalizing only certain areas of the cantilever, and the optimal position of these areas, have been investigated by positioning a point-mass in the form of a gold bead on the cantilever top surface. The mass responsivity of the cantilever and its dependence on the position of the bead has been determined by laser-optical characterization of the resonant properties at a pressure of 50 Pa.

A gold coated silicon dioxide cantilever with dimensions $\ell \times w \times h = 153 \times 11 \times 1.05$ μm^3 was used for the experiments, and a gold bead with a radius of 0.9 μm and a mass of 60 pg was used as a point-mass, as illustrated in figure 6.3.

6.2.2 Results

The Q-factors of the first four flexural modes were measured. The Q-factor of the 4th mode was observed to be more than 5 times higher than that of the 1st mode, implying that an improved mass resolution may be achieved by higher order mode actuation.

The change in resonance frequency for the first four modes, as a function of position of the gold bead along the length of the cantilever was measured. The results are displayed in figure 6.4 together with values obtained by finite–element simulations, which are in excellent agreement with the experimental values. The bead-position yielding the highest frequency response is at the tip of the cantilever for all four modes, but as higher modes are actuated, more positions with high responsivity occur. The distribution of these positions are specific to the mode, thus presenting the unique option of detecting more than one type of chemical component on a cantilever, by positioning differently functionalized gold beads at the positions specific to different modes, and scanning these modes simultaneously.

6.3 Alternative structures

The optical detection setup for the vacuum chamber was designed for vertically oscillating cantilever devices, but attempts to characterize different types of resonant structures have proven to be successful as well. Two types of alternative structures are presented here to demonstrate the resourcefulness and flexibility of the system setup: in-plane vibrating cantilevers, demonstrating that optical detection with the PSD is possible even though the cantilever deflection occurs in a plane perpendicular to the optical path of

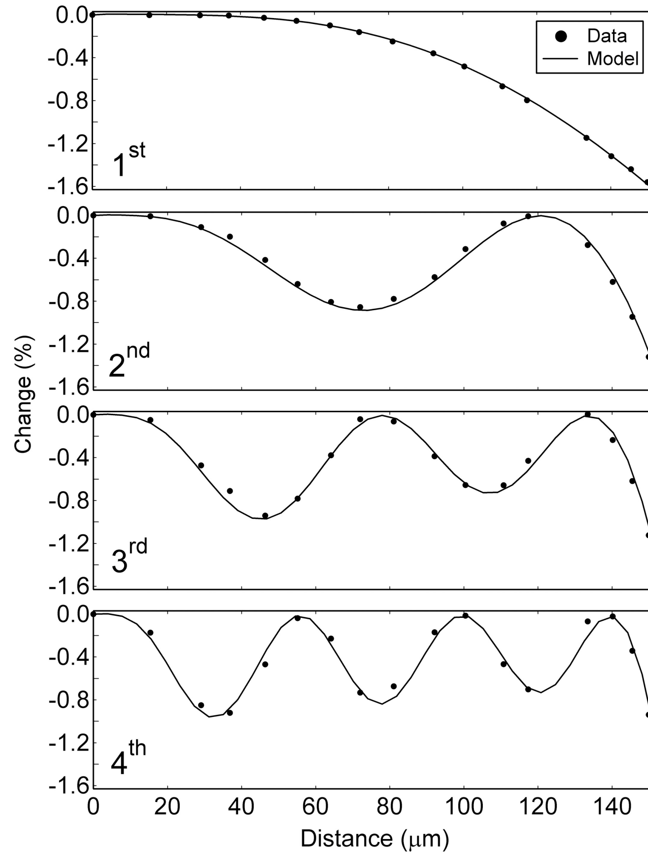

Fig. 6.4: Simulated and measured values of the relative change in resonance frequency for modes 1–4, when a gold bead is attached to the cantilever, as a function of the bead's distance from the cantilever base.

the laser; and micro-bridge resonators, demonstrating that actuation with the PZT-adapter (figure 3.10, page 23) is possible for non-cantilever components.

6.3.1 In-plane vibrating cantilevers

In-plane vibrating microcantilevers of the type displayed in figure 6.5 have been designed and fabricated at MIC by Alexander Grigorov [79]. The dimensions are $\ell \times w \times h = 160 \times 2.0 \times 2.5$ μm^3. The cantilevers are actuated by applying an AC voltage over the two electrodes at the base. This generates an AC current through the base, which will expand and compress due to the periodic heating. Because of the asymmetrical structure of the base,

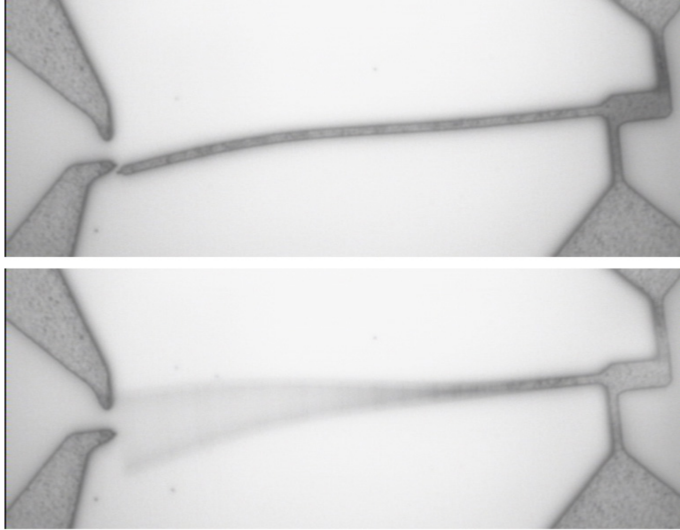

Fig. 6.5: In-plane vibrating cantilever with thermal heating actuation.

the expansion will result in a deflection of the cantilever, and the periodic expansion will set the cantilever in oscillatory motion.

Characterization of the temperature and pressure dependence of the resonant properties of these cantilevers was carried out in a students' project by Morten Fugl. The frequency response of the cantilevers was measured using a GPA in conjunction with the laser-optical detection setup. Despite the in-plane vibration, which does not generate a deflection of the laser beam, quite good results were obtained. The detected signal cannot be caused by deflection of the laser spot, but rather by intensity modulation of the beam. The laser beam is reflected off the substrate surface underneath the cantilever, and the cantilever motion will block part of the beam. The fraction of the beam intensity that is blocked depends on the position of the cantilever, relative to the Gaussian profile of the laser beam. For this particular method of detection, minimizing the beam spot size is not necessarily an advantage, as the best modulation is obtained when the physical amplitude of cantilever vibration is comparable to the dimension of the laser spot.

A measured gain-phase curve is displayed in figure 6.6, showing a resonance peak height of more than 20 dB. The results of the experiments shall not be discussed here; only that Fugl reports accuracies as low as 4 Hz in determining the resonance frequency, which is $f_0 \approx 116$ kHz. According to Fugl's report, this accuracy corresponds to a mass resolution of approximately 120 fg.

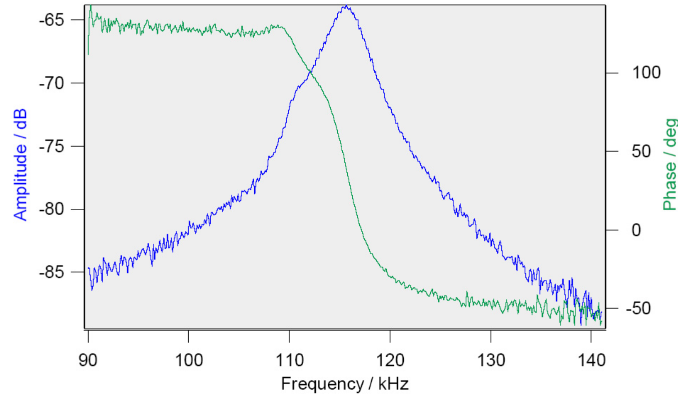

Fig. 6.6: Example of optically detected gain–phase response of in-plane vibrating cantilever.

6.3.2 Micro-bridge resonators

The mechanical actuation by a vertically aligned PZT element, which is an effective method for actuating free-hanging, vertically vibrating cantilevers, has also proven to be successful in actuation of bridge structures as those shown in figure 6.7. The resonators are designed and fabricated at MIC by Zachary Davis.

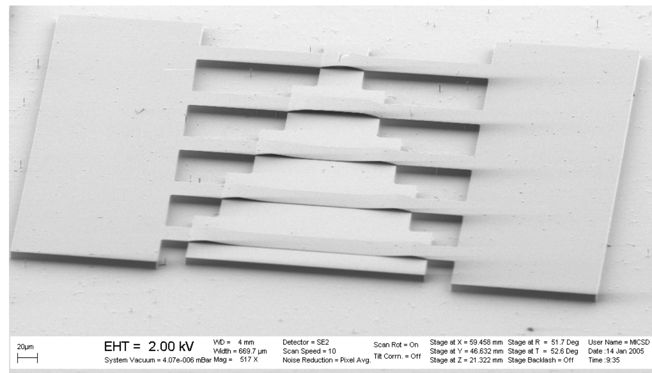

Fig. 6.7: SEM image of micro-bridge resonators. The characterization of the second bridge from the top is presented here.

Resonant motion is observed as illustrated by the gain–phase frequency sweep in figure 6.8. The measurements are done as part of a students' project by Hossein Pakdast and Michael Karimian. The characterized bridge is fabricated in silicon nitride and has the dimensions $\ell \times w \times h = 100 \times 25 \times 0.4$ µm^3.

The theoretical resonance frequency is 373 kHz, which is in very good agreement with the experimental results shown in figure 6.8, obtained in vacuum using the laser-optical detection setup.

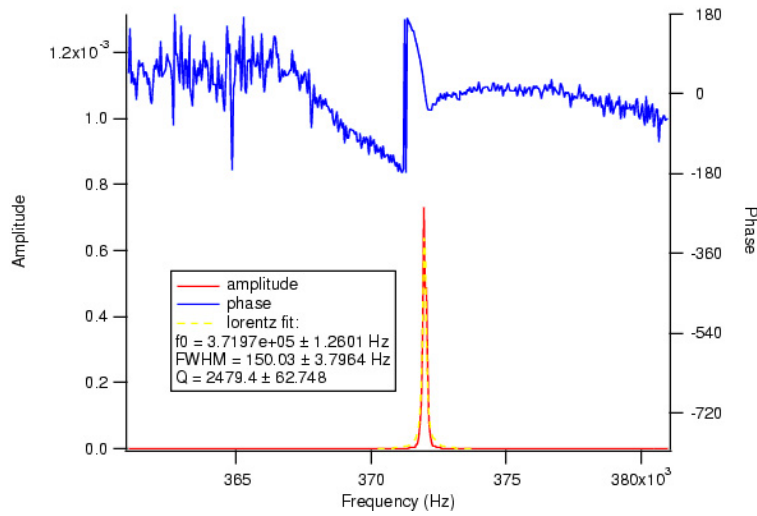

Fig. 6.8: Example of optically detected gain–phase response of balanced micro-bridge resonator.

Chapter 7

Conclusions

One of the main goals of this PhD project was to design and construct an experimental setup for characterization of micro- and nanocantilevers, especially the nanocantilever devices fabricated under the EU Nanomass project. A vacuum chamber was constructed as the main component of this setup. The main capabilities of the vacuum included temperature and pressure control, equipment for introduction of different gases and chemical compounds, electrical interconnections for actuation and signal detection and windows for laser-optical probing and detection of resonant cantilever vibration.

A laser-optical detection system was implemented as part of the experimental setup, and was demonstrated functional on a number of different micro-resonator structures. Beside from standard cantilever structures, these included in-plane vibrating cantilevers, for which a mass detection limit of approximately 120 fg was reported. The experimental setup has been proven flexible, versatile and efficient as a tool for characterization of micro- and nanoresonator devices.

An experimental investigation of the resonant properties of gold coated silicon dioxide cantilevers was performed. The effects of gold coating thickness, temperature and pressure were studied through a series of measurements.

The main results of this investigation can be summarized as:

- The observed resonance frequencies in vacuum showed good agreement with the analytical model that was derived for multi-layer cantilevers, as well as with finite–element simulation results. The analytical model may therefore be of great value in modelling resonant cantilevers, as a fast and easily implemented alternative to finite–element simulations.

- The temperature dependence of the resonance frequencies of the uncoated SiO_2 cantilevers led to an empirical deduction of the thermal co-

efficient of Young's modulus for thermally grown SiO_2. The coefficient was seen to be positive, contrary to most other materials, implying that SiO_2 may be used for composite cantilever structures with temperature independent effective Young's modulus.

- Q-factors were observed to increase for higher order flexural modes, implying that actuation of a high order mode for mass detection will yield a higher mass resolution and improved sensitivity.
- While the Q-factors in low pressures and vacuum were severely reduced by applying a gold coating, the Q-factors at atmospheric pressure were increased. This result was explained as the inertial forces of the gold-coated cantilever being greater than those of the less massive SiO_2 cantilever, and therefor being better at overcoming the dissipative force of the viscous damping.

The results presented here contain information of considerable value for the design and fabrication of resonant micro- and nanocantilevers; and may be used in the development and production of high-sensitivity resonant cantilevers in future applications.

Appendix A

List of publications

R. Sandberg, W. Svendsen, K. Mølhave and A. Boisen, “Temperature and pressure dependence of resonance in multi-layer microcantilevers”, submitted to *J. Micromech. Microeng.* 2005

R. Sandberg, K. Mølhave, W. Svendsen and A. Boisen, “Effect of gold coating on Q-factor of resonant cantilever”, submitted to *J. Micromech. Microeng.* 2005

Søren Dohn, **Rasmus Sandberg**, Winnie Svendsen and Anja Boisen, “Enhanced Functionality of Cantilever Based Mass Sensors Using Higher Modes”, submitted to *Appl. Phys. Lett.* 2005

E. Forsén, G. Abadal, S. Ghatnekar-Nilsson, J. Teva, J. Verd, **R. Sandberg**, W. Svendsen, F. Peréz-Murano, J. Esteve, E. Figueras, F. Campabadal, L. Montelius, N. Barniol, A. Boisen, “Ultrasensitive mass sensor fully integrated with CMOS”, submitted to *Appl. Phys. Lett.* 2005

R. K. Sandberg and L. Leick, “Novel design for integrated wavelength-flat 980/1550 nm pump-signal multiplexer”, in OSA *Trends in Optics and Photonics (TOPS) Vol. 78, Integrated Photonics Research*, OSA Technical Digest, Postconference Edition (Optical Society of America, Washington DC, 2001), pp. IThI3-1–3

Karin N. Andersen, Winnie E. Svendsen, **Rasmus K. Sandberg**, Hugh T. Philipp and Jörg Hübner, “Silicon Rich Nitride Micro-resonators”, in IEE *11th European Conference on Integrated Optics (ECIO)*, Prague, April 2003. WeA2.2., pp. 43–6

R.K. Sandberg, W. Svendsen, A. Boisen, A. Johansson, P.A. Rasmussen, “Temperature dependence of surface stress in nanocantilever mass detectors”, *Danish Physical Society, Annual Meeting 2004*, (Nyborg, Denmark)

Rasmus Sandberg, Alicia Johansson, Peter A. Rasmussen, Rodolphe Marie, Anja Boisen and Winnie Svendsen, “Nanocantilever Sensitivity Degradation From Bimorph Effects”, *Nanotech Insight 2005*, (Luxor, Egypt)

E. Forsén, G. Abadal, S.G. Nilsson, J. Verd, **R. Sandberg**, W. Svendsen, J. Teva, F. Peréz-Murano, J. Esteve, E. Figueras, F. Campabadal, L. Montelius, N. Barniol, A. Boisen, “Fully integrated nanoresonator system with attogram/Hz mass resolution”, *Proceedings of the 8th international conference on Micro Electro Mechanical Systems, IEEE MEMS 2005*, pp. 867-870 (Miami Beach, FL, USA)

S. Dohn, **R. Sandberg**, W. Svendsen and A. Boisen, “Enhanced Functionality of Cantilever Based Mass Sensors Using Higher Modes and Functionalized Particles”, *The 13th International Conference on Solid-State Sensors, Actuators and Microsystems, TRANSDUCERS ’05* (Seoul, Korea, 2005)

S. Dohn, **R. Sandberg**, W. Svendsen and A. Boisen, “Mass Sensitivity of Cantilever Based Mass Sensors as a Function of Mass-Position”, *Materials Research Society, 2005 Spring Meeting* (San Francisco, CA, USA)

Appendix B

Transformation of the Gaussian beam

This appendix summarizes the formulas used to calculate the theoretical, ideal characteristics of the Gaussian laser beam in its propagation through the optical detection system, as described in section 3.5. For full details on laser beams and their characteristics, see [81, 82].

B.1 Gaussian beam characteristics

The Gaussian beam is a fundamental mode of propagating electro-magnetic radiation, and an ideal[1] laser with a cavity defined by a concave spherical mirror in one end, and a plane or concave in the other end will theoretically generate a Gaussian beam of monochromatic, coherent light.

The radiation intensity through a cross section of a Gaussian beam has (not surprisingly) a Gaussian distribution as shown in figure B.1

$$I(r) = I_0 \exp\left(-\frac{2r^2}{w^2}\right) \tag{B.1}$$

where r is the distance from the centre (axis) of the beam, I_0 is the radiation intensity at $r = 0$ and w is the width (radius) of the beam, defined as the distance where the intensity has fallen to $I_0 e^{-2} \approx 0.135 I_0$. I_0 is related to the optical power, P, of the beam by

$$I_0 = \frac{2P}{\pi w^2} \tag{B.2}$$

[1] The term *ideal* in this context implies a perfectly homogeneous gain in the entire laser cavity, perfect spherical mirrors and infinite output aperture, etc. Regular gas lasers can be close to *ideal*.

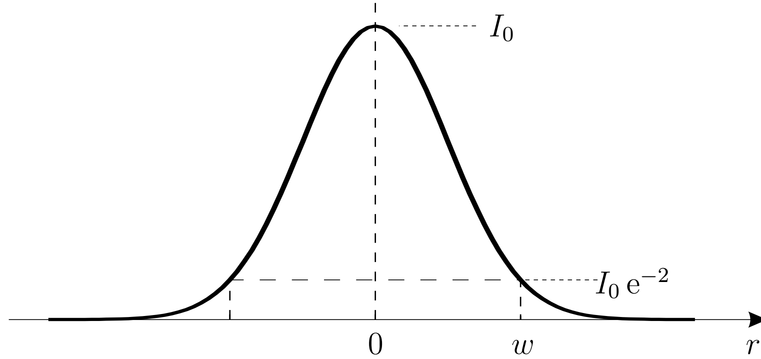

Fig. B.1: Intensity distribution of the Gaussian beam as a function of distance (r) from the beam axis.

The width, w, of the Gaussian beam has a minimum, w_0, called the beam waist, and expands hyperbolically in both axial directions, as shown in figure B.2. If the position of the waist is $z = 0$, the width of the beam at any point along the beam axis is given by

$$w(z) = w_0\sqrt{1 + \left(\frac{z}{z_0}\right)^2} \tag{B.3}$$

where z_0 is called the Rayleigh range and describes the extension (depth) of the focused beam. For $z \gg z_0$, the beam expands almost linearly with z with a divergence half-angle, θ_0.

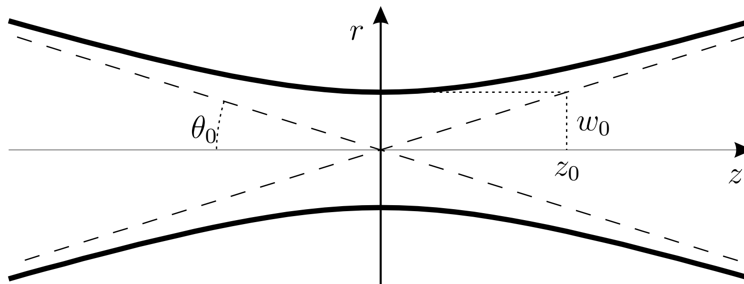

Fig. B.2: Width, $w(z)$, and characteristic dimensions of the propagating Gaussian beam.

The values of w_0, θ_0 and z_0 are interrelated with the radiation wavelength,

λ as:

$$z_0 = w_0\theta_0 = \frac{\lambda}{\pi\theta_0^2} = \frac{\pi w_0^2}{\lambda} \tag{B.4}$$

meaning that if any two of them are known, the other two can be calculated.

B.2 Transformation through a thin lens

A Gaussian beam can be characterized by one complex parameter,

$$q = z_\mathrm{w} + jz_0 = z_\mathrm{w} + j\frac{\pi w_0^2}{\lambda} \tag{B.5}$$

where z_w is the z-position of the waist. If a thin lens with focal length, f, is placed in the beam at the position $z = 0$, the beam will be transformed as

$$q' = \frac{q}{1 - q/f} \tag{B.6}$$

The position of the beam waist, z'_w, after the lens and the waist radius, w'_0, can then be deducted from q' as

$$z'_\mathrm{w} = -\mathrm{Re}(q') \tag{B.7}$$

$$w'_0 = \sqrt{\frac{\lambda \cdot \mathrm{Im}(q')}{\pi}} \tag{B.8}$$

This is illustrated in figure B.3.

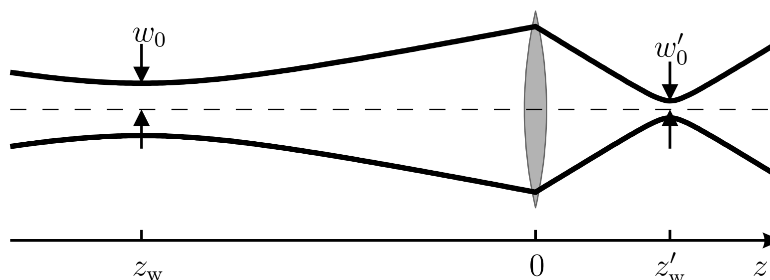

Fig. B.3: Refraction of Gaussian beam through bi-convex thin lens.

Appendix C

Finite-element simulation of gold coated cantilevers

In order to evaluate the experimentally obtained resonance frequencies of coated and uncoated cantilevers (chapter 4) and the corresponding theoretical values (chapter 2 equation (2.15)), the monolithic and gold coated silicon dioxide cantilevers were modelled as a finite–element analysis using the MEMS modelling software CoventorWare.

The cantilever has been modelled as a perfectly rectangular structure, rigidly clamped in one end. For the coated cantilevers, the three layers are modelled as one monolithic structure with different material properties. Alternatively, the coating could be modelled as a separate object, tied to the cantilever substrate. This, however, proved to be less accurate and more time-consuming. The layer heights and material data are listed in table C.1.

Material	h/nm	E/GPa	ν	$\rho/(\mathrm{kg/m^3})$
Thermal Oxide	850	70	0.17	2150
Titanium	10	116	0.33	4500
Gold	400	78	0.44	19300

Table C.1: Layer data for the 400 nm gold coated cantilever model. For uncoated cantilevers, the Ti and Au layers have been disabled. h is the height (thickness) of each layer, E is Young's modulus of elasticity, ν is the Poisson ratio and ρ is the mass density.

The finite–element mesh, displayed in figure C.1 is rectangular (Manhattan bricks). The mesh elements do not overlap the different material layers (no averaging of material properties). The element size is $\Delta x = 3.33$ µm, $\Delta y = 5$ µm and $\Delta z = 1$ µm, corresponding to 3 elements across the width

of the cantilever, 17–42 elements along the length, depending on the value of ℓ and 1 element in the height for each layer.

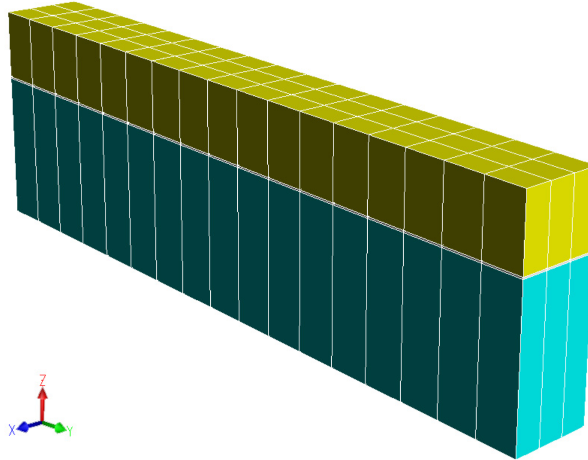

Fig. C.1: Image of the cantilever mesh model used. The Z-axis has been enlarged by a factor of 20 to better visualize the three layers. The displayed cantilever is 89 μm long.

The number of elements in the height and width provide results that deviate less than 0.1 % from the values that a finer resolution of the mesh converges towards. The size of the element in the length direction is a more critical parameter. In order to obtain 0.1 % accuracy, the elements must be in the order of 1 μm, which increases the computation time considerably. The value of $\Delta y = 5$ μm generates results that are accurate within 2 % for all modes with resonance frequencies up to 2 MHz.

For all mesh-resolutions, there is a tendency for the calculated resonance frequencies to be too high when the resolution is lowered. The comparison between simulation and analytical theory (section 4.3.1) showed that the analytical values are generally lower than the simulated. This difference may be partly caused by the mesh resolution in the cantilever length direction, implying that the analytical model may yield results that are even closer to simulated values.

Both the analytical and the simulated resonance frequencies deviate from the experimental values by a few percent, and the chosen mesh resolution is therefore sufficiently good, considering that neither of the models are supposed to be exact descriptions of the actual cantilever structures.

Appendix D

Technical drafts

In the construction of the vacuum chamber and optical detection setup, a number of mechanical components were custom designed (including the chamber body itself). The chamber body was manufactured by Wenzel Vakuum Teknik ApS and Abeto Teknik A/S, and all other components were manufactured by engineering assistants Stig Ahrent Petersen and Poul Erik Hyldbo in the technical workshop of DANCHIP [83].

D.1 Vacuum chamber body

Fig. D.1: 3D visualization of the vacuum chamber body

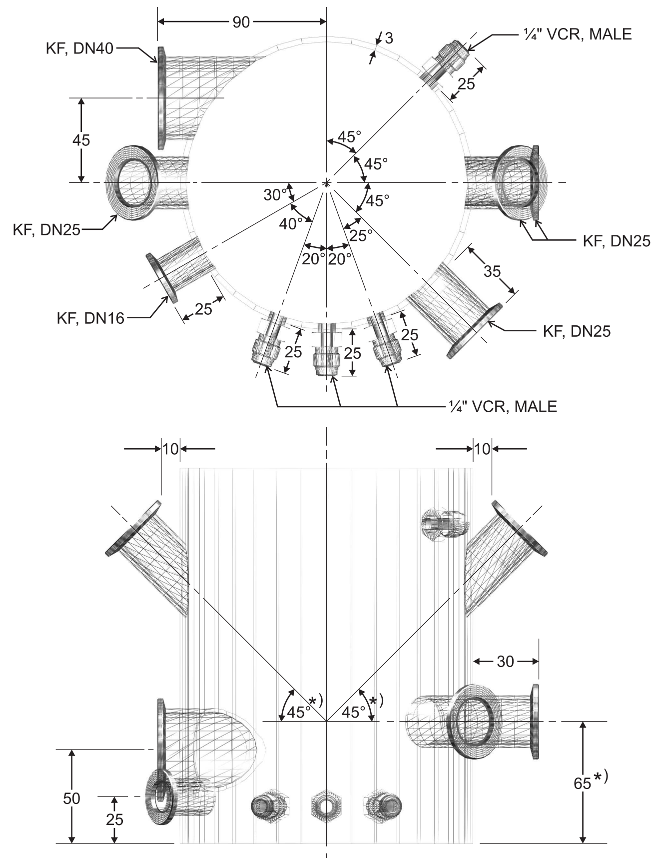

RASMUS SANDBERG
MIC, DAMARKS TEKNISKE UNIVERSITET
17. DECEMBER, 2003

Fig. D.2: Top and front view of chamber body.

*) MEASURES MARKED *) REQUIRE AS HIGH ACCURACY AS POSSIBLE, FOR THE FOUR KF-25 FLANGES TO POINT TOWARDS THE SAME POINT (CENTRE OF CHAMBER, 65 mm ABOVE THE BOTTOM).
ALL OTHER MEASURES MAY BE SLIGHTLY ALTERED IF REQUIRED FOR SIMPLIFICATION OF THE CONSTRUCTION, AS LONG AS THE CLAMPINGS WILL STILL FIT OVER THE FLANGES.

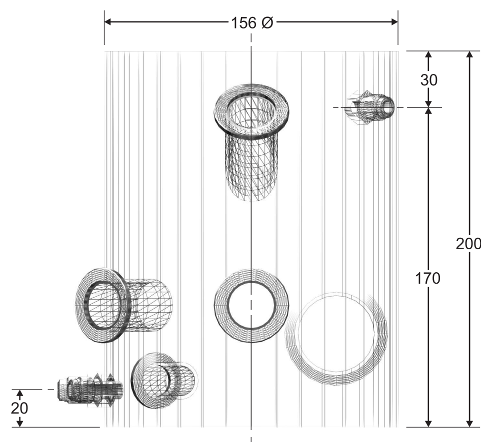

VACUUM CHAMBER

SCALE 1:4, ALL MEASURES IN mm

Fig. D.3: Right side view of chamber body.

The body of the vacuum chamber was designed in the 3D visualization software 3ds Max from Autodesk, in order to better visualize the spacing between flanges and the overall user-friendliness of the design (see figure D.1).

The technical draft used for constructing the chamber body is shown in figures D.2 and D.3. It is based on a wire-frame visualization from the 3D model and is as such not a correct engineering draft. The primary flaw is that the wire-frame is transparent, so front and back side objects cannot be distinguished. Combined with the solid visualizations in figure D.1, the draft was proven fully functional though.

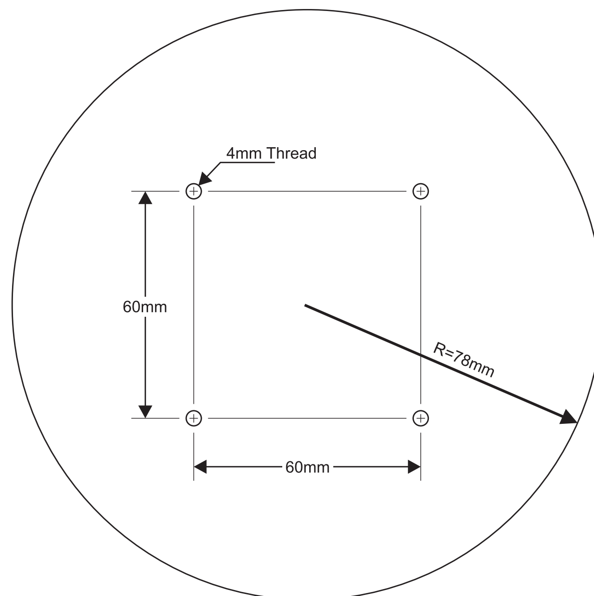

Fig. D.4: Bottom plate of the chamber body.

The top view of the chamber bottom plate is shown in figure D.4, with the location of four screw holes for mounting equipment such as a chip holder inside the chamber.

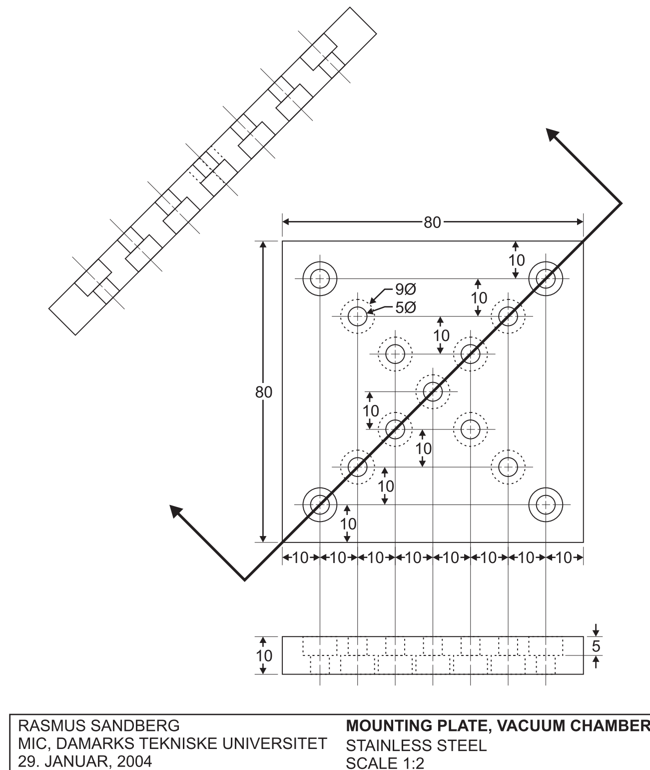

Fig. D.5: Mounting plate for vacuum chamber.

D.2 Mounting plate

The mounting plate shown in figure D.5 was constructed as an adapter between the four screw holes in the bottom plate of the chamber and any piece of equipment that should be rigidly mounted inside the chamber.

The equipment to be mounted is fastened to the plate using screws from the bottom and up. The plate with the equipment attached may then be fastened to the chamber bottom with screws from the top and down through the four outermost holes in the plate.

Figure 3.7 (p. 20) and 3.11 (p. 24) show how the aluminum base for the sample holder and the lens mount are mounted in the chamber by the plate.

D.3 Lens holder

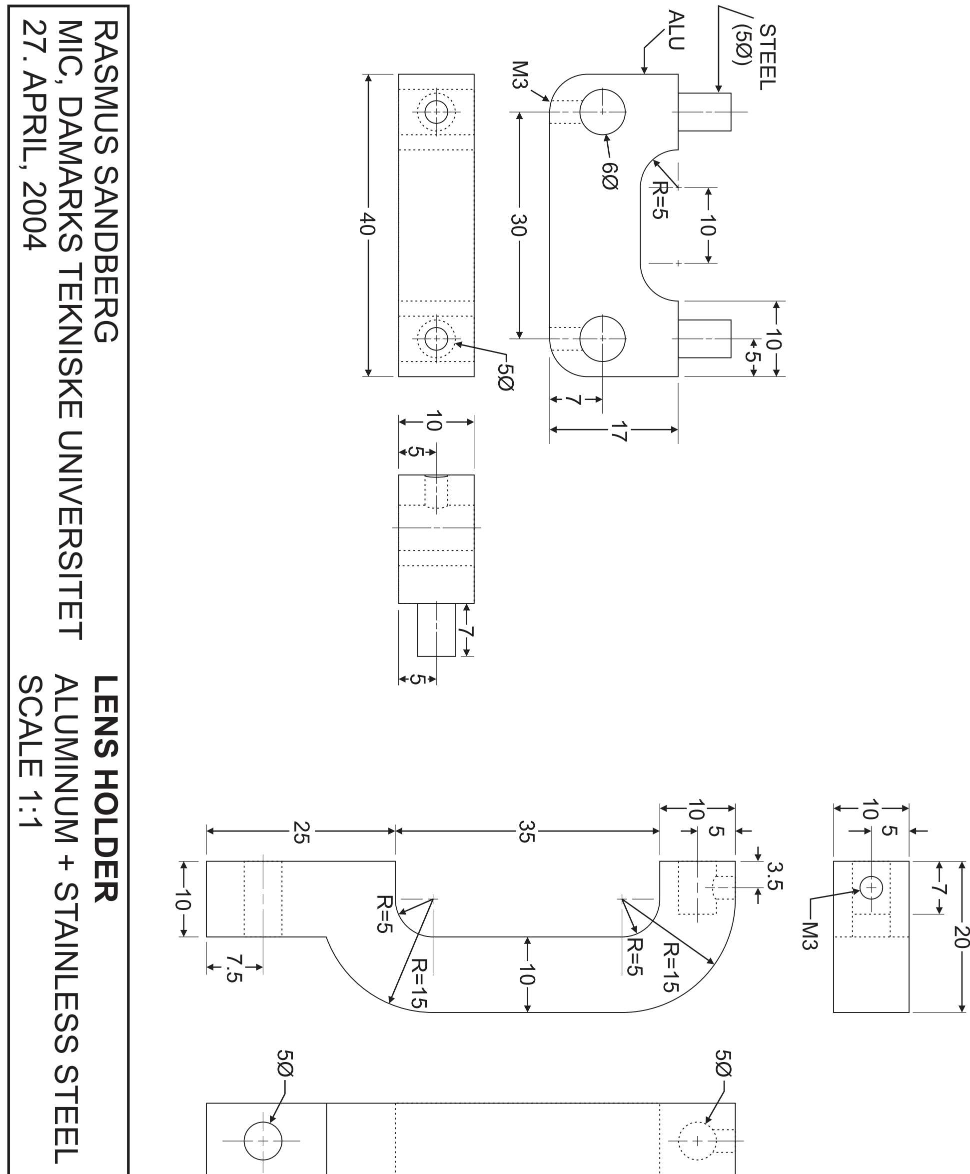

Fig. D.6: Internal lens holder for video inspection of sample in chamber.

Figure D.6 shows the technical draft of the holder for the video projection lens inside the chamber, described in section 3.4.2. Figure 3.11 (p. 24) shows the assembled parts, where the lens can be displaced horizontally by

turning the two vertical bars around the point where they are fastened to the aluminum base.

Appendix E

Electronic diagrams

The electronic diagrams and print layouts of the pre-amplifier for the position sensitive photo-detector (PSD) (section E.1) and of the difference amplifier for the PSD (section E.2) are presented in this appendix.

E.1 PSD Preamplifier

Electronic diagram and print layout of the Pre-amplifier for the PSD. The two photo-current outputs of the PSD (labelled Y1 and Y2 on the diagram) are amplified by R1 and R2 respectively. R1 and R2 are identical and have a value of 100 V/mA = 100 kΩ, which also defines the output impedance of the device. The PSD is biased with +15 V through R3.

The power supply for the pre-amplifier (± 15 V relative to common ground, 0 V) is connected to W3–W5. The signal outputs are labelled W1 and W2.

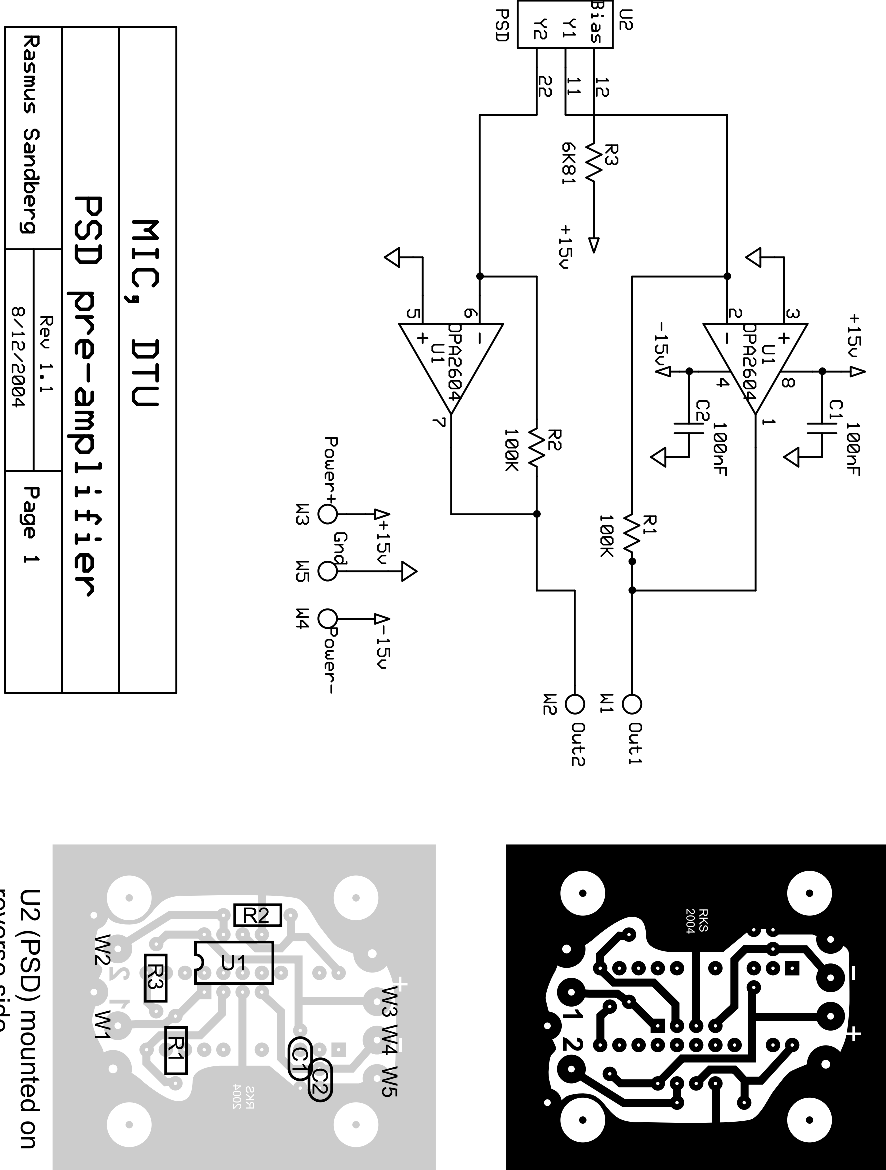

Fig. E.1: PSD Pre-amplifier, diagram and print layout.

E.2 Difference-amplifier

Electronic diagram and print layout of the Difference-amplifier for the PSD. The output voltages of the pre-amplifier are connected to W5–W7. The output voltage is given by the expression

$$U_{out} = \frac{R3(R2 + R4)U_1 - R4(R1 + R3)U_2}{R2(R1 + R3)} \tag{E.1}$$

When $R1 = R2$ and $R3 = R4$, this reduces to

$$U_{out} = (U_1 - U_2)\frac{R3}{R1} \tag{E.2}$$

The resistor values are R1=R2=1.05 kΩ and R3=R4=105 kΩ, giving an amplification of 100 and an impedance of about 106 kΩ, which almost corresponds to the output impedance of the pre-amplifier. The potentiometer P1 is used for precise adjustment of the output bias. The capacitor C3 stabilizes the gain uniformity over the operating bandwidth, but is only used for amplification factors below 20.

The power supply for the difference-amplifier (± 15 V relative to common ground, 0 V) is connected to W2–W4.

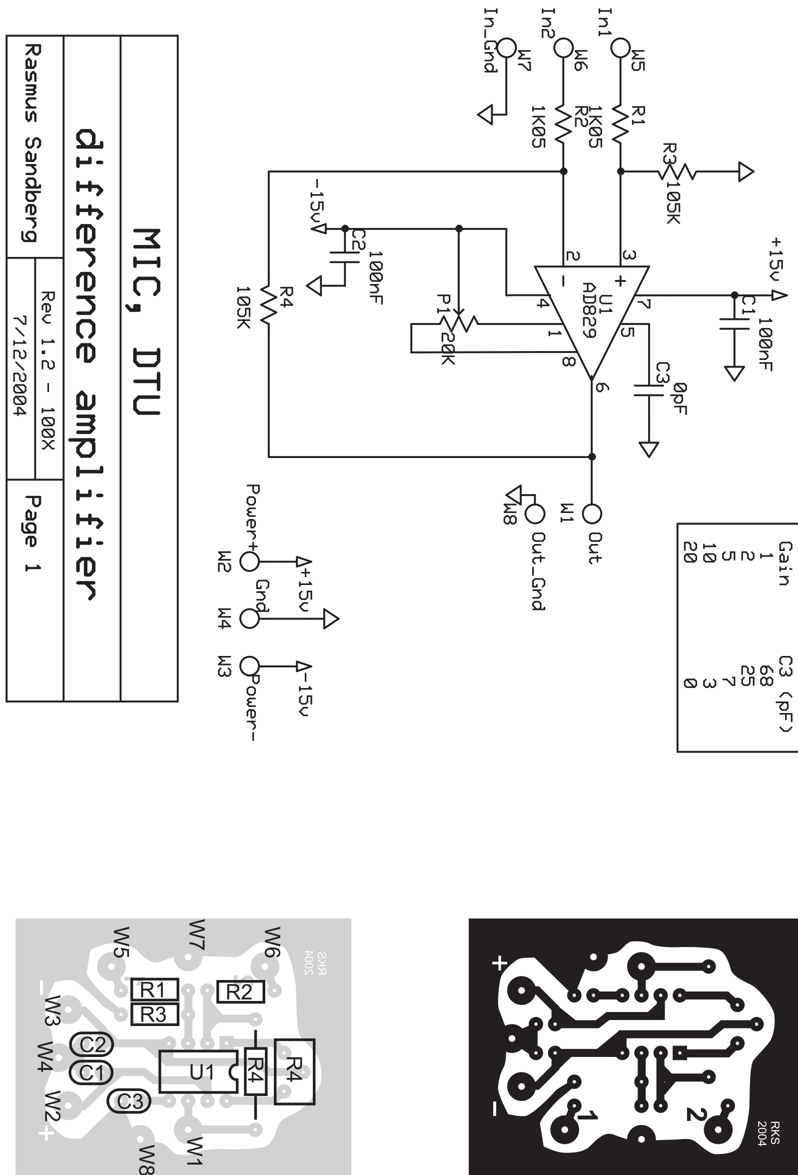

Fig. E.2: PSD Difference-amplifier, diagram and print layout.

Appendix F

LabVIEW Interface

A series of LabVIEW programs (called *virtual instruments* or just VI's) were implemented for control and data acquisition of the instruments used in the vacuum chamber and cantilever characterization setup.

A brief description of the interface and underlying program structure of the VI's used, is presented here: The VI for data acquisition from the HP 4194A gain–phase analyzer (GPA) and a VI controlling the CAL 9400 temperature controller and obtaining pressure from the HPS A900 pressure sensor.

F.1 Gain–phase analyzer VI

In order to import frequency response curves from the cantilevers characterized by the GPA, a VI was developed to read measurement data from the GPA over the GPIB bus. The interface on the GPA itself is quite user friendly and well automated, meaning that programming a VI interface for automated control of the GPA would require more time than it would eventually save.

F.1.1 Graphical interface

The user interface is shown in figure F.1. When pressing the "Update scan" button, gain- and phase-data is read and displayed in the graph. A fit of the gain-data to a Lorentz-curve is attempted and the result is displayed as a curve in the graph and as values of the derived resonance frequency, Q-factor and FWHM.

The gain-data may be displayed on a linear scale or (as shown in the figure) on a logarithmic (dB) scale. The phase-data does not have an axis of

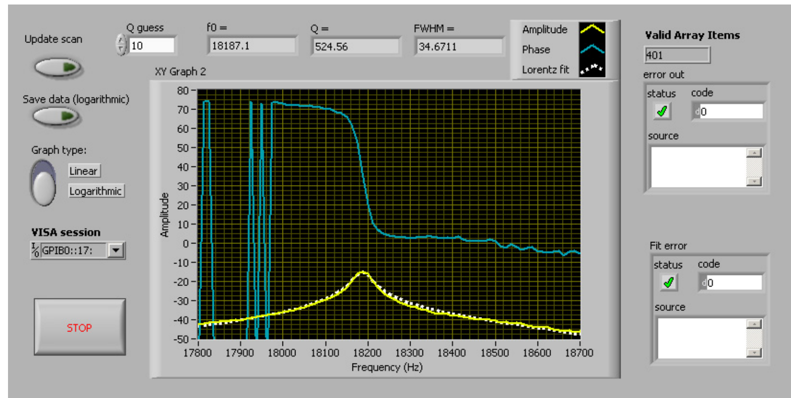

Fig. F.1: Graphical user-interface for the VI controlling the HP 4194A gain–phase analyzer.

its own but is scaled to fit in the graph.

Finally, the data may be saved in ASCII format to a file by pressing the "Save data" button. The saved gain-data will be in dB units, as indicated on the button-label.

F.1.2 Program structure

The VI is programmed as a case structure inside a loop. The case structure handles four cases, all of which are activated by user input, i.e. by pressing one of the buttons "Update scan", "Save data", "Graph type" or "Stop". The "Update scan" case is shown in figure F.2, where the individual program parts of this particular case are highlighted and described.

The curve-fitting VI is part of the LabVIEW installation and has been adapted to fit to a Lorentz-curve. It is not as efficient in finding the resonance frequency and Q-factor as Igor (see section 4.2.5) although it also uses the Levenberg-Marquardt algorithm. For low signal–to–noise ratios the fit-coefficients are unreliable, which is the reason why Igor has been used for the final data-analysis.

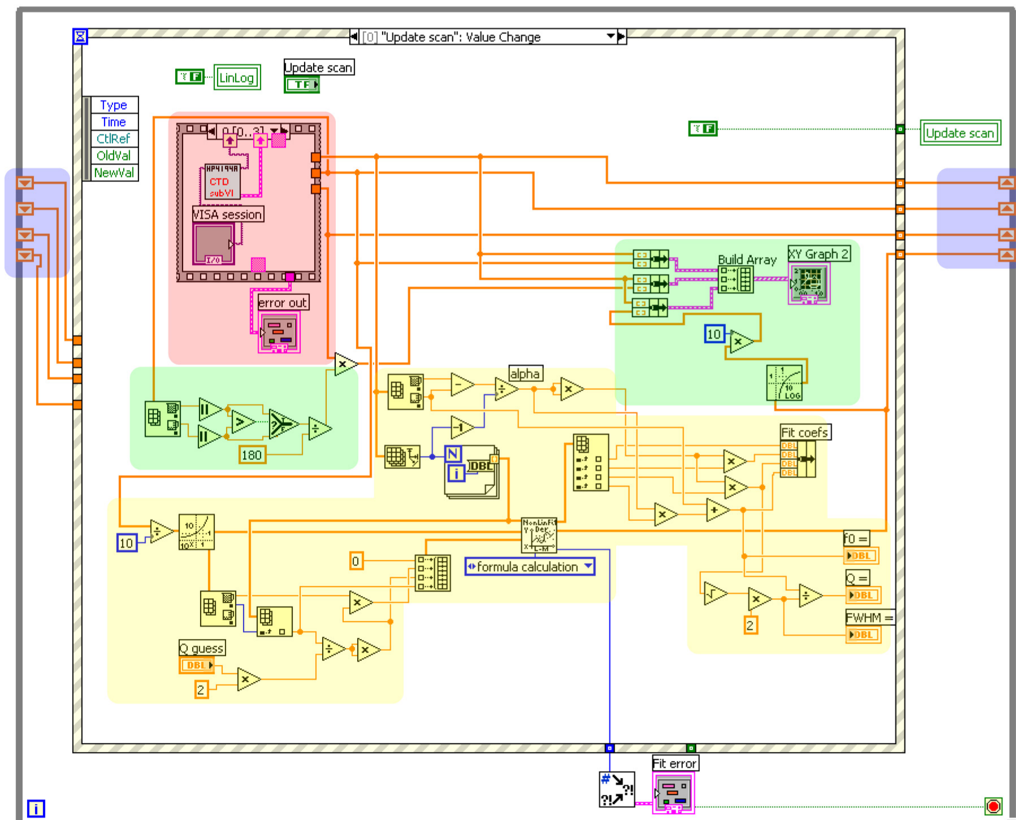

Stacked sequence, reading the gain-, phase- and frequency-axis-data from the GPA.

Data analysis, generating the Lorentz-fit and values of f_0, Q and FWHM.

Shift registers, holding the measured data and the Lorentz-fit.

Graphing routine, displaying the three curves.

Fig. F.2: Program structure of the VI for the GPA.

F.2 Temperature and pressure interface VI

The CAL 9400 temperature controller in the chamber setup has been equipped with a serial bus RS232 interface, enabling it to communicate using the MODBUS. On the back plate of the hardware interface of the pressure sensor, a signal cable may be attached for direct output of the voltages generated by the Piezo and MicroPirani transducers. These voltages have been input to a data acquisition device which may be controlled by LabVIEW over the USB bus.

A students' project was initiated with the purpose of programming a LabVIEW interface capable of controlling the temperature controller as well as importing the pressure transducer voltages and converting them to a pressure reading. The project was carried out by Reges Cezar de Andrade Costa, who designed and programmed the original VI's from which a slightly modified version is presented in this section.

F.2.1 Graphical interface

The graphical user interface is displayed in figure F.3. The bottom part is related to the pressure readout. As mentioned in section 3.3.3, the pressure transducers deliver the most accurate output if the Piezo transducer is used for pressures above 4 kPa and the MicroPirani for pressures below 4 kPa. The VI interface allows the user to specify the pressure, where the shift between the two transducers should occur. The readings of both transducers are displayed at all times in the *analogue* meters to the left, but only the *active* transducer value is logged in the data file.

The user may also specify the type of gas in the chamber. This influences the voltage–pressure conversion of the MicroPirani reading. The nonlinear conversion function is specific to the type of gas, and conversion parameters are specified by the manufacturer for nitrogen and air.

The upper graph displays the temperature history, and the controls to the left allow the user to program the temperature controller to reach a specific setpoint or to do one or two successive temperature ramps with intermediate soaking periods. A later version of the VI even allowed the user to have a message sent directly to his own computer over the local network when a specific temperature had been reached – a very useful feature for long ramp periods.

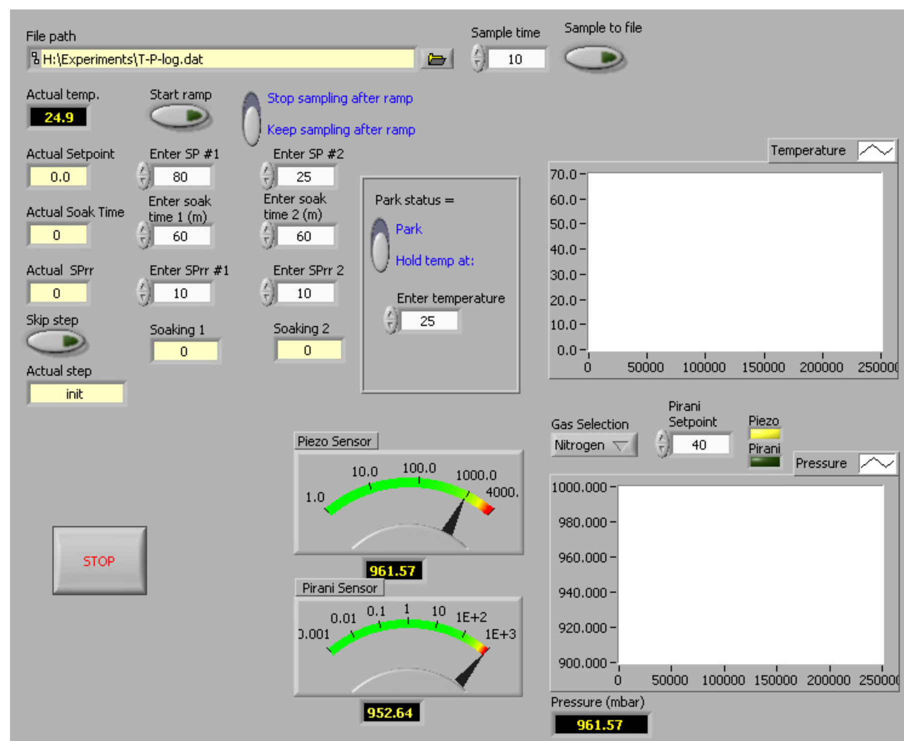

Fig. F.3: Graphical user-interface for the VI controlling the temperature controller and reading out actual temperature and pressure.

F.2.2 Program structure

Figure F.4 shows the underlying structure of the VI, which has been designed as a *state machine*, i.e. a loop structure, where each loop execution determines the *state* of the next loop. This *state* is then used as the decision parameter for a case structure, which will execute a piece of code specific to the given *state*. The different *states* in the case structure correspond to the phases of the temperature controller and the ramps: *Initialization of the variables and the controller*, *Parameter reading and controller programming*, *Temperature ramping*, *soak-time* and finally *parking*, where temperature control may be disabled or temperature may be kept constant, depending on the "Park status" switch on the graphical interface.

At specified time intervals, the structure in the right side of figure F.4 is executed. Here the VI will read the pressure, save the currently read temperature and pressure to the data file, and update the two history graphs. The graphs are updated from a binary data file, which saves system resources as compared to storing the entire data set in a local variable.

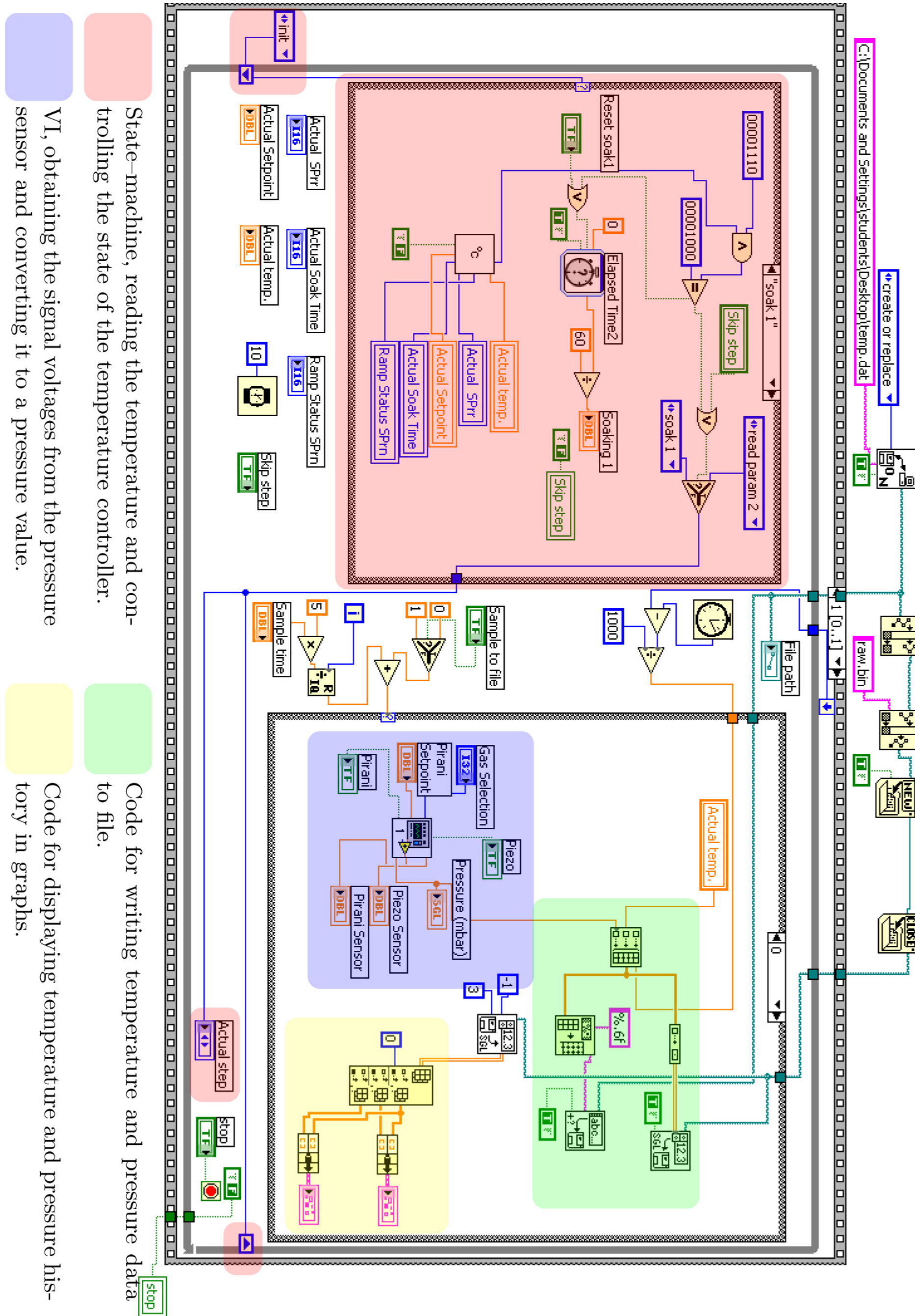

Fig. F.4: Program structure of the VI for temperature control and pressure readout.

Appendix G

List of abbreviations

AFM	Atomic Force Microscope
DNA	Deoxyribose Nucleic Acid
FEM	Finite–Element Modelling
FFC	Flat Flexible Cable
FWHM	Full–Width Half–Maximum
GPA	Gain–Phase Analyzer
PCB	Printed Circuit Board
PGA	Pin Grid Array
PID	Proportional – Integral – Derivative
PSD	Position-Sensitive (photo-)Detector
PZT	Piezo-electric Transducer
RTD	Resistance Thermometer Detector
SEM	Scanning Electron Microscope
SHO	Simple Harmonic Oscillator
SNR	Signal–to–Noise Ratio
VI	Virtual Instrument (LabVIEW-program)

Table G.1: List of abbreviations.

Bibliography

[1] G. Binnig, C.F. Quate, and C. Gerber. Atomic force microscope. *Physical Review Letters*, 56(9):930–3, 1986.

[2] Mi-Young Jung, S.S. Choi, C.J. Kang, and Y. Kuk. Fabrication of bimetallic cantilevers and its characterization. *Surface Review and Letters*, 6(6):1195–9, 1999.

[3] S. Timoshenko. Analysis of bi-metal thermostats. *Journal of the Optical Society of America*, 11:233–, 1925.

[4] J.R. Barnes, R.J. Stephenson, C.N. Woodburn, S.J. O'Shea, M.E. Welland, T. Rayment, J.K. Gimzewski, and C. Gerber. A femtojoule calorimeter using micromechanical sensors. *Review of Scientific Instruments*, 65(12):3793–8, 1994.

[5] M. Calleja, P. Rasmussen, A. Johansson, and A. Boisen. Polymeric mechanical sensors with integrated readout in a microfluidic system. *Proceedings of SPIE - The International Society for Optical Engineering*, 5116 I:314–321, 2003.

[6] Hans-Jürgen Butt. A sensitive method to measure changes in the surface stress of solids. *Journal of Colloid and Interface Science*, 180(1):251–260, 1996.

[7] Rodolphe Marie, Henriette Jensenius, Jacob Thaysen, Claus B. Christensen, and Anja Boisen. Adsorption kinetics and mechanical properties of thiol-modified DNA-oligos on gold investigated by microcantilever sensors. *Ultramicroscopy*, 91(1-4):29–36, 2002.

[8] M. Yue, H. Lin, D.E. Dedrick, S. Satyanarayana, A. Majumdar, A.S. Bedekar, J.W. Jenkins, and S. Sundaram. A 2-D microcantilever array for multiplexed biomolecular analysis. *Microelectromechanical Systems, Journal of*, 13(2):290–299, 2004.

[9] A.-R.A. Khaled, K. Vafai, M. Yang, X. Zhang, and C.S. Ozkan. Analysis, control and augmentation of microcantilever deflections in bio-sensing systems. *Sensors and Actuators B: Chemical*, 94(1):103–115, 2003.

[10] T. Thundat, E.A. Wachter, S.L. Sharp, and R.J. Warmack. Detection of mercury vapor using resonating microcantilevers. *Applied Physics Letters*, 66(13):1695–7, 1995.

[11] J.D. Adams, G. Parrott, C. Bauer, T. Sant, L. Manning, M. Jones, B. Rogers, D. McCorkle, and T.L. Ferrell. Nanowatt chemical vapor detection with a self-sensing, piezoelectric microcantilever array. *Applied Physics Letters*, 83(16):3428–3430, 2003.

[12] T. Thundat, G.Y. Chen, R.J. Warmack, D.P. Allison, and E.A. Wachter. Vapor detection using resonating microcantilevers. *Analytical Chemistry*, 67(3):519–521, 1995.

[13] Nicolas Ledermann, Paul Muralt, Jacek Baborowski, Martin Forster, and Jean-Paul Pellaux. Piezoelectric $pb(zr_x, ti_{1-x})o_3$ thin film cantilever and bridge acoustic sensors for miniaturized photoacoustic gas detectors. *Journal of Micromechanics and Microengineering*, 14(12):1650–1658, 2004.

[14] Kyo Seon Hwang, Jeong Hoon Lee, Jaebum Park, Jung Ho Park, and Tae Song Kim. Protein mass detection system in liquid for prostate-specific antigen (PSA) using PDMS liquid cell by resonant frequency shift of micromachined PZT cantilever. *Miniaturized Chemical and Biochemical Analysis Systems, 2003. 7th International Conference on*, pages 1267–1269, 2003.

[15] T.P. Burg and S.R. Manalis. Suspended microchannel resonators for biomolecular detection. *Applied Physics Letters*, 83(13):2698–2700, 2003.

[16] B. Ilic, H.G. Craighead, S. Krylov, W. Senaratne, C. Ober, and P. Neuzil. Attogram detection using nanoelectromechanical oscillators. *Journal of Applied Physics*, 95(7):3694–3703, 2004.

[17] G. Abadal, Z.J. Davis, B. Helbo, X. Borrise, R. Ruiz, A. Boisen, F. Campabadal, J. Esteve, E. Figueras, F. Perez-Murano, and N. Barniol. Electromechanical model of a resonating nano-cantilever-based sensor for high-resolution and high-sensitivity mass detection. *Nanotechnology*, 12(2):100–104, 2001.

[18] Göran Stemme. Resonant silicon sensors. *Journal of Micromechanics and Microengineering*, 1(2):113–125, 1991.

[19] Z.J. Davis, G. Abadal, B. Helbo, O. Hansen, F. Campabadal, F. Perez-Murano, J. Esteve, E. Figueras, J. Verd, N. Barniol, and A. Boisen. Monolithic integration of mass sensing nano-cantilevers with CMOS circuitry. *Sensors and Actuators A: Physical*, 105(3):311–319, 2003.

[20] J.H. Lee, K.H. Yoon, K.S. Hwang, J. Park, S. Ahn, and T.S. Kim. Label free novel electrical detection using micromachined PZT monolithic thin film cantilever for the detection of C-reactive protein. *Biosensors and Bioelectronics*, 20(2):269–275, 2004.

[21] Y. Li, C. Vancura, C. Hagleitner, J. Lichtenberg, O. Brand, and H. Baltes. Very high Q-factor in water achieved by monolithic, resonant cantilever sensor with fully integrated feedback. *Sensors, 2003. Proceedings of IEEE*, pages 809–813 Vol.2, 2003.

[22] A. Mehta, S. Cherian, D. Hedden, and T. Thundat. Manipulation and controlled amplification of brownian motion of microcantilever sensors. *Applied Physics Letters*, 78(11):1637–9, 2001.

[23] D.A. Walters, J.P. Cleveland, N.H. Thomson, P.K. Hansma, M.A. Wendman, G. Gurley, and V. Elings. Short cantilevers for atomic force microscopy. *Review of Scientific Instruments*, 67(10):3583–90, 1996.

[24] G. Meyer and N.M. Amer. Novel optical approach to atomic force microscopy. *Applied Physics Letters*, 53(12):1045–7, 1988.

[25] H. J. McSkimin. Measurement of elastic constants at low temperatures by means of ultrasonic waves — data for silicon and germanium single crystals, and for fused silica. *Journal of Applied Physics*, 24(8):988–, 1953.

[26] F. Shen, P. Lu, S.J. O'Shea, K.H. Lee, and T.Y. Ng. Thermal effects on coated resonant microcantilevers. *Sensors and Actuators A: Physical*, 95(1):17–23, 2001.

[27] J. Mertens, E. Finot, T. Thundat, A. Fabre, M.-H. Nadal, V. Eyraud, and E. Bourillot. Effects of temperature and pressure on microcantilever resonance response. *Ultramicroscopy*, 97(1-4):119–126, 2003.

[28] A. Passian, R.J. Warmack, A. Wig, R.H. Farahi, F. Meriaudeau, T.L. Ferrell, and T. Thundat. Observation of knudsen effect with microcantilevers. *Ultramicroscopy*, 97(1-4):401–406, 2003.

[29] L. Fadel, I. Dufour, F. Lochon, and O. Francais. Optimization of the signal to noise ratio of resonant microcantilever type chemical sensors. *TRANSDUCERS, Solid-State Sensors, Actuators and Microsystems, 12th Innational Conference on, 2003*, 2:1351–1354, 2003.

[30] L. Fadel, I. Dufour, F. Lochon, and O. Francais. Signal-to-noise ratio of resonant microcantilever type chemical sensors as a function of resonant frequency and quality factor. *Sensors and Actuators B: Chemical*, 102(1):73–77, 2004.

[31] Nickolay V. Lavrik, Michael J. Sepaniak, and Panos G. Datskos. Cantilever transducers as a platform for chemical and biological sensors. *Review of Scientific Instruments*, 75(7):2229–2253, 2004.

[32] Christiane Ziegler. Cantilever-based biosensors. *Analytical and Bioanalytical Chemistry*, 379(7-8):946–959, 2004.

[33] M. Ataka, A. Omodaka, N. Takeshima, and H. Fujita. Fabrication and operation of polyimide bimorph actuators for a ciliary motion system. *Microelectromechanical Systems, Journal of*, 2(4):146–150, 1993.

[34] D. Lange, C. Hagleitner, C. Herzog, O. Brand, and H. Baltes. Magnetic actuation and mos-transistor sensing for cmos-integrated resonators. *Micro Electro Mechanical Systems, 2002. The Fifteenth IEEE International Conference on*, pages 304–307, 2002.

[35] J. Thaysen, A.D. Yalcinkaya, P. Vettiger, and A. Menon. Polymer-based stress sensor with integrated readout. *Journal of Physics D: Applied Physics*, 35(21):2698–2703, 2002.

[36] P.A. Rasmussen, J. Thaysen, O. Hansen, S.C. Eriksen, and A. Boisen. Optimised cantilever biosensor with piezoresistive read-out. *Ultramicroscopy*, 97(1-4):371–376, 2003.

[37] Dror Sarid. *Scanning Force Microscopy with applications to electric, magnetic, and atomic forces*. Oxford University Press, Inc., 200 Madison Avenue, New York 10016, 1991.

[38] J.E. Sader, I. Larson, P. Mulvaney, and L.R. White. Method for the calibration of atomic force microscope cantilevers. *Review of Scientific Instruments*, 66(7):3789–98, 1995.

[39] C.T. Gibson, B.L. Weeks, J.R.I. Lee, C. Abell, and T. Rayment. A non-destructive technique for determining the spring constant of atomic force

microscope cantilevers. *Review of Scientific Instruments*, 72(5):2340–3, 2001.

[40] Nanomass project, [http://einstein.uab.es/_c_nanomass]. Internet site.

[41] Christian Bergaud, Liviu Nicu, and Augustin Martinez. Multi-mode air damping analysis of composite cantilever beams. *Japanese Journal of Applied Physics, Part 1: Regular Papers and Short Notes and Review Papers*, 38(11):6521–6525, 1999.

[42] H.F. Dylla, D.M. Manos, and P.H. LaMarche. Correlation of outgassing of stainless steel and aluminum with various surface treatments. *Journal of Vacuum Science & Technology A (Vacuum, Surfaces, and Films)*, 11(5):2623–2636, 1993.

[43] Shuzo Ohe. Web publication [www.s-ohe.com/acetone_cal.html] with data from “computer aided data book of vapor pressure”, data book publishing company, tokyo, japan, 1999.

[44] Allmeasures.com [http://www.allmeasures.com]. Internet html document.

[45] F.L. Pedrotti and L.S. Pedrotti. *Introduction to Optics*. Prentice Hall, Englewood Cliffs, New Jersey 07632, second edition, 1993.

[46] Lars Stenberg. The PSD school, sec.11: How to reduce the aberrations in the lens system. Internet site, [http://www.sitek.se].

[47] Polytec Incorporated. MSV-400 microscope scanning vibrometer. PDF-document available at [http://www.polytec.com], 2004.

[48] Max Ti-Kuang Hou and Rongshun Chen. Effect of width on the stress-induced bending of micromachined bilayer cantilevers. *Journal of Micromechanics and Microengineering*, 13(1):141–148, 2003.

[49] Sangmin Jeon and Thomas Thundat. Instant curvature measurement for microcantilever sensors. *Applied Physics Letters*, 85(6):1083–1084, 2004.

[50] U. Harms and H. Neuhauser. Influence of stress in thin film modulus measurements by the vibrating reed technique. *Thin Solid Films*, 323(1-2):153–157, 1998.

[51] Q. Ren and Y.-P. Zhao. Influence of surface stress on frequency of microcantilever-based biosensors. *Microsystem Technologies*, 10(4):307–314, 2004.

[52] K.Y. Yasumura, T.D. Stowe, E.M. Chow, T. Pfafman, T.W. Kenny, B.C. Stipe, and D. Rugar. Quality factors in micron- and submicron-thick cantilevers. *Microelectromechanical Systems, Journal of*, 9(1):117–125, 2000.

[53] M.J. Tudor, M.V. Andres, K.W.H. Foulds, and J.M. Naden. Silicon resonator sensors: interrogation techniques and characteristics. *IEE Proceedings D (Control Theory and Applications)*, 135(5):364–368, 1988.

[54] Kyungsuk Yum, Zhaoyu Wang, Abhijit P. Suryavanshi, and Min-Feng Yu. Experimental measurement and model analysis of damping effect in nanoscale mechanical beam resonators in air. *Journal of Applied Physics*, 96(7):3933–3938, 2004.

[55] James W.M. Chon, Paul Mulvaney, and John E. Sader. Experimental validation of theoretical models for the frequency response of atomic force microscope cantilever beams immersed in fluids. *Journal of Applied Physics*, 87(8):3978–3988, 2000.

[56] F.R. Blom, S. Bouwstra, M. Elwenspoek, and J.H.J. Fluitman. Dependence of the quality factor of micromachined silicon beam resonators on pressure and geometry. *Journal of Vacuum Science & Technology B (Microelectronics Processing and Phenomena)*, 10(1):19–26, 1992.

[57] Young-Ho Cho, A.P. Pisano, and R.T. Howe. Viscous damping model for laterally oscillating microstructures. *Microelectromechanical Systems, Journal of*, 3(2):81–87, 1994.

[58] G. Lévêque, P. Girard, S. Belaidi, and G. Cohen Solal. Effects of air damping in noncontact resonant force microscopy. *Review of Scientific Instruments*, 68(11):4137–4144, 1997.

[59] J.E. Sader. Frequency response of cantilever beams immersed in viscous fluids with applications to the atomic force microscope. *Journal of Applied Physics*, 84(1):64–76, 1998.

[60] H. Walther. Internal friction in solids. *The Scientific Monthly*, 41(3):275–277, 1935. Journal archived digitally by JSTOR [http://www.jstor.org].

[61] Torben Mikael Hansen. *Tools for Nanoscale Conductivity Measurements.* PhD thesis, MIC – Mikroelektronik Centret, Technical University of Denmark, 2003.

[62] Gino Rinaldi, Muthukumaran Packirisamy, and Ion Stiharu. An improved method for predicting microfabrication influence in atomic force microscopy performances. *International Journal of Nanotechnology*, 1(3):292–306, 2004.

[63] Coventor, Inc. Coventorware materials database. Commercial software distribution, April 2004.

[64] Mark J. Winter. Webelements [http://www.webelements.com]. Internet html document.

[65] WaveMetrics, Inc., PO Box 2088, Lake Oswego, OR 97035, USA. *Igor Pro ver. 4.0*, 10/00 (4.01) edition, 2000.

[66] G.Y. Chen, R.J. Warmack, T. Thundat, D.P. Allison, and A. Huang. Resonance response of scanning force microscopy cantilevers. *Review of Scientific Instruments*, 65(8):2532–7, 1994.

[67] R. Lifshitz and M.L. Roukes. Thermoelastic damping in micro- and nanomechanical systems. *Physical Review B (Condensed Matter)*, 61(8):5600–9, 2000.

[68] Corning Incorporated. HPFS® Fused silica standard grade. PDF-document available at [http://www.corning.com], September 2003.

[69] Douglas M. Photiadis and John A. Judge. Attachment losses of high Q oscillators. *Applied Physics Letters*, 85(3):482–484, 2004.

[70] Ulric S. Lindholm, Daniel D. Kana, Weh-Hwa Chu, and H. Norman Abramson. Elastic vibration characteristics of cantilever plates in water. *Journal of Ship Research*, 9(1):11–22, 1965.

[71] Cho-Chung Liang, Ching-Chao Liao, Yuh-Shiou Tai, and Wen-Hao Lai. The free vibration analysis of submerged cantilever plates. *Ocean Engineering*, 28(9):1225–1245, 2001.

[72] J.E. Sader, J.W.M. Chon, and P. Mulvaney. Calibration of rectangular atomic force microscope cantilevers. *Review of Scientific Instruments*, 70(10):3967–3969, 1999.

[73] Søren Dohn, Rasmus Sandberg, Winnie Svendsen, and Anja Boisen. Enhanced functionality of cantilever based mass sensors using higher modes. Submitted to Applied Physics Letters, 2005.

[74] F. Höök, M. Rodahl, C. Keller, K. Glasmästar, C. Fredriksson, P. Dahlqvist, and B. Kasemo. The dissipative QCM-D technique: interfacial phenomena and sensor applications for proteins, biomembranes, living cells and polymers. *European Frequency and Time Forum, 1999 and the IEEE International Frequency Control Symposium, 1999., Proceedings of the 1999 Joint Meeting of the*, 2:966–972 vol.2, 1999.

[75] Rodolphe Marie. *Nucleic acids reactions investigated by cantilever-based sensor*. PhD thesis, MIC, Department of Micro and Nanotechnology, Technical University of Denmark, 2003.

[76] Tonya M. Herne and Michael J. Tarlov. Characterization of DNA probes immobilized on gold surfaces. *Journal of the American Chemical Society*, 119(38):8916–8920, 1997.

[77] E. Forsén, G. Abadal, S. G. Nilsson, J. Verd, R. Sandberg, W. Svendsen, J. Teva, F. Peréz-Murano, J. Esteve, E. Figueras, F. Campabadal, L. Montelius, N. Barniol, and A. Boisen. Fully integrated nanoresonator system with attogram/Hz mass resolution. *Proceedings of the 8th international conference on Micro Electro Mechanical Systems, IEEE MEMS*, pages 867–870, 2005. Miami Beach, FL, USA, 2005.

[78] E. Forsén, G. Abadal, S. Ghatnekar-Nilsson, J. Teva, J. Verd, R. Sandberg, W. Svendsen, F. Peréz-Murano, J. Esteve, E. Figueras, F. Campabadal, L. Montelius, N. Barniol, and A. Boisen. Ultrasensitive mass sensor fully integrated with CMOS. Submitted to Applied Physics Letters, 2005.

[79] A.V. Grigorov, Z.J. Davis, P. Rasmussen, and A. Boisen. A longitudinal thermal actuation principle for mass detection using a resonant microcantilever in a fluid medium. *Microelectronic Engineering*, 73-74:881–886, 2004.

[80] K.L. Ekinci, Y.T. Yang, and M.L. Roukes. Ultimate limits to inertial mass sensing based upon nanoelectromechanical systems. *Journal of Applied Physics*, 95(5):2682–2689, 2004.

[81] Bahaa E.A. Saleh and Malvin Carl Teich. *Fundamentals of Photonics*. John Wiley & Sons, Inc., New York, 1991.

[82] Torben Skettrup. *Laserteknik.* Polyteknisk Forlag, Anker Engelundsvej 1, DK-2800 Kgs. Lyngby, Denmark, 5. edition, 1993.

[83] Danchip, [http://www.danchip.dtu.dk].